

2011

# Sequestration of Arsenic by nanoscale Zero-Valent Iron (nZVI): Surface Reactions Characterized by High Resolution X-Ray Photoelectron Spectroscopy (HR-XPS)

Mauricio Alfred Valencia Ramos  
*Lehigh University*

Follow this and additional works at: <http://preserve.lehigh.edu/etd>

---

## Recommended Citation

Valencia Ramos, Mauricio Alfred, "Sequestration of Arsenic by nanoscale Zero-Valent Iron (nZVI): Surface Reactions Characterized by High Resolution X-Ray Photoelectron Spectroscopy (HR-XPS)" (2011). *Theses and Dissertations*. Paper 1311.

This Dissertation is brought to you for free and open access by Lehigh Preserve. It has been accepted for inclusion in Theses and Dissertations by an authorized administrator of Lehigh Preserve. For more information, please contact [preserve@lehigh.edu](mailto:preserve@lehigh.edu).

Sequestration of Arsenic by nanoscale Zero-Valent Iron (nZVI): Surface Reactions  
Characterized by High Resolution X-Ray Photoelectron Spectroscopy (HR-XPS)

by

Mauricio A. Valencia Ramos

A Dissertation

Presented to the Graduate and Research Committee

of Lehigh University

in Candidacy for the Degree of

Doctor of Philosophy

in

Chemistry

Lehigh University

May 2011

Copyright  
Mauricio Alfred Ramos Valencia

Approved and recommended for acceptance as a dissertation in partial fulfillment of the requirements for the degree of Doctor of Philosophy

Mauricio Alfred Ramos Valencia

“Sequestration of Arsenic by nanoscale Zero-Valent Iron (nZVI): Surface Reactions Characterized by High Resolution X-Ray Photoelectron Spectroscopy (HR-XPS)”

---

Defense Date

---

Prof. Bruce E. Koel

---

Approved Date

Committee Members

---

Prof. Tianbo Liu

---

Prof. Daniel Zeroka

---

Prof. Wei-xang Zhang

## DEDICATION

To my Family

## ACKNOWLEDGEMENTS

First of all, I would like to thank my research advisor Prof. Bruce E. Koel for his support and guidance during my PhD studies at Lehigh University and the University of Southern California. His advice, great knowledge, and patience have been indispensable in the process of obtaining my PhD in chemistry. I would like to extend my gratitude to Dr. Al Miller for mentoring me in the use of the HR-XPS Scienta ESCA 300, which became a significant part in the development of my research. I want to give especial thanks to Dr. Wei-xian Zhang and Weile Yan for their insight, friendship and for the opportunity to collaborate with them, which has formed an essential part of my research. I am also grateful to my friends, past and present Koel research group members for their input and support John Martin, Lindsey Welch, Xiaofang Yang, Jie Fu, Dr. Frank Liu, and Dr. Michael Hughes.

I am also grateful to my committee members for their time and advice, Prof. Tianbo Liu, Prof. Daniel Zeroka, and Prof. Wei-xian Zhang.

Finally, I would like to thank my dear family and all my friends both in California and Pennsylvania for their encouragement, understanding, and patience. Without a doubt they have made all the difference.

## TABLE OF CONTENTS

List of Figures . . . . .	x
List of Tables . . . . .	xiv
ABSTRACT . . . . .	1
CHAPTER	
I. INTRODUCTION . . . . .	3
1.1 Background . . . . .	3
1.1.1 The influence of redox kinetics on arsenic speciation . . . . .	7
1.2 Adsorption reactions of arsenic species with Fe(0) . . . . .	7
1.3 Role of Fe(0) in the electrochemical reduction of As(III) and As(V) . . . . .	8
1.4 Synthesis and use of iron nanoparticles for environmental remediation . . . . .	9
1.5 Issues and challenges concerning the use of nZVI for environmental remediation . . . . .	12
1.5.1 Materials chemistry: economics . . . . .	12
1.5.2 Environmental concerns . . . . .	13
1.5.3 Geochemistry . . . . .	13
1.5.4 Environmental impact . . . . .	13
1.6 Equilibrium potential and pH effect of arsenic adsorption on nZVI . . . . .	14
1.7 Oxide layer thickness in core-shell nZVI . . . . .	17
1.8 nZVI reaction mechanisms . . . . .	18
1.9 Scope of thesis . . . . .	20
References . . . . .	21

II. EXPERIMENTAL METHODS . . . . .	25
2.1 Characterization and Analysis of As-treated nZVI using High-Resolution X-ray Photoelectron Spectroscopy . . . . .	25
2.1.1 X-ray source . . . . .	27
2.1.2 Monochromator . . . . .	27
2.1.3 Electron lenses . . . . .	27
2.1.4 Hemispherical Electron Energy Analyzer (HMA) . . . . .	28
2.1.5 Multichannel detector . . . . .	28
2.2 Considerations in building a new FTIR apparatus (Improving noise % transmittance) . . . . .	29
2.2.1 Detector/filter combination . . . . .	29
2.2.2 Incident source light and SAMs surface . . . . .	35
2.2.3 Mirrors . . . . .	35
2.2.4 Lenses . . . . .	36
2.2.5 Polarization Flipper . . . . .	37
References . . . . .	38
III. SIMULTANEOUS OXIDATION AND REDUCTION OF ARSENIC BY ZERO-VALENT IRON NANOPARTICLES: UNDERSTANDING THE SIGNIFICANCE OF THE CORE-SHELL STRUCTURE . . . . .	39
3.1 Introduction . . . . .	39
3.2 Materials and Experimental Methods . . . . .	40
3.2.1 As Reactions . . . . .	40
3.2.2 XPS Analysis . . . . .	41
3.3 Results and Discussion . . . . .	42
3.3.1 Reactions with As(V) . . . . .	42



3.3.2 Reactions with As(III)	45
3.3.3 Effect of As(III) concentrations	48
3.4 Conclusion	57
References	58
<b>IV. ARSENIC ENCAPSULATION IN IRON NANOPARTICLES: EVIDENCE OF INTRAPARTICLE REACTIONS</b>	<b>60</b>
4.1 Introduction	60
4.2 Experimental methods	61
4.2.1 Preparation of iron materials	61
4.2.2 Arsenic batch experiments	64
4.2.3 XPS analysis	64
4.3 Results and Discussion	65
4.3.1 Analysis of depth-dependent distribution of multiple As valence states within nZVI and iron oxides ( $\text{Fe}_3\text{O}_4$ and $\text{Fe}_2\text{O}_3$ )	66
4.4 Conclusion	78
References	80
<b>V. REMOVAL OF AS(III) BY IRON NANOPARTICLES (NZVI): INVESTIGATION OF SOLID-PHASE ARSENIC-IRON REACTIONS</b>	<b>83</b>
5.1 Introduction	83
5.2 Materials and Methods	86
5.2.1 Preparation of iron materials	86
5.2.2 Batch experiments	86
5.2.3 Aqueous phase analysis	88
5.2.4 Solid phase analysis using XPS/SEM/TEM/XRD	88

5.3 Results and Discussion . . . . .	89
5.3.1 Characterization of nZVI . . . . .	89
5.3.2 As(III) removal from the aqueous phase . . . . .	90
5.3.3 Arsenic speciation on the solid phase . . . . .	94
5.3.4 Arsenic speciation over time . . . . .	100
5.3.5 Effect of nZVI dose . . . . .	105
5.3.6 Reaction model and practical implications . . . . .	109
5.4 Conclusion . . . . .	112
References . . . . .	114
VI. CONCLUDING REMARKS . . . . .	117
6.1 Summary . . . . .	117
Curriculum Vitae . . . . .	119

## LIST OF FIGURES

### Figures

1.1	The concentration of inorganic (arsenious acid and arsenic acid) and organic arsenic species (MMA and DMA) occurring in natural waters plays an important role in the understanding of the mobility and toxicity of arsenic species in the ecological systems [adapted from ref. 26]	6
1.2	Depicting a pe–pH diagram for the As–Fe–H <sub>2</sub> O equilibrium and redox systems at 25°C [42]	10
1.3	Thermodynamic cycle depicting the reduction of As(V) in aqueous solution. As(III) and As(V) can be bound to the iron oxide layer coating the iron metal surface [adapted from reference 58]	16
2.1	Schematic depicting the ESCA 300 main components	26
2.2	Reducing % noise transmittance in an FTIR apparatus: ■) purging with N <sub>2</sub> and ▲) evacuating the system with the use of turbo pumps	32
2.3	The Optimized FTIR Optical System consists of: <b>1)</b> Evacuated Vector 22 FTIR, <b>2)</b> Evacuated Mirror Box, <b>3)</b> Evacuated Polarization Flipper (small blue-edged rectangle) Box, <b>4)</b> UHV Sample Chamber, and <b>5)</b> Evacuated Filter/Detector Combination (green circle) Box. The red lines represent the optical path of the IR and laser source	33
2.4	Actual FTIR Optical System	34
3.1	As3d HR-XPS spectra of (a) fresh nZVI and (b) nZVI reacted with 100mg/L As(V), and (c) nZVI reacted with 100mg/L As(III). The nZVI loading in (b) and (c) was 5g/L. The proportions of the respective species as percentages of the total As detected are annotated on the spectra. The intensity scale varies for each curve.	43
3.2	(a) Bright field-TEM micrograph of nZVI nanoparticles showing a core-shell structure comprised of a dense metallic center and a thin, continuous oxide skin. The inset shows the electron diffraction pattern of the metallic core, which suggests a polycrystalline <i>bcc</i> structure. (b) HR-TEM micrograph of a single nZVI nanoparticle. The lack of long-range periodic lattice fringes in the oxide layer suggests that it is amorphous in character.	47
3.3	As3d HR-XPS spectra from nZVI particles exposed to different initial concentrations of As(III). The nZVI loading was 5g/L in all cases. The inset of (a) is a vertically expanded view of spectrum (a).	49

3.4 Solution pH for various initial As(III) concentrations. nZVI loading was fixed at 5 g/L. Initial pH was measured before nZVI loading. Equilibrium pH was obtained after a reaction time of 24 hours. The dashed line corresponds to the $pK_a$ value of $H_3AsO_3$ , which dissociates to $H_2AsO_3^-$ at $pH > pK_a$ .	50
3.5 O1s HR-XPS spectra obtained after different initial concentrations of As(III) (nZVI loading was fixed at 5 g/L). The prominent increase in $OH^-$ at the two highest As(III) concentrations indicates substantial iron hydroxide formation at the solid surface. The different forms of oxygen are indicated in the top spectrum: $H_2O$ at 531.8 eV, $OH^-$ at 530.7 eV, and $O^{2-}$ at 529.5 eV.	52
3.6 SEM images of a) a fresh nZVI sample, b) 5g/L nZVI reacted with 100 mg/L As(III) for 24 h, and c) 5g/L nZVI reacted with 1000 mg/L As(III) for 24 h.	54
3.7 As3d HR-XPS spectra from nZVI particles reacted with 100 mg/L As(III) for different reaction times. The nZVI loading was 5g/L in all cases. The proportions of the respective species as percentages of the total As detected are annotated on the spectra.	55
4.1 (a)-(b) Field-emission SEM micrographs of freshly made nZVI nanoparticles showing the particles are in the size range of 50 to 100 nm. (c) Bright field TEM micrograph of an individual nZVI particle reveals a dense core encapsulated by a thin continuous layer of iron oxide. The inset shows electron diffraction from the interior core region, in which the diffuse ring pattern is characteristic of polycrystalline <i>bcc</i> Fe(0). (d) Phase contrast TEM image of a particle. The lack of long-range periodic lattice fringes in the oxide region underlies its amorphous nature.	62
4.2 Elements whose spectra exhibit photoelectron lines widely spaced in Kinetic Energy (KE) (e.g. As lines 2p and 3d) can be located using the intensity ratio of the lines. In general, electrons with lower KE are attenuated more when moving through a solid phase, whereas those of higher KE have a greater escape path. Thus for a surface species the lower KE component will be stronger than the higher KE component	67
4.3 HR-XPS spectra of (a) As2p <sub>3/2</sub> and (b) As3d regions of various Fe materials reacted with As(III) solutions. These two core-levels were chosen because of the widely spaced kinetic energies of the respective photoelectrons and hence difference in surface sensitivity. As2p <sub>3/2</sub> spectra arise from photoemission from a shallower depth than does As3d spectra. The top spectrum of each column is that of pure sodium arsenite ( $NaAsO_2$ ), which was used to prepare the As(III) solutions used in these experiments. The vertical scale of the two spectra from the nZVI sample is enlarged five-fold. Samples were prepared by reacting 5g/L of the iron oxides or nZVI with deoxygenated 1.3 mMAs(III) solutions for 24 hours.	68

4.4 Normalized intensity ratios of the As <sub>2p<sub>3/2</sub></sub> to As <sub>3d</sub> peaks in HR-XPS spectra. . . . .	75
4.5 Fe <sub>2p</sub> HR-XPS spectra of nZVI reacted with an 100 mg/L As(III)solution for 24 hours. The small peak at 707.0 eV BE corresponds to the Fe <sub>2p<sub>3/2</sub></sub> signal from Fe(0) and the larger peak at 710.8 eV BE corresponds to the Fe <sub>2p<sub>3/2</sub></sub> signal from oxidized Fe. Using the Fe <sub>2p<sub>3/2</sub></sub> intensities observed for metallic and oxidized iron, the average thickness of the oxide layer can be calculated to be 4.2 nm using the XPS Multi-Quant software. . . . .	76
4.6 Schematic illustrations of the depth distribution of arsenic species in iron oxides and nZVI. The left-hand scale bars indicate the escape depth (3λ) of As <sub>3d</sub> photoelectrons in iron (oxy)hydroxide (FeOOH). The thickness of the surface oxide layer for nZVI is calculated from the relative intensities of metallic and oxidized iron contributions in the Fe <sub>2p</sub> spectra. . . . .	77
5.1 (a)-(b) Field-emission SEM micrographs of freshly made nZVI nanoparticles showing the particles are in the size range of 50 to 100 nm. (c) Bright field TEM micrograph of an individual nZVI particle reveals a dense core encapsulated by a thin continuous layer of iron oxide. The inset shows electron diffraction from the interior core region, in which the diffuse ring pattern is characteristic of polycrystalline <i>bcc</i> Fe(0). (d) Phase contrast TEM image of a particle. The lack of long-range periodic lattice fringes in the oxide region suggests it is amorphous in nature. . . . .	91
5.2 Change in aqueous arsenic concentration with time. Initial As(III) concentration (C <sub>0</sub> ) was 100 mg/L; nZVI or iron oxide dose was 5 g/L. Inset: percentage As(III) removal at various dose of iron materials after 24 hours. . . . .	93
5.3 As <sub>3d</sub> HR-XPS spectra of (a) As(III) and (b) As(V) reacted with nZVI and iron oxide particles. The top spectra are those of pure sodium arsenite (NaAsO <sub>2</sub> ) and sodium arsenate (Na <sub>2</sub> HAsO <sub>4</sub> • 7H <sub>2</sub> O), respectively, which were precursors used to prepare As(III) and As(V) solutions. Initial As(III) or As(V) concentration was 100 mg/L; mass loading of iron materials was 5 g/L; reaction time was 24 hours. . . . .	95
5.4 Comparison of As <sub>3d</sub> XPS spectra of two replicate experiments. Experimental conditions: As(III) initial concentration 100 mg/L, nZVI dose 5 g/L, reaction time 24 hour. . . . .	97
5.5 Comparison of As(III) and As(V) removal rate with nZVI. The initial concentration of As(III) or As(V) was 100 g/L; the mass loading of nZVI was 5 g/L. . . . .	101
5.6. As <sub>3d</sub> HR-XPS spectra of nZVI reacted with As(III) for different times. Initial As(III) concentration was 100 mg/L; nZVI loading was 5 g/L. . . . .	103

5.7 As3d HR-XPS spectra of varying dose of nZVI reacted with 100 mg/L As(III) for 24 hours. . . . .	106
5.8 Fe2p XPS spectra of varying dose of nZVI reacted with As(III) solutions. Initial As(III) concentration was 100 mg/L; reaction time was 24 hours. . . .	107
5.9 Intensity ratios of the As2p <sub>3/2</sub> and As3d XPS spectra for the three samples in Figure 5.7. The raw intensities have been corrected by the relative sensitivity factors (S): S <sub>As2p</sub> = 31.5 and S <sub>As3d</sub> = 1.82. The value of S <sub>As2p</sub> was determined empirically in a previous study [30] and S <sub>As3d</sub> was from ref [45]. Using sodium arsenite (NaAsO <sub>2</sub> ) as a standard, we determined the intensity ratio of uniformly distributed arsenic species is 1.1 as indicated on the figure. . . .	110
5.10 Schematic diagram summarizing processes responsible for arsenic removal in As(III)-nZVI system in anoxic conditions. The relative scale of the core and shell components of nZVI are for illustration only and do not reflect actual dimensions. As(III) may be taken up from the aqueous phase by adsorption or co-precipitation. The solid-bound As(III) is oxidized rapidly at the oxide surface, and the As(V) formed may be reverted to As(III) at a slower rate. Some As(III) diffuses towards Fe(0) core and is reduced to elemental arsenic (As(0)) near the oxide/Fe(0) interface. . . . .	111

## LIST OF TABLES

### Tables

1.1 Iron oxide thickness for varying average nZVI particle diameters. . . . .	19
2.1 Specific IR energy ranges ( $\text{cm}^{-1}$ ) for the optimized detector/filter combination series . . . . .	30
3.1 Surface composition of samples analyzed by XPS . . . . .	44
3.2 Solution pH and $E_h$ before and after reactions . . . . .	51
4.1 Characteristics of various iron-based materials used in the study . . . . .	63
4.2 As(III) batch experiment conditions . . . . .	70
4.3 Curve-fitting parameters for As $2p_{3/2}$ and As $3d$ HR-XPS spectra and the relative areas of the peak components arising from different arsenic oxidation states . . . . .	71
4.4 Integrated peak areas of the XPS spectra taken for each sample . . . . .	72
4.5 Apparent elemental concentrations (at. %) for major elemental components . . . . .	73
5.1 Characteristics of iron-based materials used . . . . .	87
5.2 Comparison of XPS spectra of two replicate experiments in Figure 5.4 . . . . .	96
5.3 Solution pH and $E_h$ values, speciation of solid-phase arsenic and aqueous phase arsenic and iron concentrations . . . . .	102
5.4 Surface elemental composition determined by XPS analysis . . . . .	104

## ABSTRACT

Recent studies have shown that nanoscale zero-valent iron (nZVI) is very effective in the removal of highly toxic arsenic species such as As(III) and As(V) from both ground and surface water. Nonetheless, little is known about the sorption reaction mechanism of the As-treated nZVI particles. The present study carries out a more detailed analysis of these particular As sorption surface reactions. In our investigation we have used nZVI with a mean diameter of 60 nm, an average shell thickness in the range of 2.3-2.8 nm, and a surface area of 30 m<sup>2</sup>/g. High Resolution X-ray Photoelectron Spectroscopy (HR-XPS) using primarily As3d spectra has provided evidence of the presence of all major As species on nZVI: As(0), As(III), and As(V). HR-XPS Fe2p and O1s spectra also confirmed the presence of an oxyhydroxide (FeOOH) layer on freshly synthesized nZVI, which forms an intrinsic shell around the reactive metallic iron nanoparticle core. We also analyzed the reactions between nZVI and As(III) demonstrating for the first time depth-dependent distributions of multiple arsenic valence states within the iron nanoparticles. The stratified concentration profiles of arsenic species in nZVI showed novel aspects of the reactions between As(III) and nZVI. The results offered clear evidence of As(III) redox reactions within the nanoparticles. The distinct layers where As(V) and As(0) reside implied that As(III) oxidation and reduction can occur at different physical fronts. We also concluded that the ability to infuse arsenic into the solid phase of the iron nanoparticles renders nZVI a more voluminous sink for arsenic compared to the commonly used iron oxides nanoparticles. Infiltration of arsenic



induced by reactions with nZVI may offer an engineering methodology to encapsulate arsenic for remediation and waste disposal applications.

# CHAPTER I

## INTRODUCTION

### 1.1 Background

Arsenic is a well-known carcinogen and a very prevalent contaminant in groundwater around the world. It has been estimated that over 137 million people in more than 70 countries are affected by arsenic poisoning of drinking water [1]. Globally, some of the areas with the highest arsenic concentrations have been found in Chile, Argentina, Mexico, China, West Bengal (India), Bangladesh and Vietnam. In the case of Bangladesh, the arsenic contamination problem seems to be even more acute since a population estimated to be around 40 million people has access only to high risk or excessive arsenic-containing water [1].

The large amounts of arsenic in groundwater may come as a consequence of two important factors. The first is a change in the pH conditions ( $>8.5$ ), generally as a result of mineral weathering. The change in pH causes desorption of arsenic species from mineral oxides (e.g., Fe oxides). The second factor is the development of strongly reducing conditions at near-neutral pH, leading to the reductive dissolution of Fe oxides, Fe(II) and Fe(III) in most of the areas containing groundwater, resulting in an abundance of arsenic species [1].

Arsenic also occurs naturally in waters adjacent to sedimentary rocks [2], mineral deposits (replacing aluminum in crystal lattices) [3,4], volcanic rocks [5], volcanic emissions (yearly output has been estimated at  $3.1 \times 10^{10}$  g/year) [6], and geothermal areas [7], and is produced by anthropogenic means such as irrigation practices [8], mining/industrial wastes [9,10], and accidental spills of herbicides and pesticides in the agricultural sector [11,12,13].

Other significant natural sources of arsenic can be found in terrestrial air masses ( $0.46 \mu\text{g/L}$ )—from which As is globally distributed by rain—and unpolluted oceanic air masses ( $0.019 \mu\text{g/L}$ ) [14].

In the United States, groundwater supplies about one-third of the country's drinking water. However, there are many areas in the southwestern states where groundwater contains arsenic concentrations above those specified by the World Health Organization (WHO) guidelines, and the U.S. Environmental Protection Agency (EPA) drinking water standard of 10 ppb. The U.S. EPA has also reported that in some remote areas in the state of Alaska, well water contains higher levels of arsenic due to geochemical enrichment of landfills [15,16,17].

Based on recent spectroscopic and analytical techniques, arsenite (As(III)) has been suggested as the most prevalent species in groundwater samples. This raises both environmental and health concerns since As(III) is highly mobile and more toxic than the other arsenic species, i.e., arsenate (As(V)) and the metallic form (As(0)). Studies have shown that As(III) may be responsible for persistent neurological damages even if consumed in concentrations just above  $0.1 \text{ mg/L}$  [18]. Also, conservative estimates claim that As(III) is 25 to 60 times more toxic than As(V) [19]. The toxicity of arsenic

compounds depends on how fast the body can get rid of them. The residence time of arsenic compounds in the body usually follows this trend: arsine > As(III) > As(V) methylated arsenicals [20]. Some of the natural systems contributing to As(III) mobility in groundwater include reducing conditions in alluvial sediments where arsenic is predominantly sorbed by iron oxide. This kind of geochemical mechanism can increase the local concentration of As(III) up to a few hundred micrograms per liter. In addition, high levels of As(III) concentrations in both shallow aquifers and groundwater can be directly attributed to biological reaction mechanisms and arsenic sorption reaction kinetics [21].

The most common arsenic species present in environmental samples, mainly in groundwater, are inorganic species such as arsenious acid (As(III)) and arsenic acid (As(V)) and the organic species, monomethylarsonic acid (MMA) and dimethylarsinic acid (DMA) (see Figure 1.1). DMA is also predominant in marine waters [22]. Other arsenic species such as monomethyl-, dimethyl- and trimethyl arsine and trimethylarsine oxide have not yet been found in terrestrial waters [23].

Figure 1.1 also shows the most common form of arsenic in groundwater: arsenious acid (neutral molecules  $\text{H}_3\text{AsO}_3$  and  $\text{HAsO}_2$ ), at a constant pH of 8 ( $\text{pK}_a$  of 9.2).

In natural waters, the coexistence mechanism of both arsenic species and the rate of oxidation of As(III) to As(V) have been proposed but it is not yet well understood [24]. At neutral pH, the rate of oxidation of As(III) to As(V) is known to be very slow. However, the rate of oxidation in strong alkaline conditions proceeds steadily during several days [25].

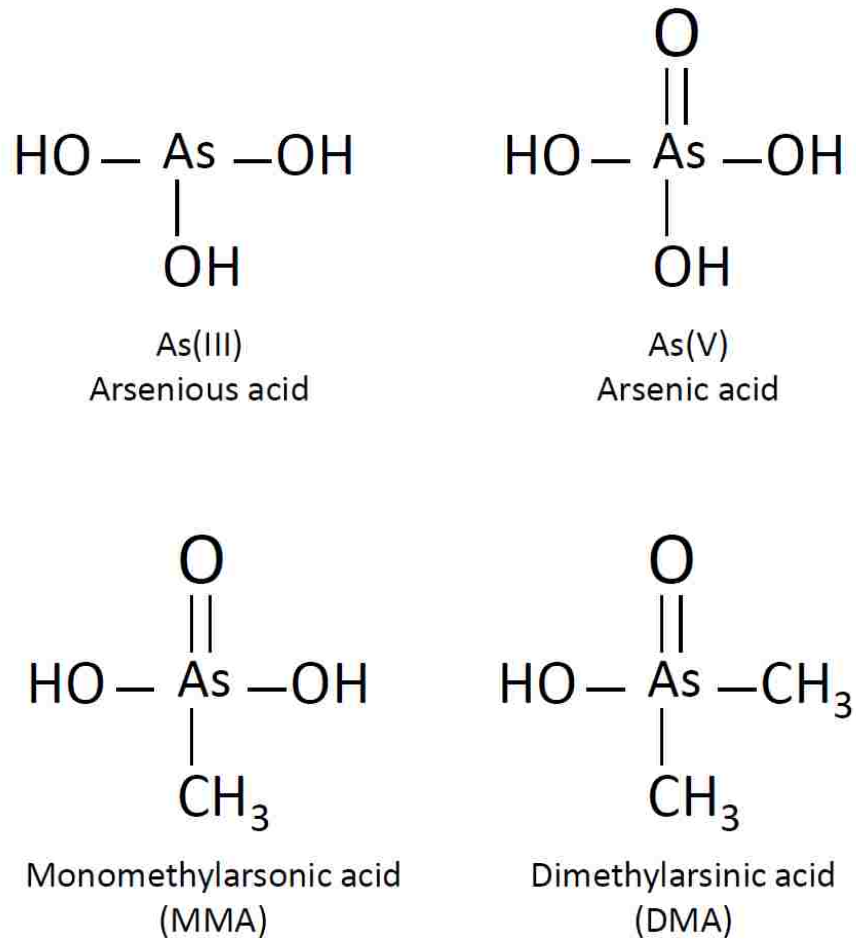


FIGURE 1.1 The concentration of inorganic (arsenious acid and arsenic acid) and organic arsenic species (MMA and DMA) occurring in natural waters plays an important role in the understanding of the mobility and toxicity of arsenic species in the ecological systems [adapted from ref. 26].

### 1.1.1 The influence of redox kinetics on arsenic speciation

The work done by Wersin, *et al.* [27] suggests that redox reactions act as a mechanism for controlling the chemical behavior of species such as arsenic. However, the presence of major elements like O, N, C, and Fe in natural waters control the redox potential, and as a consequence, the redox equilibrium is usually attained very slowly. It is generally believed that As(V) concentrations are greater than As(III) concentrations in oxidizing conditions, [28,29,30]. Oxidation of As(III) is a very slow reaction under aerobic conditions. For example, Johnson and Pilson [31] showed that the oxygenation of As(III) in seawater ranged from a couple of months to a year. As a practical matter, Yan *et al.* [32] concluded that the As(V)/As(III) ratio could be used as a consistent redox indicator for groundwater systems.

### 1.2 Adsorption reactions of arsenic species with Fe(0)

Adsorption reactions for As(III) may occur by means of electrostatic interactions such as Coulombic attraction, ion exchange and induced polarization, covalent bonding, and Van der Waals forces [26].

The work done by Livesey and Huang [33] and Matisoff *et al.* [34] was seminal in measuring the adsorption isotherms of As compounds on oxide minerals. It is generally accepted that Fe compounds interact most strongly with As in natural systems such as sedimentary rocks. In this regard, Fe minerals goethite and hematite have been extensively used in water remediation [35].

In order to reduce the health hazard derived from arsenic contamination in surface water and groundwater, a series of viable As-removing technologies have been implemented. Among these methods are the use of iron oxide materials, activated alumina, activated carbon, zeolites and nanoscale zero-valent iron (nZVI) to sequester arsenic from water. Recent studies suggest that nZVI—a very reactive nanomaterial frequently applied in hazardous waste treatment—is highly effective for arsenic removal in water. Moreover, nZVI is an affordable and environment-friendly reductant [36]. The small size of nZVI provides the advantage of a high surface-to-volume ratio, which allows mass transfer to and from the solid surface. The overall result is an increase of the reaction and sequestration capacity to remove contaminants over that of micron-sized or larger iron filings.

### 1.3 Role of Fe(0) in the electrochemical reduction of As(III) and As(V)

Figure 1.2 depicts a common example of a pe-pH (or Eh-pH) diagram, also known as a Pourbaix diagram, showing the predominant species of arsenic as well as their possible electrochemical reactions in an arsenic-iron system. The solid lines represent the domain where arsenic species prevailed and the dashed lines refer to the domain of iron species. The area encompassed by the two dotted lines is the stable water region. At any given time, when the redox potential is sufficiently low (e.g., pe values below the lower dotted line), water can be reduced to hydrogen gas [37].

From the pe-pH diagram in Figure 8 it can also be noticed that both forms of arsenic (III) and (V) exist under specific conditions. For example, As(III) in  $\text{H}_3\text{AsO}_3$  is the predominant species at pe values between 0 and -6, and pH = 9. At a neutral pH and a

pe value between -6 and -17, As(0) is the most stable species. On the hand, under oxic conditions and pe values just above zero As(V) is more abundant [37].

Among the iron species, Fe(0) is generally regarded as a strong electron donor that reaches stability around  $pe < -9$ . In aqueous solution, the outermost layer of Fe(0) nanoparticles tends to oxidize forming Fe(II) and hydrogen gas in anaerobic conditions. On the other hand, As(III) and As(V) are considered strong electron acceptors which can be reduced as seen on the pe-pH diagram (e.g., the As(V)—As(III) system has a higher pe boundary than the H<sub>2</sub>O—H<sub>2</sub> system) . Furthermore, the reduction of As(III) and As(V) to As(0) by Fe(0) is thermodynamically favored. Some of the equilibration rates and redox reactions of the arsenic and iron species may be slow due to the high energies of activation involved [37].

#### **1.4 Synthesis and use of iron nanoparticles for environmental remediation**

Zero valent iron (ZVI) particles and zero valent iron nanoparticles (nZVI) comprise some of the first attempts to effectively remove contaminants from surface and groundwater. In-situ remediation generally consisted of placing granular ZVI in permeable reactive barriers (PRB) systems [38–41]. Although in the long term the ZVI-PRB system has proved to be effective, it still faces a few practical limitations. One of the limitations is that large amounts —often estimated in tons— of the ZVI powder was necessary in relatively small PRB structures.

The small size of nZVI particles has made it easier for these nanoparticles to be injected by gravity flow or under pressure in-situ to the contaminated area. Once in the underground zone and depending on the conditions, nZVI can flow or remain suspended



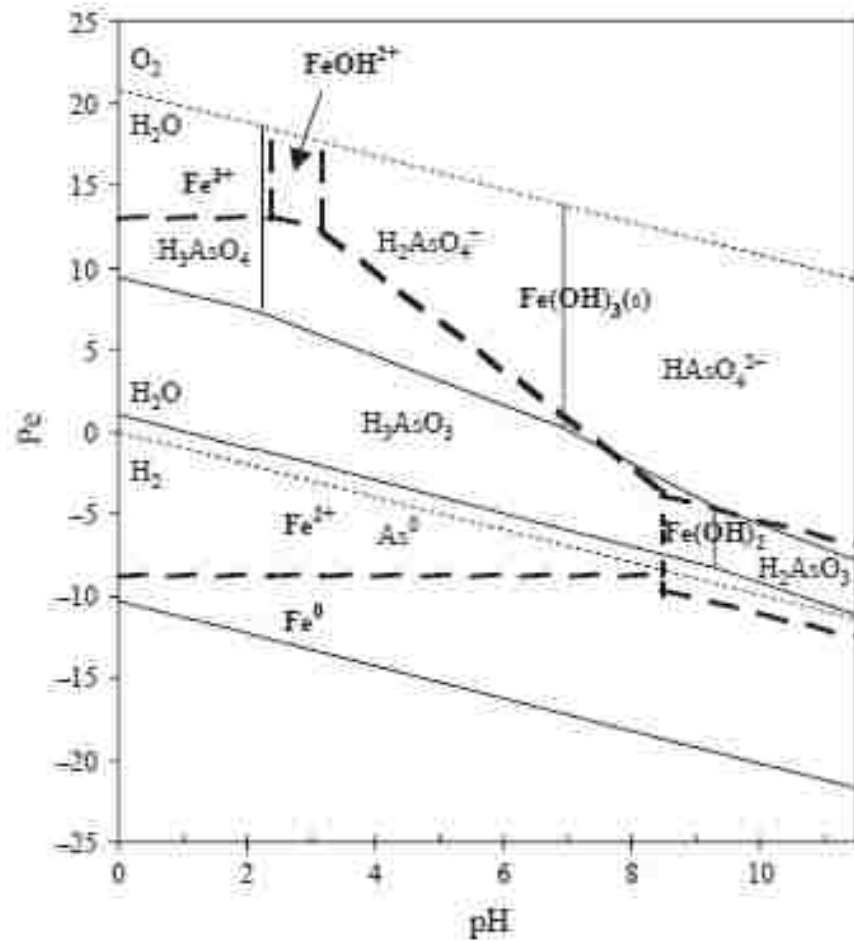


Figure 1.2 Depicting a pe-pH diagram for the As-Fe-H<sub>2</sub>O equilibrium and redox systems at 25 °C [42].

for a substantial period of time expanding the range of interactions (e.g., adsorption) with the contaminants. Also ex-situ nZVI applications can be carried out.

Fe(0) particles can be synthesized via two techniques, top-down and bottom-up. The first method involves mechanical milling or chemical etching of granular iron material to produce nanoparticles of iron. The second method involves the reduction of iron oxides (Fe(II) or Fe(III)) by means of sodium borohydride as depicted in Equation 1-1 [43]:



By using two of the most common reagents and no especial equipment, the synthesis of nZVI becomes economical feasible. Since the reaction takes place in aqueous conditions the iron on the surface of the nanoparticle oxidizes to Fe(II), i.e., Fe<sup>2+</sup> [42]:



Fe<sup>2+</sup> can be further oxidized to Fe<sup>3+</sup>:



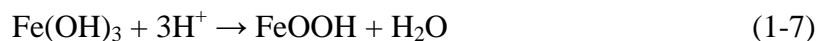
In addition to the small size of the nanoparticles, the structure also play an important role in the effective removal of As. The nZVI morphology is generally regarded as a core-shell combination with a zero-valent iron core enclosed by an iron

oxide/hydroxide shell. It is generally accepted that the iron oxide shell of the nZVI material is highly reactive, particularly when exposed to both oxygen and water and may even oxidize in air.

Also,  $\text{Fe}^{3+}$  reacts with  $\text{OH}^-$  or  $\text{H}_2\text{O}$  and to yield an oxyhydroxide layer [42]:



$\text{Fe}(\text{OH})_3$  can also dehydrate to form  $\text{FeOOH}$ :



These results constitute the foundation of a conceptual model of the nZVI nanoparticle structure and composition.

### 1.5 Issues and challenges concerning the use of nZVI for environmental remediation

Since 2001, considerable progress in research and development of nZVI for environmental remediation has been achieved. Field testing of nZVI for groundwater and soil remediation has demonstrated that these nanoparticles of iron can accelerate the degradation of organic contaminants such as organochlorine pesticides, chlorinated organic solvents, and polychlorinated biphenyls (PCBs). The chemical degradation process of the halogenated hydrocarbons is sped up by the action of metallic iron as an effective electron donor [42]:



However, this new technology still faces some significant challenges.

### 1.5.1 Materials chemistry: economics

The whole concept and modeling of nZVI technologies depends on scaling up the synthesis of nZVI material to sufficiently large quantities that allow production of nZVI to become economical feasible (e.g., \$10-25/pound). In 2010, the considerable use of nanomaterials to address water and air purification [43-46] had an annual market value of \$2.4 billion [47]. Although the latter figure may look impressive, the marketability of nZVI currently represents only a fraction of the total investment in water remediation treatments and environmental technology programs. In addition, other processes involving quality control, particle size, mobility, surface charge and reactivity of nZVI materials should be optimized.

### 1.5.2 Environmental concerns

Although the effectiveness of nZVI in removing halogenated aromatic contaminants, pesticides, and dioxins., and also heavy metal and metalloid contaminants in groundwater has been well documented, more studies are needed that address the complex chemistry and reaction mechanisms. Details on competing contaminants, ionic strength, and pH at the Fe(0) nanoparticle-water interface must be properly considered [42].

### 1.5.3 Geochemistry

Geochemistry in the subsurface environment can affect nZVI performance. Additional studies are needed that encompass nZVI physical processes (e.g., sorption and desorption) with contaminants present in surfaces and groundwater, and account for the long term effects of porous media on the nZVI mobility in both soil and sediments [42].

#### 1.5.4 Environmental impact

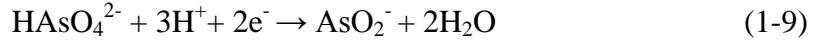
Impact studies have shown that iron is one the most used natural occurring elements, in fact only carbon, oxygen, hydrogen and calcium are consumed in larger quantities. Therefore, as more quantities of nanoparticles of iron are being used for the effective removal of contaminants in surface and groundwater, it should be a priority to demonstrate their positive effects on the environment. In addition, any potential toxic effect of the nZVI used in ecosystems around the world should not be overlooked [42].

#### 1.6 Equilibrium potential and pH effect of arsenic adsorption on nZVI

Recent studies have shown that the two predominant mechanisms by which both As(III) and As(V) species are removed in the presence of iron filter materials is via the formation of monodentate and bidentate complexes [48-50]. Also, the removal of arsenic directly depends on how much of the arsenic is transferred to adsorption sites, in other words, the process is driven by the ratio of the number of adsorbed species to the numbers of adsorption sites, thus becoming first order with respect to arsenic concentration [49, 51]. Meng *et al.*, [52] suggested that the removal of As(III) species proceeds via a pseudo-first order reaction ( $d[As]/dt = -k[As]$ ). For both species of arsenic, the binding strength to iron complexes depends on their concentration in solution and the solution pH. For instance, at a neutral and alkaline pH, As(III) tends to bind to goethite and ferrihydrite, while As(V) behaves in the same manner at sub-neutral pH [53-56]. It is important to understand the overall chemical behavior and, in particular, the redox mechanism of both arsenic species, since it can yield information on how strongly and at what rate a species with a specific oxidation state can be adsorbed or released from the

iron oxide or nZVI materials. Studies have confirmed that the equilibrium potential of the As(III)/As(V) redox mechanism depends on the concentration of the species involved. Reduction of As(V) to As(III) is expected to happen at pH = 9.5 and in the vicinity of the surface of the iron species (non-corroding conditions) [57].

The reduction of As(V) is given by equation (1-9):



At 25°C the equilibrium potential ( $E_{\text{eq}}$ ) for this reaction is given by equation (1-10) [58]:

$$E_{\text{eq}} = 0.609 - 0.0887 \text{ pH} + 0.0295 \log \frac{[\text{HAsO}_4^{2-}] \gamma_{\text{As(V)}}}{[\text{AsO}_2^-] \gamma_{\text{As(III)}}} \quad (1-10)$$

where  $[\text{HAsO}_4^{2-}]$  and  $[\text{AsO}_2^-]$  represent the molar concentrations, and  $\gamma_{\text{As(V)}}$  and  $\gamma_{\text{As(III)}}$  are the activity coefficients of each arsenic species. The concentrations of As(III) and As(V) at the iron oxide layer depends on the difference in potential between the iron at the surface and the bulk solution ( $\psi_s$ ). The ratio of As(III) with a charge of  $m$  to As(V) with a charge of  $n$  at the iron surface is given by [58]:

$$\left[ \frac{\text{As(III)}}{\text{As(V)}} \right]_{\text{surface}} = \left[ \frac{\text{As(III)}}{\text{As(V)}} \right]_{\text{bulk}} \exp \left[ \frac{(n - m)F\psi_s}{RT} \right] \quad (1-11)$$

Reduction of As(V) species that are bound to the iron oxide shell in nZVI will affect the equilibrium potential of the As(III)/As(V) redox couple. Figure 1.3 depicts how differences in binding strength contribute to the changes in standard reduction potentials

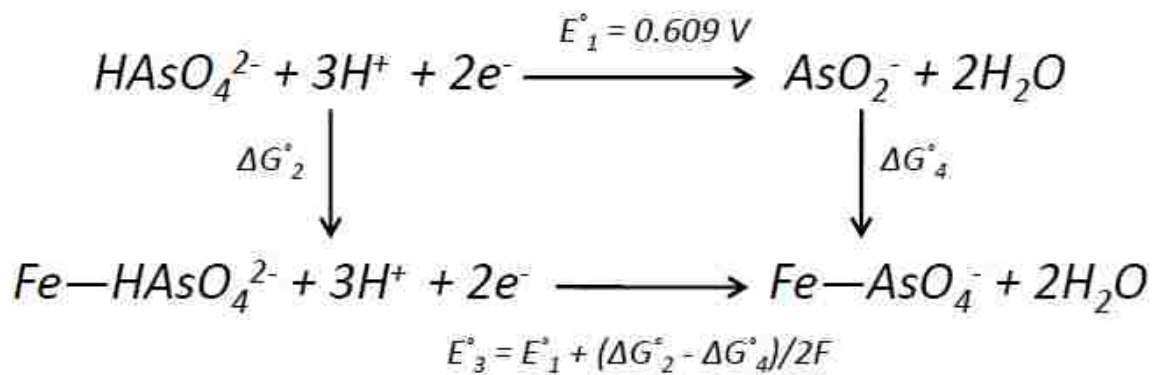


Figure 1.3 Thermodynamic cycle depicting the reduction of As(V) in aqueous solution. As(III) and As(V) can be bound to the iron oxide layer coating the iron metal surface [adapted from reference 58].

( $E^\circ$ ) for both free and bound species of As(V). For example, having stronger bound As(III) species to the nZVI surface means that  $\Delta G_2^\circ > \Delta G_4^\circ$ , and thus  $E_3^\circ > E_1^\circ$ . The opposite effect is true for As(V), resulting in bound As(V) to be reduced at higher potentials than aqueous As(V) [59].

Thus, overall the nZVI reactivity is directly related to its iron-oxide shell thickness and great effort has been directed to quantitative and structural characterization of this oxide shell.

### 1.7 Oxide layer thickness in core-shell nZVI

Structural details of the nZVI oxide layer thickness have been achieved with the use of spectroscopic tools such as High Resolution X-ray photoelectron spectroscopy (HR-XPS) and transmission electron microscopy (TEM). To successfully measure the oxide layer thickness using XPS, a geometric correction must be introduced to compensate for the nZVI spherical topography [60-62]. It is well established that for any metal with a flat surface covered by a metal oxide layer, the thickness of the oxide layer is given by equation (1-12) [63]:

$$d = \lambda_{ox} \cos \theta \ln \left( \frac{N_{me} \lambda_{me}}{N_{ox} \lambda_{ox}} \cdot \frac{I_{ox}}{I_{me}} + 1 \right) \quad (1-12)$$

where  $\lambda$  is the inelastic mean free path,  $\theta$  is the detection angle,  $I_{me}$  and  $I_{ox}$  are the intensities of the metal and oxidized metal, respectively,  $N$  is the number of atoms per unit volume, and  $d$  is the thickness of the oxide layer.

In the case of nZVI, the curved surface of the nanoparticle causes variations in the relative intensity of photoelectrons (produced by exposure to X-rays) that originate from both the core and shell. For a detector placed at  $90^\circ$  with respect to the surface of the



sample, those photoelectrons escaping from the edges of an nZVI particle will seem to originate mainly from the shell. On the other hand, photoelectrons escaping from the apex will primarily emanate from both the core and shell. For an nZVI particle with uniform shell thickness the equation that defines its effective thickness,  $d^{eff}$ , must include the necessary geometrical corrections for the inelastic mean free path [6]. Calculations of the attenuation length,  $\lambda_{AL}$ , are based on equation (1-13) [63].

$$\lambda_{AL} = 0.316a^{3/2} \left\{ \frac{E}{Z^{0.45} [\ln(E/27) + 3]} + 4 \right\} \quad (1-13)$$

where  $a$  is the lattice parameter in nm,  $E$  is the kinetic energy, and  $Z$  is the average atomic number. For iron photoelectrons moving through the metallic core and oxide shell,  $\lambda_{me} = 1.10$  nm and  $\lambda_{ox} = 1.42$  nm.

As demonstrated by Martin *et al.*, [64] the effective thickness values of the nZVI oxide layer, using the corresponding geometric corrections, are shown in Table 1.1. On average, the iron oxide shell thickness was determined to be between 2.3 - 2.8 nm.

### 1.8 nZVI reaction mechanisms

Some of the significant challenges in the investigation of nZVI involve the fact that the reaction mechanisms of arsenic on nZVI are not well understood. Some of the works done using nZVI have demonstrated to a large extent the great reducing potential that these nanoparticles of iron have on various inorganic contaminants. Thus, it is often expected that both forms of arsenic (V) and (III) behave in the same manner when reacted with nZVI. However, the reduction of As(V) to As(III) has been suggested to be kinetically slow. In addition, —prior to our own investigation, which provides direct evidence of the formation of elemental arsenic upon reaction with nZVI — the presence

Table 1.1 Iron oxide thickness for varying average nZVI particle diameters [64].

diameter (nm)	10	20	30	40	50	60	100	200
Shell thickness (nm)	2.85	2.57	2.49	2.45	2.42	2.40	2.38	2.36

of As(0) has been speculated about, but not substantially corroborated [65-67]. Thus, several studies suggest that oxidation of As(III) by nZVI is the predominant reaction [68,69].

The majority of these studies rely on solution-phase arsenic analysis, and there are fewer studies investigating arsenic speciation on nZVI surfaces that can provide more direct evidence of the reactions between nZVI and arsenic.

### **1.9 Scope of thesis**

The objective of this thesis is to examine surface reaction mechanisms of arsenate and arsenite with nZVI by using HR-XPS, which can provide valuable information about nZVI core-shell structure, elemental valence states, and the abundance of various arsenic species on nanoparticle surfaces. The results are interpreted in light of the fundamental structure of nZVI, and the implications of these findings for arsenic treatments and remediation are discussed.

## REFERENCES FOR CHAPTER I

1. Smedley, P. L.; Kinniburgh, D. G. *Appl. Geochem.* **2002**, *17*, 517.
2. U.S. Geological Survey, *Water-Resources Investigations Report*, 89-4104, Denver, **1989**.
3. Onishi, H.; Snadell, E. B. *Geochim. Cosmochim.* **1955**, Acta, *7*, 1.
4. Fuller, C. C.; Davis, J. A.; Claypool-Frey, R. G. Partition of arsenic oxides in Whitewood Creek, S.D., presented at Division of Environmental Chemistry. American Chemical Society Meeting, Denver, 1987.
5. Welch, A. H.; Lico, M. S.; Hughs, J. L. *Ground Water*, **1988**, *26*, 333.
6. Walsh, P. R.; Duce, R. A.; Fasching, J. L. *J. Geophys. Res.* **1979**, *84*, 1719.
7. Thompson, J. *Environ. Geol.* **1979**, *3*, 13.
8. Sonderegger, J. L.; Ohguchi, T. *Environ. Geol. Water Sci.* **1988**, *11*, 153.
9. Mok, W. M.; Wai, C. M. *Environ. Sci. Technol.* **1990**, *24*, 102.
10. Spackman, L. K.; Hartman, K. D.; Harbour, J. D.; Essington, M. E. *Environ. Geol. Water Sci.* **1990**, *15*, 83.
11. Artiola, J. F.; Zabelk, D.; Johnson, S. H. *Waste Manage.* **1990**, *10*, 73.
12. Hess, R. E.; Blanchar, R. W. *Soil Sci. Soc. Am. J.* **1976**, *40*, 847.
13. Jackson, D. R.; Levin, M. *Water, Air, Soil Pollut.* **1979**, *11*, 3.
14. Andreae, M. O. *J. Geophys. Res.* **1980**, *85*, 4512.
15. World Health Organization, *Guidelines for drinking water quality, Voll: Recommendations*, 2<sup>nd</sup> ed.; World Health Organization, Geneva, 1993.
17. U.S. Environmental Protection Agency, *National Primary Drinking Water Standards*, 2003, EPA 816-F-03-016.
18. Welch, A. H.; Westjohn, D. B.; Helsel, D. R.; Wanty, R. B. *Ground Water* **2000**, *38*, 589.

18. Grantham, D. A.; Jone, J. F. *J. Am. Water Well Assoc.* **1978**, 707
19. Morrison, G. M. P.; Batley, G. E.; Florence, T. M. *Chem. Br.* **1989**, 25, 791.
20. Puttemans, F.; Massart, D. L. *Anal. Chim. Acta.* **1982**, 141, 225.
21. Environmental Protection Agency, *Health Assessment Document for Inorganic Arsenic*, 1984, EPA-600/8-83021F.
22. Ridley, W. P.; Dizikes, I. J.; Wood, J. M. *Science.* **1977**, 197, 329.
23. Sturgeon, R. E.; Siu, K. M.; Willie, S. N.; Berman, S. S. *Analyst.* **1989**, 114, 1393.
24. Agget, J.; Kriegman, M. R. *Water Res.* **1988**, 22, 407.
25. Kohltoff, L. M. *Anal. Chem.* **1921**, 60, 393.
26. Korte, N. E.; Fernando, Q. *Critic. Rev. Environ. Contrl.* **1991**, 21, 1
27. Wersin, P.; Hohener, P.; Giovanoli, R.; Stumm, W. *Chem. Geol.* **1991**, 90, 233.
28. Seyler, P.; Martin, J.-M. *Environ. Sci. Technol.* **1989**, 23, 1258.
29. Eary, L.E.; Schranke, J.A. Rates of inorganic oxidation reactions involving dissolved oxygen. In: Melchior, D.C., Bassett, R.L. (Eds.), *Chemical Modeling of Aqueous Systems II*. ACS Symposium Series. American Chemical Society, Washington, DC, 1990, 379.
30. Kuhn, A.; Sigg, L. *Limnol. Oceanog.* **1993**, 38, 1052
31. Johnson, D.L.; Pilson, M.E.Q. *Environ. Lett.* **1975**, 8, 157.
32. Yan, X.-P.; Kerrich, R.; Hendry, M.J. *Geochim. Cosmochim.* **2000**, Acta 64, 2637
33. Livesey, N.T.; Huang, P.M. *Soil Sci.* **1981**, 131, 88.
34. Matisoff, G.; Khourey, C.J.; Hall, J.F.; Varnes, A.W.; Strain, W.H. *Ground Water.* **1982**, 20, 446.
35. Edwards, M. *J. Am. Water Works Assoc.* **1994**, 86, 64.
36. Welch, A H.; Lico, M. S.; Hughs, J. L. *Groun. Water*, **1988**, 26, 333.
37. Bang, S.; Johnson, M. D.; Korfiatis, G. P.; Meng, X. *Water Research.* **2005**, 39, 763.

38. Reynolds, G.W.; Hoff, J. T.; Gillham, R.W. *Environ. Sci. Technol.* **1990**, 24, 135.
39. Gillham, R.W.; O'Hannesin, S. F. *Goundwater*, **1994**, 32, 958.
40. Gavaskar, A. R.; Gupta, N.; Sass, N. M.; Janoy, R. J.; O'Sullivan, D. *Permeable Barriers for Goundwater Remediation—Design, Construction, and Monitoring*, Battelle Memorial Institute, Columbus, OH, 1998.
41. Gu, B. T.; Phelps, J.; Liang, L.; Dickey, M. J.; Roh, Y.; Kinsall, B. L.; Palumbo, A. V.; Jacobs, G. K. *Environ. Sci. Technol.* **1999**, 33, 2170.
42. Li, X-Q, Elliott, D. W.; Zhang, W.-X. *Crit. Rev. Sol. State Mater. Sci.* **2006**, 31, 111.
43. Wang, C.; Zhang, W. *Environ. Sci. Technol.* **1997**, 35, 4922.
44. Fujishima, A.; Rao, T. N.; Tryk, D. A.; *J. Potochem. Photobiol. C: Photochem. Rev.* **2000**, 1, 1.
45. Kamat, P. V.; Huehn, R.; Nicolaescu, R. *J. Phys. Chem. B.* **2002**, 106, 788.
46. Masciangioli, T.; Zhang, W. X. *Environ. Sci. Technol.* **2003**, 36, 102A.
47. BCC Research, *Nanotechnology in Environmental Applications* (RNAN039A).
48. Lackovic, J. A.; Nikolaidis, N. P.; Dobbs, G. M. *Environ. Eng. Sci.* **2000**, 17, 29.
49. Farrell, J.; Wang, J. P.; O'Day, P.; Conklin, M. *Environ. Sci. Technol.* **2001**, 35, 2026.
50. Su, C.; Puls, R. W. *Environ. Sci. Technol.* **2001**, 35, 1487.
51. Melitas, N.; Farrell, J.; Wang, J. P.; Conklin, M.; O'Day, P. *Environ. Sci. Technol.* **2002**, 36, 2074.
52. Meng, X.G., Bang, S., Korfiatis, G.P. *Water Res.* **2000**, 34, 1255.
53. Pierce, M. L.; Moore, C. B. *Water Res.* **1982**, 16, 1247.
54. Raven, K. P.; Jain, A.; Loeppert, R. H. *Environ. Sci. Technol.* **1998**, 32, 344.
55. Manning, B. A.; Fendorf, S. E.; Goldberg, S. *Environ. Sci. Technol.* **1998**, 32, 2383.
56. Jain, A.; Raven, K. P. Loeppert, R. H. *Environ. Sci. Technol.* **1999**, 33, 1179.

57. Uhlig, H. H.; Revie, R. W. *Corrosion and Corrosion Control*, 3<sup>rd</sup> ed.; John Wiley: New York, 1985.
58. Pourbaix, M. *Atlas of Electrochemical Equilibria*; Pergamon Press: Oxford, 1966.
59. Melitas, N.; Coklin, M.; Farrel, J. *Environ. Sci. Technol.* **2002**, 36, 3188
60. Mohai, M.; Bertoli, I. *Surf. Interface Anal.* **2004**, 36, 805-808.
61. Leupin, O. X.; Hug, S. J. *Water Res.* **2005**, 39, 1729.
62. Mohai, M. *XPS Multiquant Users Manual* 2005.
63. Cumpson, P.; Seah, M. *Surf. And Interface Anal.* **1997**, 25, 430-446.
64. Martin, J. E.; Herzing, A. A.; Yan, W. L.; Li, X. Q.; Koel, B. E.; Kiely, C. J.; Zhang, W. X., *Langmuir* **2008**, 24, 4329.
65. Li, X.; Zhang, W. *Langmuir* **2006**, 22, 4638-4642.
66. Su, C. M.; Puls, R. W. *Environ. Sci. Technol.* **2001**, 35, 1487.
67. Kanel, S. R.; Manning, B.; Charlet, L.; Choi, H. *Environ. Sci. Technol.* **2005**, 39, 1291.
68. Hug, S. J.; Leupin, O. *Environ. Sci. Technol.* **2003**, 37, 2734.
69. Mohai, M. *Surf. Interface Anal.* **2004**, 36, 828-832.

## CHAPTER II

### EXPERIMENTAL METHODS

#### 2.1 Characterization and Analysis of As-treated nZVI using High-Resolution X-ray Photoelectron Spectroscopy

Dried samples of nZVI after reaction with both As(III) and As(V) were characterized using High Resolution X-ray Photoelectron Spectroscopy (HR-XPS), carried out on a Scienta ESCA 300 spectrometer equipped with an 8 kW-rotating anode yielding monochromatic AlK $\alpha$  ( $h\nu = 1486.7$  eV) radiation (Figure 2.1). The dried As-treated nZVI samples were mounted on a stainless steel stub coated with conductive carbon tape and transferred to the ESCA 300 analysis chamber ( $5.0 \times 10^{-9}$  Torr). Samples were analyzed at C1s, O1s, As3d, and Fe2p regions, which account for the major elements present at the surface.

Each spectrum was calibrated against the binding energy (BE) of adventitious carbon detected in the C1s region (284.6 eV). Curve fitting was carried out using the CASA XPS MFC application software (version 2.3.12.8). A Shirley background was used to account for inelastic scattering and all peaks were described using a Gaussian/Lorentzian ratio of 70/30. The As3d $_{5/2}$  and As3d $_{3/2}$  components of the As3d spin orbit-split doublet peaks were fixed at a constant intensity ratio of 3:2 and a constant separation of 0.70 eV.



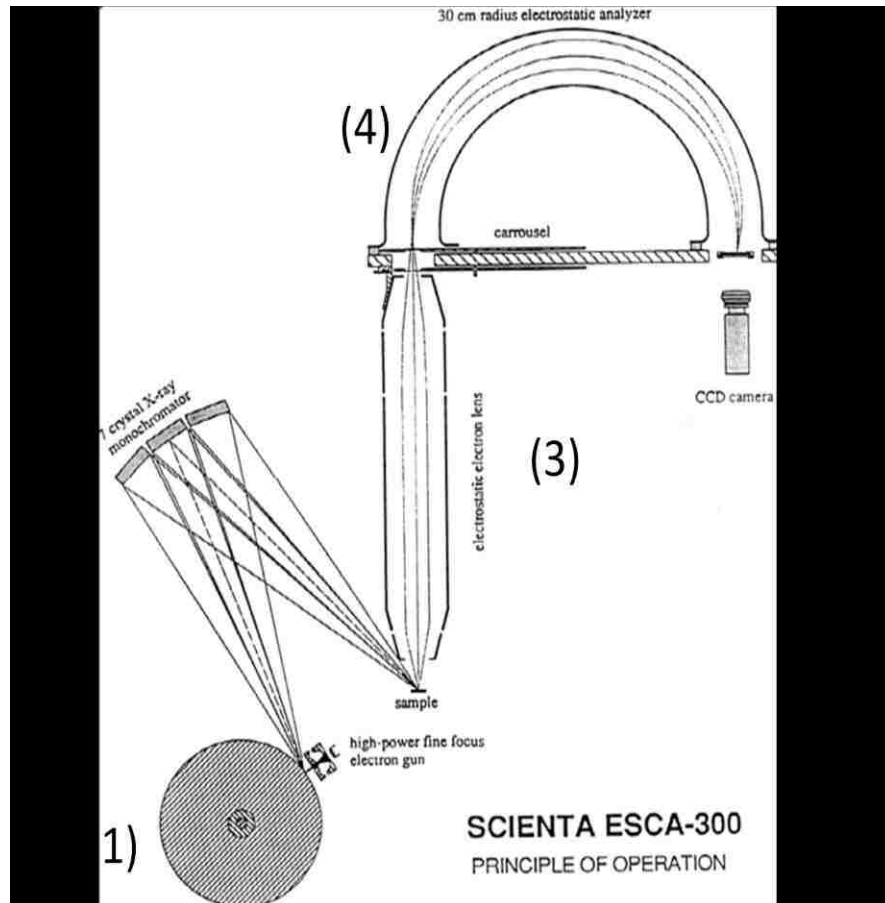


Figure 2.1 Schematic depicting the ESCA 300 main components [1]

### 2.1.1 X-ray source

The Scienta ESCA 300 is equipped with a rotating anode made of titanium alloy. The maximum operational speed is 10000rpm. While the anode rotates, differential and turbo pumping provide the high vacuum created in the chamber. The source of the monochromated Al K $\alpha$  radiation (1486.7eV) is produced when the electron beam from a Pierce-type gun is directed onto an Al band on the circular edge of the anode. The rotating anode is capable of dissipating electron beams whose power range from 5 kW to 8 kW. The power for this electron beams depends on the square root of their rotational speeds that can go from 4000 rpm to 10000 rpm.

### 2.1.2 Monochromator

The monochromator is a collection of  $\alpha$ -quartz crystals that collects the X-rays from the rotating anode and subsequently projects them onto the surface of the sample. Any spherical aberration is eliminated by the toroidal bend in the crystals. The crystals are also protected with a beryllium foil that prevents damage from incident electrons. In the same manner an Al foil separates the analysis chamber from the preparation chamber to prevent any electrons from the monochromator to hit the sample and become part of the spectral background [1].

### 2.1.3 Electron lenses

The lenses main purpose is to collect the photoelectrons reflected off from the sample and focus them on the aperture at the entrance of the hemispherical energy analyzer. The lenses can operate in two modes: High Transmittance where the lenses

accept the whole range of the X-rays coming from the sample. The other mode is High Spatial Resolution where the lenses accept only a fraction of the X-rays from the surface of the sample.

#### **2.1.4 Hemispherical Electron Energy Analyzer (HMA)**

The HMA in the ESCA 300 has an average radius of 300 mm and in between its hemispheres the separation is 100 mm. The seven pass energies remain constant during operation and the eight-slit pairs selection allow a high energy resolution and high electron flux to continue steadily while taking data [1].

#### **2.1.5 Multichannel detector**

The multichannel detector consists of a P10 phosphor and a CCD TV camera, and two additional microchannel plates. Of particular interest is that electrons striking the screen of the CCD camera produce a flash of light that integrates several pixels. This situation could give a misreading in the accumulation of count rates. Since saturations of this type occur predominantly at higher count rates for the lower pass energies, there is a characteristic dispersing of the photoelectrons striking a larger area of the detector with the immediate consequence of reducing the accumulation of light flashes on the same camera pixels. The multichannel detector array is positioned at the exit aperture of the HMA [1].

## 2.2 Considerations in building a new FTIR apparatus (Improving noise % transmittance)

### 2.2.1 Detector/filter combination

The original idea and design of the new FTIR apparatus was conceived by Prof. C.J.S.M. Simpson. Some of the initial testing and signal-to-noise data acquisition was performed by S. J. Burke, D. Klevisha, R. S. Jackson, and T. J. Johnson at Bruker facilities. The custom-made optical devices such as lenses and filters for the detectors were provided by Crystan Ltd and Northumberland Optical Coaters respectively.

The reason for optimizing our FTIR apparatus is most apparent in the need to reduce the % noise transmittance to levels that can give us a reliable reading when measuring small fractions (about 10%) of peroxy radicals distributed among the original molecules on the surface of Self Assembled Monolayers (SAMs). One way to reduce the % noise transmittance is by coating our Mercury-Cadmium-Tellurium (MCT) detectors with a special filter that is capable to reduce the background noise from the IR source. The latter approach can allow us to obtain measurements at very specific energy ranges (Table 2.1).

The detector/filter combination was previously tested by R. Jackson at Bruker Optics in a fully evacuated FTIR. The results demonstrated that at a resolution of  $4\text{ cm}^{-1}$ , the light source attenuated by a factor of 10, and after only 35 scans ( $\sim 15\text{ sec}$ ) the percent noise transmittance was 0.001 and after 192 scans it was reduced to 0.0004. These results showed that both conditions for obtaining the desirable % noise transmittance and obtaining them in real time were possible. The results also stand when compared to those found in literature. For example, Celio and White measuring the % noise transmittance in

Table 2.1 Specific IR energy ranges ( $\text{cm}^{-1}$ ) for the optimized detector/filter combination series

DETECTOR	SAMPLE	RANGE ( $\text{cm}^{-1}$ )	SETTINGS	FILE	Preamp. ID
DTGS	Polystyrene	4000 – 500	Room Temp, 7V – 2.35A, Preamp. 1, Signal Gain 1	DTGSSP DTGSINT	—
MCT E5829 10 – 2.0	Polystyrene	1650 – 550	LN <sub>2</sub> cooled, 8V – 2.5A, Preamp. 1, Signal Gain 1, Yellow coating	E5829SP E5829INT	I2143 ECL 5 FI023441 DP
UNKNOWN ID	Polystyrene	—	LN <sub>2</sub> cooled, 8V – 2.5A, Preamp. 1, Signal Gain 1, Purple coating	—	—
MCT D3542 D*9(10)	Polystyrene	2000 – 1500 3150 – 3000	LN <sub>2</sub> cooled, 8V – 2.5A, Preamp. 1, Signal Gain 1, Yellow coating.	D3542SP D3542INT	I2143 ECL05 FI040929
InSb	Polystyrene	1939 (overtone) 4000 – 3652 (surface water)	LN <sub>2</sub> cooled, 8V – 2.5A, Preamp. 1, Signal Gain 1	INBSP INSBINT	I2143 ECL 5 FI023441
MCT D3296 D*6(10)	Polystyrene	3700 – 3550 2500 – 2250 1400 – 650	LN <sub>2</sub> cooled, 8V – 2.5A, Preamp. 1, Signal Gain 1, Yellow coating.	D3296SP D3296INT	I2143 ECL 5 FI022611

their purge FTIR (purging time: ~ two weeks) at a resolution of  $4\text{ cm}^{-1}$ , light attenuated by a factor of 10, and after 2000 scans (~ 14 min) obtained a % noise in transmittance of 0.0026 (Figure 2.2) [2]. Since the lifetime of any radical is particularly short, Celio *et al.* approach would not be convenient for our experimental purposes.

From Figure 2.2 we can also see that up to 192 scans the decrease in noise % correlates linearly with  $N^{-1/2}$ , where N is the number of scans. Even though the decrease in noise % continues, it seems that between 200 and 500 scans the rate at which the noise % decreases starts to slow down to reach an apparent limit just below 0.0004%. The situation persists besides the fact that the FTIR spectrometer has been equipped with the filter/detector combination. So this limitation might be due to the intrinsic characteristics of the evacuated FTIR spectrometer. Moreover, the test using the purged FTIR shows that after 50 scans the noise % increases rather than decreases, demonstrating the susceptibility to technical limitations when using this approach. For instance, Stallard *et al.* [3] have found out that it takes several days (~ two weeks) to adequately purge a commercial Nicolet FTIR spectrometer with 0.1 part per million (ppm) of  $\text{N}_2$  down to a water concentration of 1ppm. And this was achieved only after placing the entire FTIR spectrometer inside a customized glove box.

In order to achieve the necessary noise % transmittance level requires that our new FTIR apparatus be fully evacuated. One way to achieve this is by housing the FTIR and the main optical parts such as lenses, polarizers, and mirrors in compact aluminum boxes (Figure 2.3, Figure 2.4). The design of the boxes may permit use of turbo pumps to evacuate the entire optical system to proper pressures.

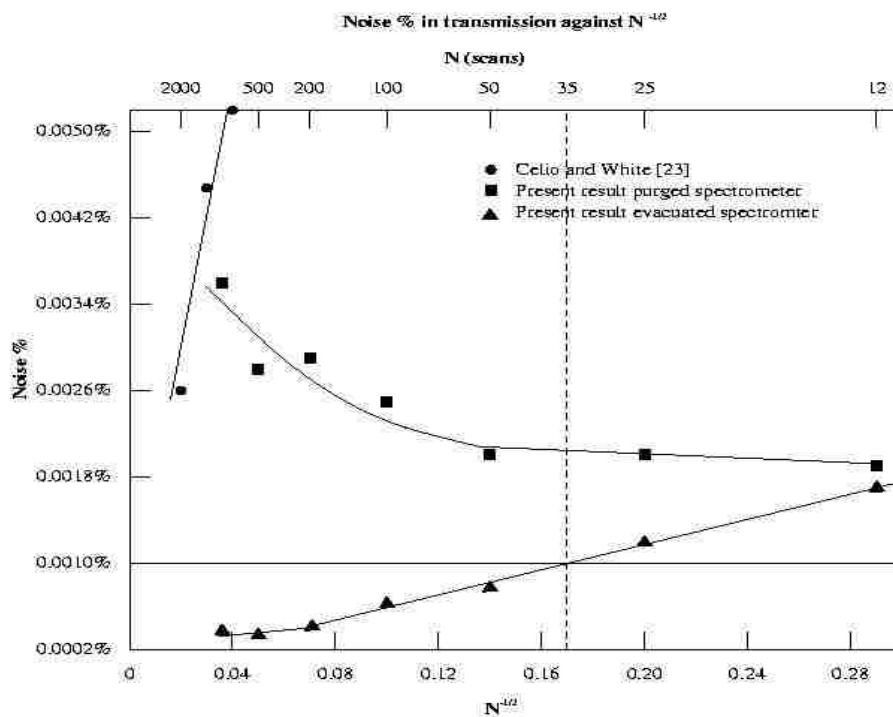


Figure 2.2 Reducing % noise transmittance in an FTIR apparatus: ■) purging with N<sub>2</sub> and ▲) evacuating the system with the use of turbo pumps.

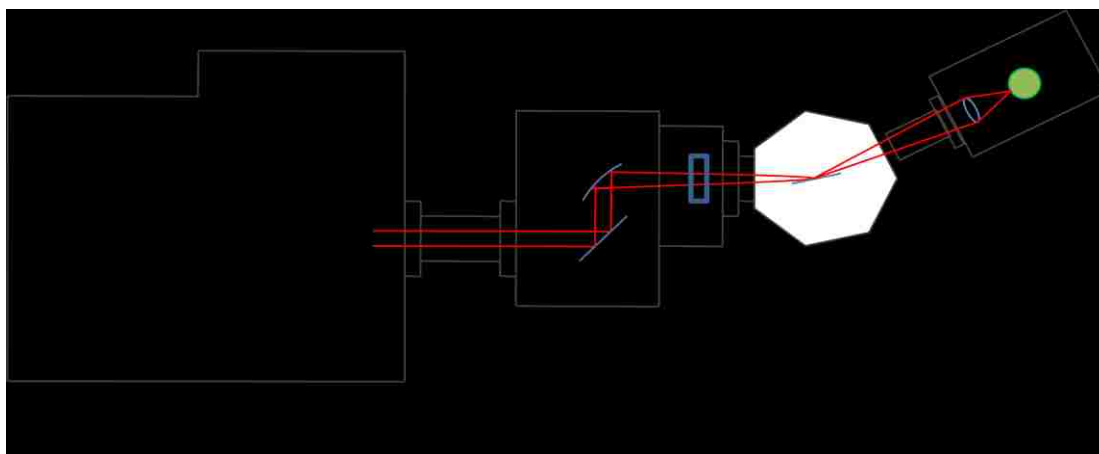


Figure 2.3 The Optimized FTIR Optical System consists of: **1)** Evacuated Vector 22 FTIR. **2)** Evacuated Mirror Box, **3)** Evacuated Polarization Flipper (small blue-edged rectangle) Box, **4)** UHV Sample Chamber, and **5)** Evacuated Filter/Detector Combination (green circle) Box. The red lines represent the optical path of the IR and laser source.



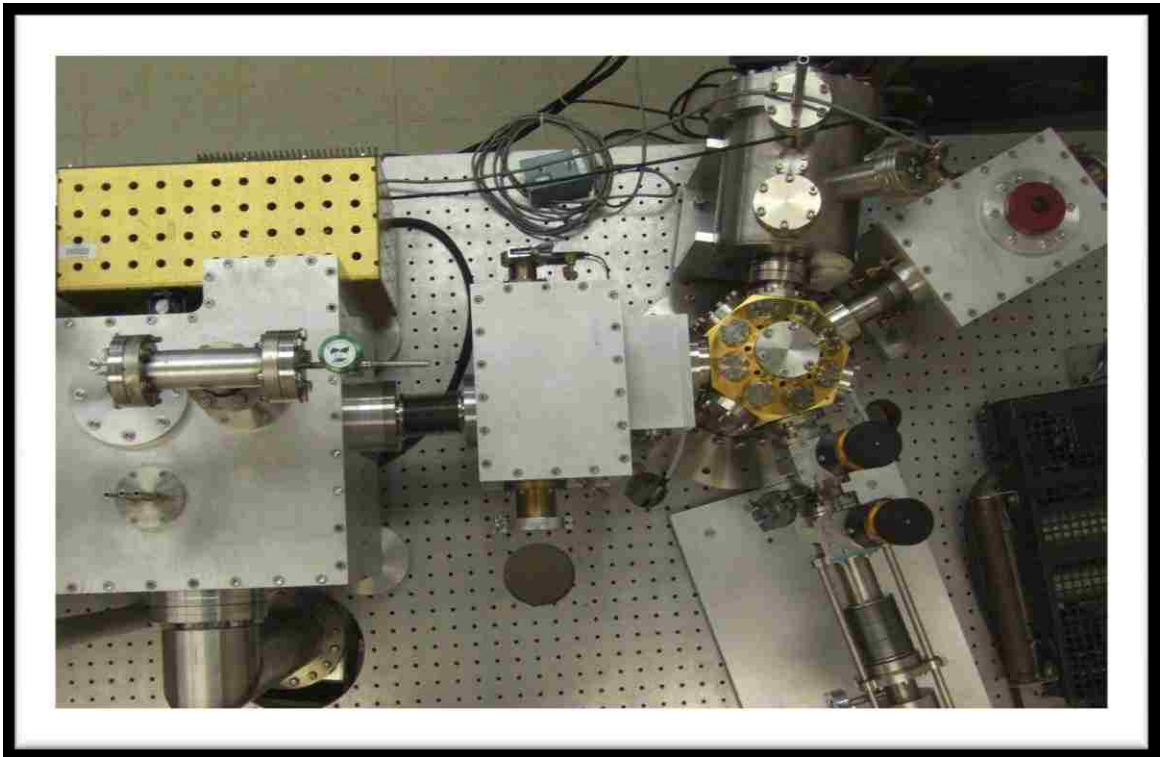


Figure 2.4 Actual FTIR Optical System

### 2.2.2 Incident source light and SAMs surface

Evacuating the FTIR apparatus can definitely improve the signal-to-noise ratio, but maximizing the effectiveness of the incident light that strikes the SAM samples would be another advantage in minimizing the background noise effects. According to Greenler one could maximize the effect of the light on the surface by directing the light at angles of  $4^\circ$  or  $5^\circ$  [4]. This recommendation implies that at very small angles —light almost traveling parallel to the surface sample— the path length of the light will increase and as a consequence the absorption of light by the molecules will increase. This latter approach makes even more sense if we imagine the surface area in question approaching infinity. Since the average area of the SAMs samples is at the most only  $1\text{cm}^2$  —with a dosing diameter surface of 8 mm— directing the light at very small angles on the surface is not practical. Celio and White in their experiments choose an angle of  $8^\circ$  to analyze a 13mm diameter surface [2]. Our particular SAMs may just have a fraction of the total area covered with peroxy radicals so we want to maximize the effectiveness of the incident light by choosing an optimum angle.

The optimum incident angle in this case would be  $15^\circ$ . This is from the fact that the electric vector of the incident light is predominantly responsible for the outcome of the signal-to-noise ratio.

### 2.2.3 Mirrors

It is well established that not all the light is transmitted from the surface of the sample to the detector. It happens that in a similar way the light leaving the IR source spreads out from the circular opening of the detector to become elliptical upon hitting the

surface of the sample, so does the light reflected from the surface when it arrives at the detector element (1mm x 1mm). The use of mirrors to correct this elongation/contraction phenomenon becomes necessary. In our system we can use an off-axis paraboloidal mirror with a focal length of 250 mm and another off-axis mirror of focal length of 39 mm. The optimum magnifying ratio obtained is 6.4:1 and it compares well to those obtained by Celio and White 7.2:1 for incident angles of  $8^\circ$  [2].

#### 2.2.4 Lenses

The lens in our FTIR apparatus is located in the small detector box (Figure 2.3). Here the lens receives the incoming light reflected off the SAM sample and redirects it to the detector. We do not need to use any other mirror for magnification or redirecting the light between the surface of the SAM and the detector because mirrors can contribute some degree of polarization. For the detector to receive the maximum input of the reflected light from the sample surface, the angle of the diverging beam of light from the surface to the lens must equal the angle of the converging beam of light of the input side. The off-axis paraboloidal mirror with a focal length of 250 mm will form an angle of  $8.7^\circ$  for an incident light beam with a diameter of 3.8 cm that is reflected off the mirror surface. This means that we need to use a lens of 3.8 cm in diameter, focal length of 3.37 cm, and  $F = 0.87$  to direct an image of 7 mm on the detector element (1mm x 1mm). To avoid any lens aberration we will install a coated anti-reflected Ge lens with a refractive index ( $n$ ) equal to 4. Mirrors made of ZnSe are another good option even though they contribute minor spherical aberration.

### 2.2.5 Polarization Flipper

The need to use a polarizer flipper is a direct consequence of employing the IRAS technique to analyze the peroxy radicals SAMs on the Au(111) surface. The principle behind the IRAS technique requires that the % transmittance of the molecules on the sample surface and the % transmittance of the clean surface be known to obtain a spectrum. This represents a difficulty, since SAMs are not reversibly adsorbed due to strong bonding with the surface. One way to solve the problem is by employing a polarizer flipper. The idea is to take advantage of the selection rules governing molecular vibration, which implies that any transitional dipole moment parallel to the surface (in this case Au(111)) will have net intensity of zero. In this way only the perpendicular transitional dipole moments will generate a signal. The polarizer flipper will allow us to obtain an IRAS spectrum by “flipping” in different sets of measurements the light beam - from the FTIR- between parallel and perpendicular orientations. The polarization flipper might contribute to additional background noise for long periods of scanning; therefore, equipping our FTIR with the polarization flipper should not be a problem, since obtaining a noise % 0.001 takes only 15 seconds (~ 35 scans).

## REFERENCES FOR CHAPTER II

1. *Scienta ESCA 300 Users' Manual*, Scienta, Uppsala, 1989
2. Celio, H; White, J. M. Private Communication (1999)
3. Stallard, B. R.; Espinoza, L. H.; Rowe, R. K.; Garcia, M. J.; Niemczyk, T. M., *J. Electrochem. Soc.* **1995**, 142, 2777.
4. Greenler, R. G., *J. Chem. Phys.* **1966**, 44, 310

## CHAPTER III

### SIMULTANEOUS OXIDATION AND REDUCTION OF ARSENIC BY ZERO-VALENT IRON NANOPARTICLES: UNDERSTANDING THE SIGNIFICANCE OF THE CORE-SHELL STRUCTURE

#### 3.1 Introduction

The principal forms of arsenic in natural waters are arsenate (As(V)) and arsenite (As(III)). Arsenate exists as oxyanions ( $\text{H}_2\text{AsO}_4^-$  or  $\text{HAsO}_4^{2-}$ ) in a pH range of 2 to 12, while arsenite remains as neutral undissociated species ( $\text{H}_3\text{AsO}_3$ ) below a pH of 9.2 [1, 2]. As(III) oxidation to As(V) by dissolved oxygen alone is kinetically slow [3]. Traditional remediation technologies rely largely on adsorption for removing arsenic in water using materials such as iron oxides, activated alumina, granular activated carbon, and silica with various degrees of success [5, 6]. Current studies suggest that nanoscale zero-valent iron (nZVI), a highly reactive engineered nanomaterial extensively evaluated for groundwater remediation and hazardous waste treatment, is effective for arsenic removal in water, but the reaction mechanisms of arsenic on nZVI are not well understood. Because of nZVI's strong reducing capabilities towards chlorinated hydrocarbons and numerous inorganic contaminants, it is expected that both arsenic (V) and arsenic (III) are amenable to reduction by nZVI. Prior publications indicate, however, the transformation of As(V) to As(III) is kinetically slow, and no clear evidence for the formation of elemental arsenic (As(0)) has been published so far [6,7, 8]. On the other hand, several recent studies suggest that, instead of reduction, oxidation of arsenic (III) is

the prevalent reaction under oxic conditions through peroxide or radicals generated by Fenton reactions [4, 9].

The objective of this work was to examine surface reactions of arsenate and arsenite with nZVI by using High-Resolution X-ray Photoelectron Spectroscopy (HR-XPS), which can provide valuable information about the valence states and abundance of various arsenic species on nanoparticle surfaces. The results are interpreted in light of the fundamental structure of nZVI, and the implications of these findings on arsenic treatment and remediation are discussed.

## **3.2 Materials and Experimental Methods**

Iron nanoparticles (nZVI) used in this study were prepared from sodium borohydride reduction of ferric iron as reported previously [10, 11]. The nanoparticles have a mean diameter of 60 nm and a BET-measured surface area of 30 m<sup>2</sup>/g [10].

### **3.2.1 As Reactions**

As(III) or As(V) solutions were prepared from NaAsO<sub>2</sub> and NaHAsO<sub>4</sub> • 7H<sub>2</sub>O (both from Fluka), respectively, and the solutions were purged with nitrogen (high purity, >99.9% ) for 30 minutes immediately before nZVI introduction. Experiments were carried out in closed, 120-ml serum bottles in which the solution volume was 100 ml. After loading nZVI to give a concentration of 5 g/L, the bottles were closed and the caps sealed with a Teflon liner to prevent air leakage and placed on a mechanical shaker at 25 °C. After 24 hours, the reacted nZVI were harvested by vacuum filtration, dried and stored in a N<sub>2</sub>-filled box.

### 3.2.2 XPS Analysis

Dried samples of nZVI, after reaction with As(III) or As(V) solutions, were characterized using High Resolution X-ray Photoelectron Spectroscopy (HR-XPS) performed on a Scienta ESCA 300 spectrometer. This instrument has a 8-kW rotating anode source and 7-crystal monochromator for providing monochromated Al K $\alpha$  X-rays ( $h\nu = 1486.7$  eV), and enhanced signal detection utilizing a 300-mm radius hemispherical analyzer and position-sensitive detector, which provides high energy resolution at greatly enhanced signal-to-noise ratios. The nZVI samples were placed in the HR-XPS analysis chamber ( $5 \times 10^{-9}$  Torr) where spectra for As3d, O1s, Fe2p and C1s regions were taken. Spectra were obtained using a takeoff angle of  $90^\circ$  with respect to the surface plane of the samples. The hemispherical analyzer pass energy for this characterization was set at 150 eV, giving an optimized resolution of the analyzer of 0.1 eV. Each As3d and O1s spectrum was calibrated against a value of 284.6 eV binding energy (BE) for adventitious carbon detected in the C1s region. Curve-fitting for both regions was accomplished by using CASA XPS MFC Application software, version 2.3.12.8. In the curve-fitting procedure, a Shirley background was selected to account for inelastic scattering, and all peaks were described using a Gaussian/Lorentzian ratio of 70/30. The full-width-at-half-maximum (FWHM) of each component peak was set to 1.2 eV for As3d spectra and 1.3 eV for O1s spectra. The As3d<sub>5/2</sub> and As3d<sub>3/2</sub> components of the As3d spin orbit-split doublet peak were fixed at a constant intensity ratio of 3:2 and at a fixed separation of 0.7 eV.



### 3.3 Results and Discussion

Figure 3.1 displays XPS spectra of the As3d region of nZVI before (a) and after reactions with As(V) (b) and As(III) (c) species, respectively. The XPS peak positions were assigned by comparison to As3d<sub>5/2</sub> binding energies reported in the literature [12]. No arsenic was detected on pristine nZVI, but As peaks were clearly detected on reacted nZVI. The XPS spectra reveal the presence of multiple arsenic valence states, *viz.*, As(V), As(III), and As(0) on the nZVI surfaces. Curve fitting of the As peaks involved six curves, since the As3d peak for each chemical state has two unresolved components due to spin-orbit splitting corresponding to the As3d<sub>3/2</sub> (at higher BE) and As3d<sub>5/2</sub> (at lower BE) peaks separated by 0.7 eV (held constant herein). The relative abundance of each chemical species can be quantified from the respective peak areas. In addition, information on the total As surface composition obtained from XPS is summarized in Table 3.1, and these data are used below to infer the relative extent of different reactions that occurred on nZVI surfaces.

#### 3.3.1 Reactions with As(V)

When nZVI (5 g/L) was added to 100-mg/L As(V) solution, significant amounts of As(III) and As(0) were detected on the nZVI surface in 24 hours (Figure 3.1b), establishing As(V) reduction to As(III) and As(0). The amounts indicated in Figure 3.1 are the proportions of the respective arsenic species as percentages of the total arsenic detected. It should be noted that each of these spectra were not affected by increasing the X-ray irradiation time by a factor of six under the instrument conditions used in this

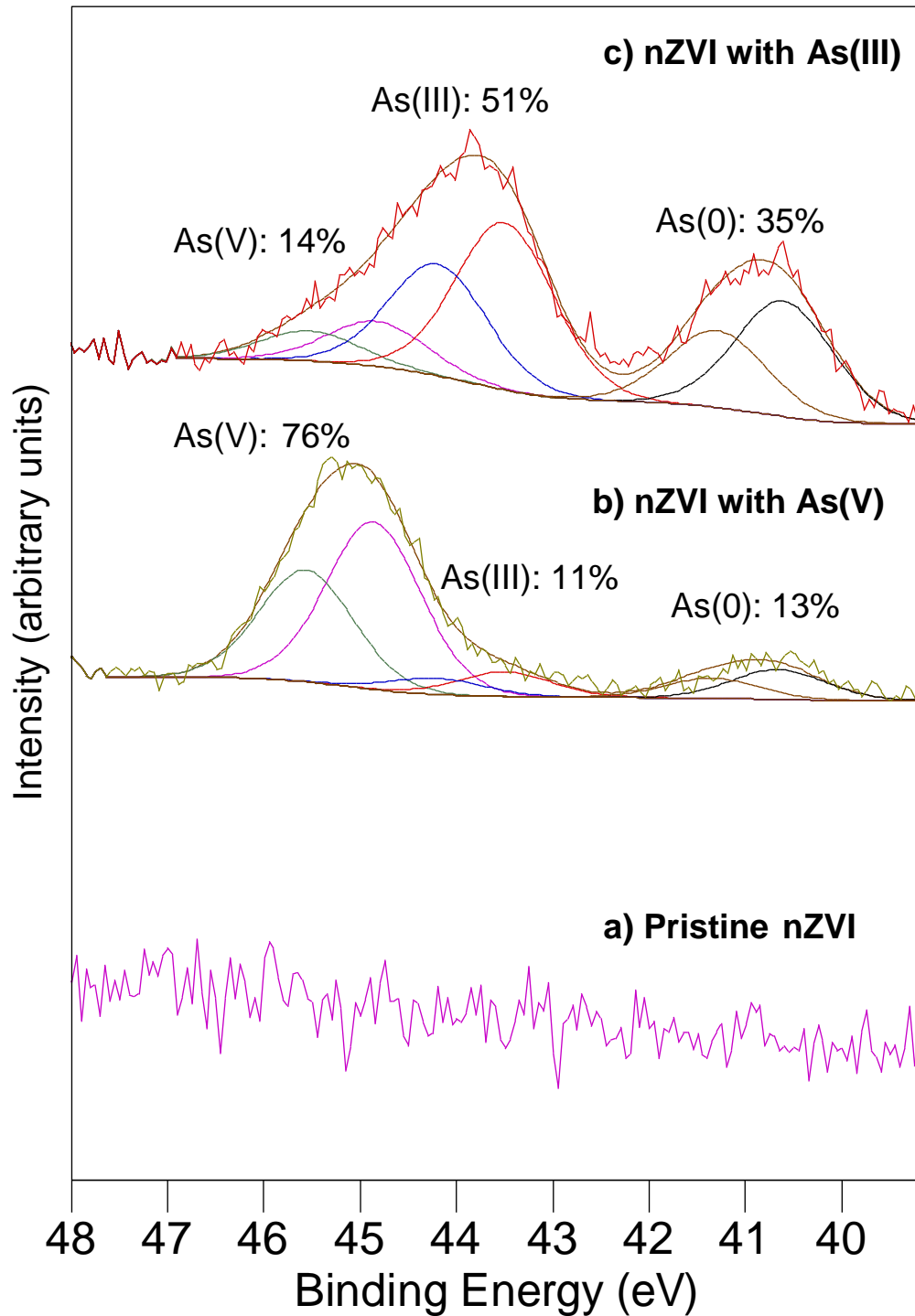


Figure 3.1 As<sub>3d</sub> HR-XPS spectra of (a) fresh nZVI and (b) nZVI reacted with 100mg/L As(V), and (c) nZVI reacted with 100mg/L As(III). The nZVI loading in (b) and (c) was 5g/L. The proportions of the respective species as percentages of the total As detected are annotated on the spectra. The intensity scale varies for each curve.

Table 3.1 Surface composition of samples analyzed by XPS\*

	As(III) (at. %)	As(0) (at. %)	As(V) (at. %)	Total As (at. %)	Total Fe (at. %)	Total O (at. %)
Fig1c nZVI w/ As(III)	0.8	0.5	0.3	1.6	19.7	78.7
Fig 1b nZVI w/ As(V)	0.2	0.4	2.3	3.0	18.4	78.6
Fig 1a pristine nZVI	0	0	0	0	13.3	86.7
Fig3a 50 mg/L As(III)	0.4	0.7	0.2	1.4	21.2	77.3
Fig 3b 100 mg/L As(III)	0.8	0.5	0.3	1.6	19.7	78.7
Fig 3c 500 mg/L As(III)	3.2	0	1.6	4.8	16.0	79.3
Fig 3d 1000 mg/L As(III)	4.5	0	1.5	5.9	15.0	78.0

\*Surface compositions reported as atomic percent, as calculated from XPS spectra using the measured peak areas and appropriate relative sensitivity factors. The calculations assume a homogeneous distribution of elements in the sample.

study, *i.e.*, XPS analysis had no observable effect on the arsenic valence state detected. We have also analyzed nZVI reacted with arsenic for up to 15 days, and the results indicate no significant change in arsenic distributions compared to samples reacted for 24 hours under the same conditions. While earlier studies reported the reduction of arsenate to arsenite species by iron fillings or nanoscale ZVI with considerably slower kinetics (e.g., >30 days before As(III) was detected) [2, 7], the formation of As(0) has only been suggested, but not substantiated, and the predominant mechanism for As(V) uptake is generally thought to be surface sorption and precipitation [7, 13]. Results presented in Figure 3.1 clearly show that nZVI is capable of reducing As(V) with reasonably fast kinetics and reduction to elemental arsenic is also a feasible mechanistic step. As will be discussed later herein, the variances in environmental conditions, in particular arsenic concentration and solution pH, and the properties of iron materials play crucial roles in determining the final arsenic speciation.

### 3.3.2 Reactions with As(III)

When nZVI was added to an arsenite [As(III)] solution (Figure 3.1c), 51 % of the surface-bound arsenic remained as As(III). Meanwhile, 14% and 35% of the total arsenic emerged as As(V) and As(0), respectively, indicating that both As(III) oxidation and reduction had occurred to significant extents. While As(III) oxidation by ZVI was noticed in prior studies, [1, 18], the concomitant observation of oxidation and reduction of arsenic (III) has not been reported before. This behavior implies that the nanoparticles used here have a more complex character than being a monofunctional reductant as widely acknowledged.

To understand the properties of nZVI, advanced TEM techniques were used to analyze the material constituents present in individual nZVI particles. Bright Field-TEM imaging showed a composite layered structure comprised of a dense metallic center enclosed by a thin layer of iron-oxide material (Figure 3.2a). Phase-contrast TEM imaging did not reveal periodic lattice-fringes in the oxide layer, which suggests a disordered oxide structure (Figure 3.2b). The oxide outer-shell appears to vary from 10-20 nm in thickness and has a stoichiometric composition of FeOOH as determined previously from Fe2p and O1s XPS spectra [14]. The oxide layer is thought to form instantaneously upon nZVI synthesis to passivate the highly reactive Fe<sup>0</sup> core and it may be practically viewed as an inherent part of the nanoparticle [15]. The extremely thin dimension and disordered nature of the oxide layer support earlier notions that the oxide phase is able to allow electron passage via tunneling effects or defect sites [11, 15], thereby conserving the reducing characteristics of Fe<sup>0</sup> and accounting for As(III) reduction. On the other hand, iron oxides have been extensively studied to possess strong adsorptive ability for both As(III) and As(V), and certain iron oxides formed from Fe<sup>0</sup> corrosion are able to cause As(III) oxidation to As(V) [2, 16]. In our studies, the nanoparticles are comprised of an Fe<sup>0</sup> core and iron oxide at the interface between Fe<sup>0</sup> and aqueous solution. The two phases are present in a nanoscale core-shell configuration that allows each component to exert its distinctive reactivity without significant kinetic constraints. The composite particles therefore possess dual properties of the two components and this leads to unconventional chemical behavior such as the concurrent oxidation, reduction and sorption of As(III) illustrated in Figure 3.1c.

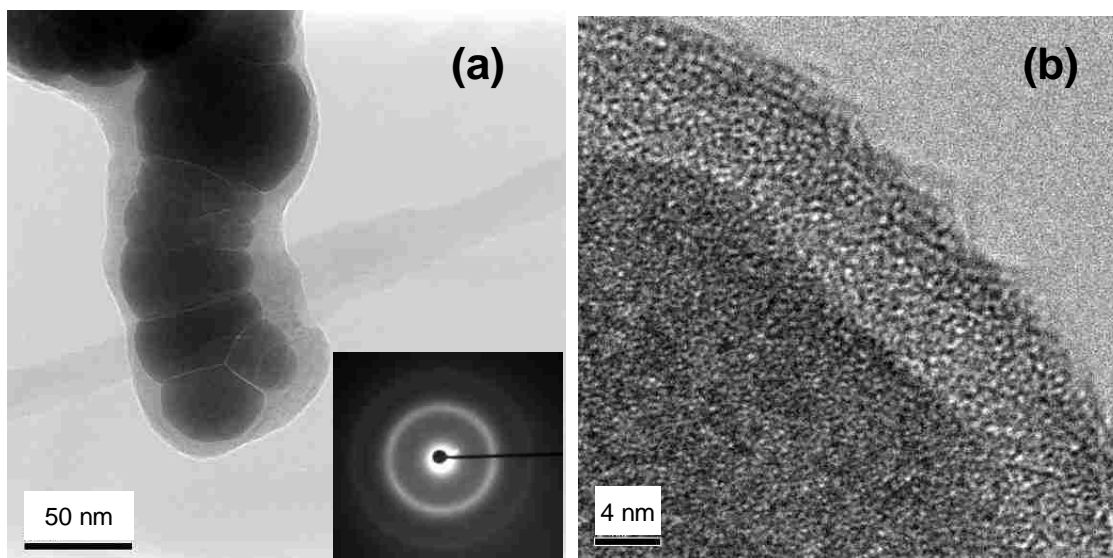


Figure 3.2 (a) Bright field-TEM micrograph of nZVI nanoparticles showing a core-shell structure comprised of a dense metallic center and a thin, continuous oxide skin. The inset shows the electron diffraction pattern of the metallic core, which suggests a polycrystalline *bcc* structure. (b) HR-TEM micrograph of a single nZVI nanoparticle. The lack of long-range periodic lattice fringes in the oxide layer suggests that it is amorphous in character.

### 3.3.3 Effect of As(III) concentrations

The effect of arsenite concentration on the product speciation has not been examined before. Figure 3.3 presents results following reaction of nZVI with arsenite at different initial As(III) concentrations. The initial As(III) concentration in the solution was in the range of 50-1,000 mg/L. Clearly, the relative amount of As(0) formed is the greatest at the lowest initial concentration of As(III) (50mg/L), with approximately one-half of the total arsenic present as As(0). The proportion decreased to 17% when the initial As (III) concentration was increased to 100 mg/L, and no As(0) was detected when As(III) concentration was increased to 500 and 1,000 mg/L.

The solution  $E_h$  and pH conditions corresponding to different As(III) concentrations are presented in Table 3.2. The equilibrium pH changed from (pH 8.5) to alkaline (pH11) as the As(III) concentration increased from 50 to 1,000 mg/L (Figure 3.4). The equilibrium pH was largely influenced by the starting pH, which showed an increasing trend as the As(III) initial concentration increased due to arsenite hydrolysis and the release of hydroxyl ions ( $\text{AsO}_2^- + \text{H}_2\text{O} \rightarrow \text{H}_3\text{AsO}_3/\text{H}_2\text{AsO}_2^- + \text{OH}^-$ ). The alkaline condition associated with high Ar(III) concentrations promotes ferric ion precipitation. This point is corroborated by the O1s XPS spectra of the reacted samples (Figure 3.5), which show a pronounced increase in the OH<sup>-</sup> peak size with increased initial arsenic loading. Iron oxide precipitates are also evident in SEM images (Figure 3.6), where the sample after reaction with 1000 mg/L As(III) exhibited extensive platelet formation resembling typical solid precipitates from iron corrosion (Figure 3.6c). In contrast, the oxide growth was less predominant in the 100 mg/L sample (Figure 3.6b). A further piece of evidence in support of oxide build-up comes from solution  $E_h$ . The  $E_h$

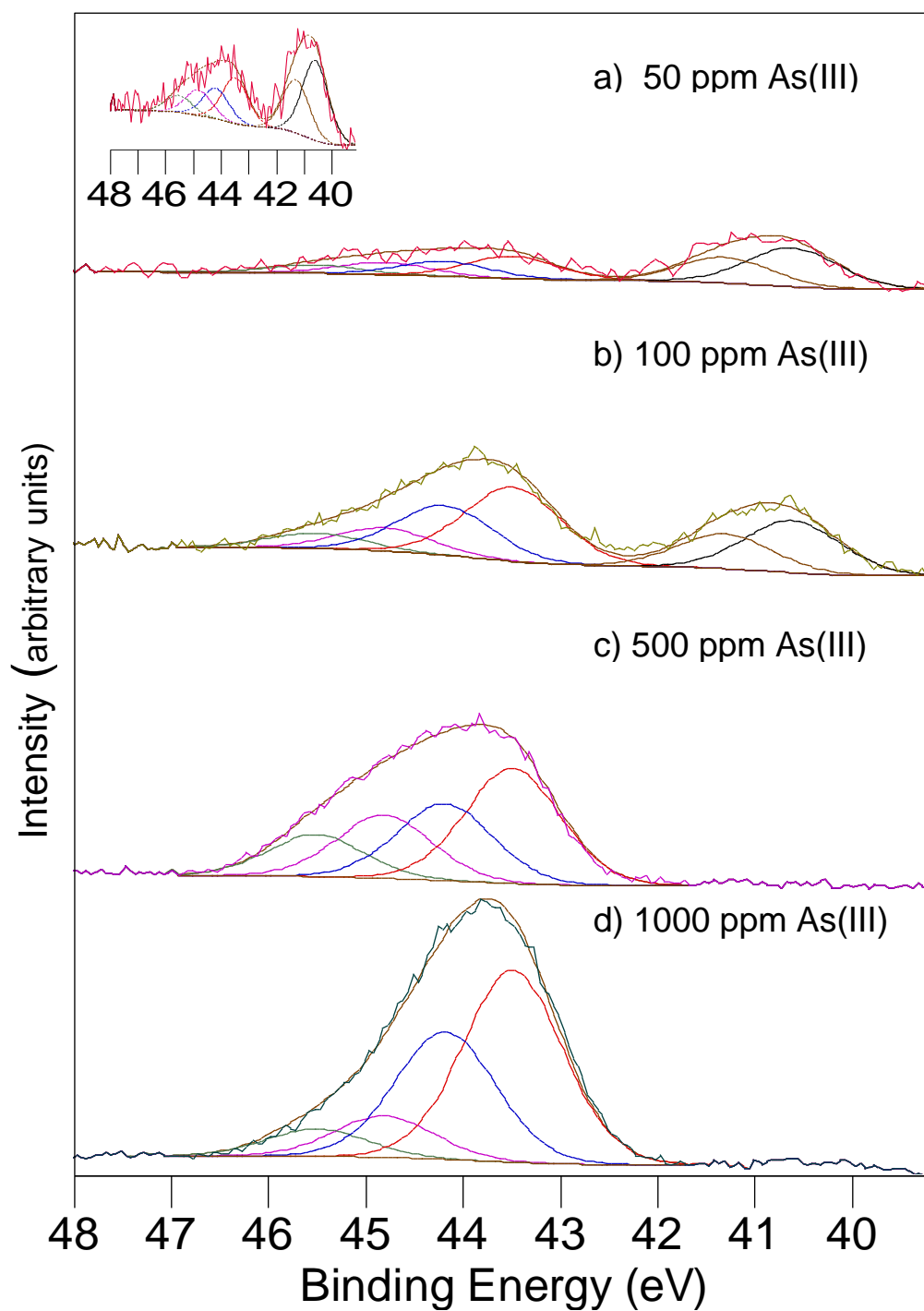


Figure 3.3 As<sub>3d</sub> HR-XPS spectra from nZVI particles exposed to different initial concentrations of As(III). The nZVI loading was 5g/L in all cases. The inset of (a) is a vertically expanded view of spectrum (a).



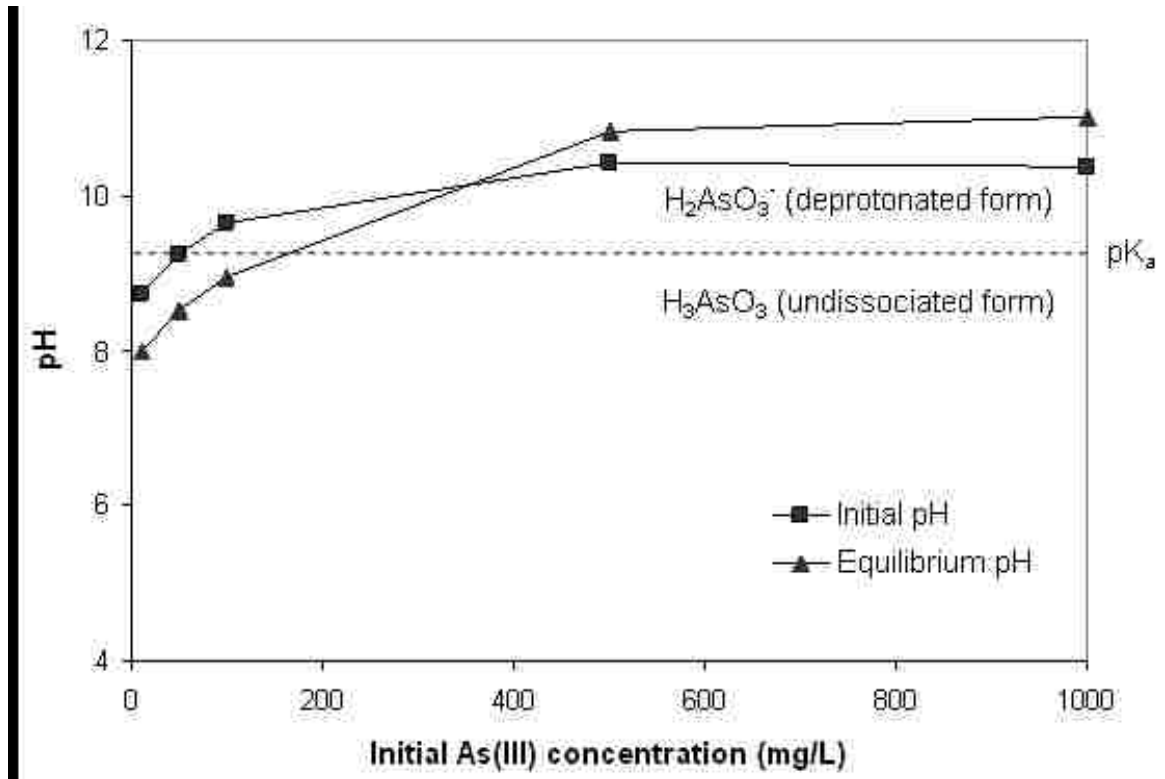


Figure 3.4 Solution pH for various initial As(III) concentrations. nZVI loading was fixed at 5 g/L. Initial pH was measured before nZVI loading. Equilibrium pH was obtained after a reaction time of 24 hours. The dashed line corresponds to the  $pK_a$  value of  $H_3AsO_3$ , which dissociates to  $H_2AsO_3^-$  at  $pH > pK_a$ .

Table 3.2 Solution pH and  $E_h$  before and after reactions\*

	Reaction conditions	pH (t=0 hr)	pH (t=24 hr)	$E_h$ , mV (t=24 hr)
Fig. 1b	As(V) 100 mg/L	8.2	9.3	115
Fig. 1c	As(III) 100 mg/L,	10.0	8.9	-49
Fig. 3a	As(III) 50 mg/L	9.2	8.5	-198
Fig. 3b	As(III) 100 mg/L	10.0	8.9	-84
Fig. 3c	As(III) 500 mg/L	10.4	10.8	152
Fig. 3d	As(III) 1000 mg/L	10.4	11.0	158

\* The amount of nZVI was 5g/L and the reaction time was 24 hr for each sample.

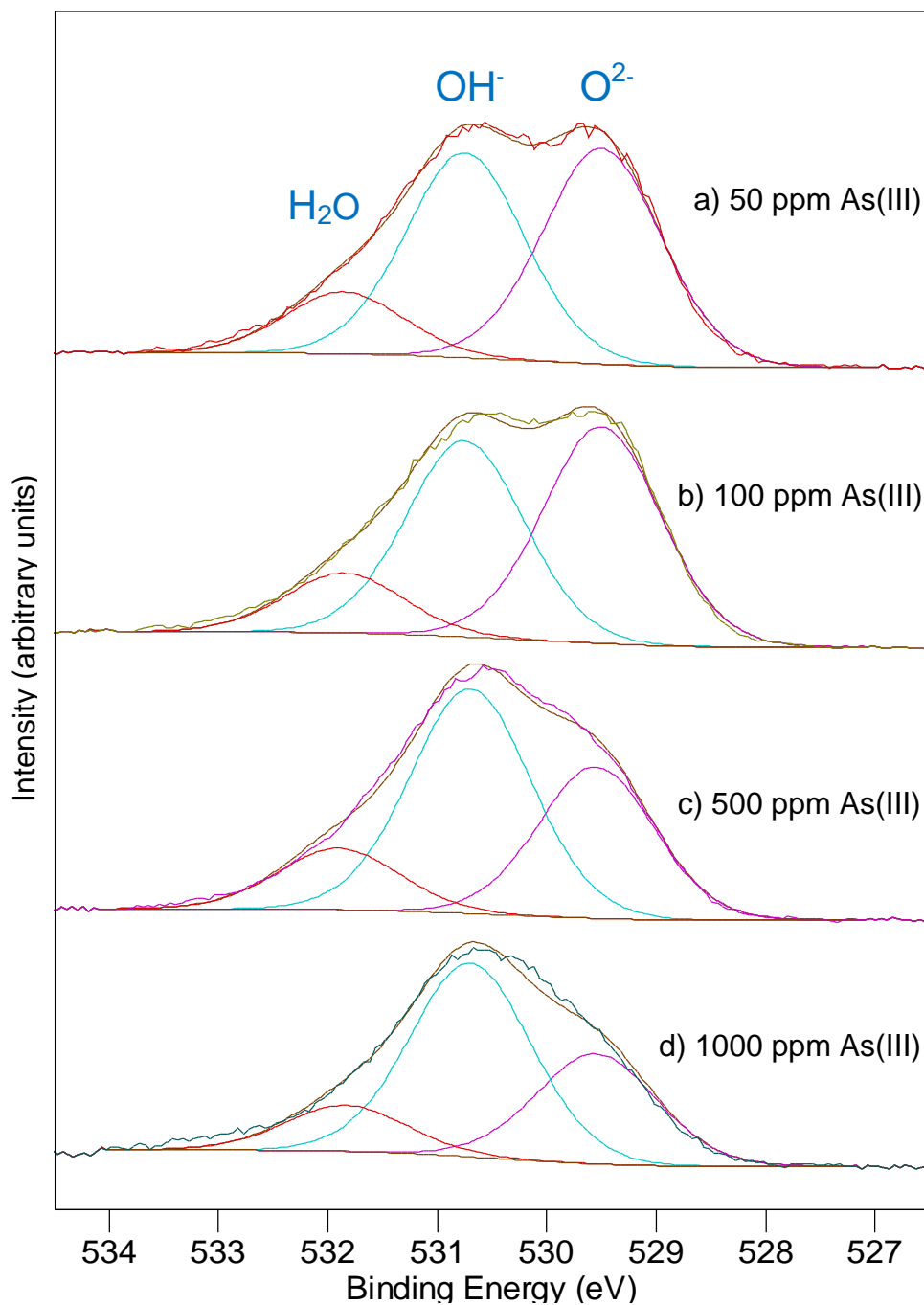


Figure 3.5 O1s HR-XPS spectra obtained after different initial concentrations of As(III) (nZVI loading was fixed at 5 g/L). The prominent increase in OH<sup>-</sup> at the two highest As(III) concentrations indicates substantial iron hydroxide formation at the solid surface. The different forms of oxygen are indicated in the top spectrum: H<sub>2</sub>O at 531.8 eV, OH<sup>-</sup> at 530.7 eV, and O<sup>2-</sup> at 529.5 eV.

potentials registered a sharp increase with As(III) concentration at 500 and 1000 mg/L (Table 3.2), suggesting the prevalence of iron oxidation products observed in HR-XPS and SEM at those high concentrations forms a barrier layer on top of metallic iron and diminishes  $\text{Fe}^0$  reducing capability. Taken together, As(III) concentration exerts a pronounced effect on As(III) reduction by controlling solution chemistry and influencing the nZVI surface conditions. Formation of As(0) was more evident at lower concentrations and it was absent at above 100 mg/L due to substantial iron oxidation and precipitate formation. Although the concentration range evaluated here is higher than arsenic occurrence in natural waters (typical range 1-5000  $\mu\text{g/L}$ ), the trend revealed in Figure 3.3 strongly implies that reduction of arsenite at trace levels such as in natural waters is likely to occur in the presence of nZVI. As(0) not being observed in previous studies may be attributed to instrumental limitations and the specific reaction conditions used. In those studies, relatively high As(III) concentrations were used since conventional XPS analysis requires a significant amount of arsenic deposited on the particle surfaces to be detected. Under those conditions, As(0) formation is not favored for the reasons just mentioned above, and surface saturation with adsorbed arsenic species may attenuate the already weak As(0) signal. In the present HR-XPS study, we used a Scienta ESCA 300 instrument, which has an intense rotating anode X-ray source and enhanced signal detection utilizing a 300-mm radius hemispherical analyzer and position-sensitive detector, thereby greatly lowering the arsenic detection limit and improving the energy resolution. This enables us to study nZVI reactions with arsenic at lower initial concentrations, which are conditions more relevant to the natural systems.

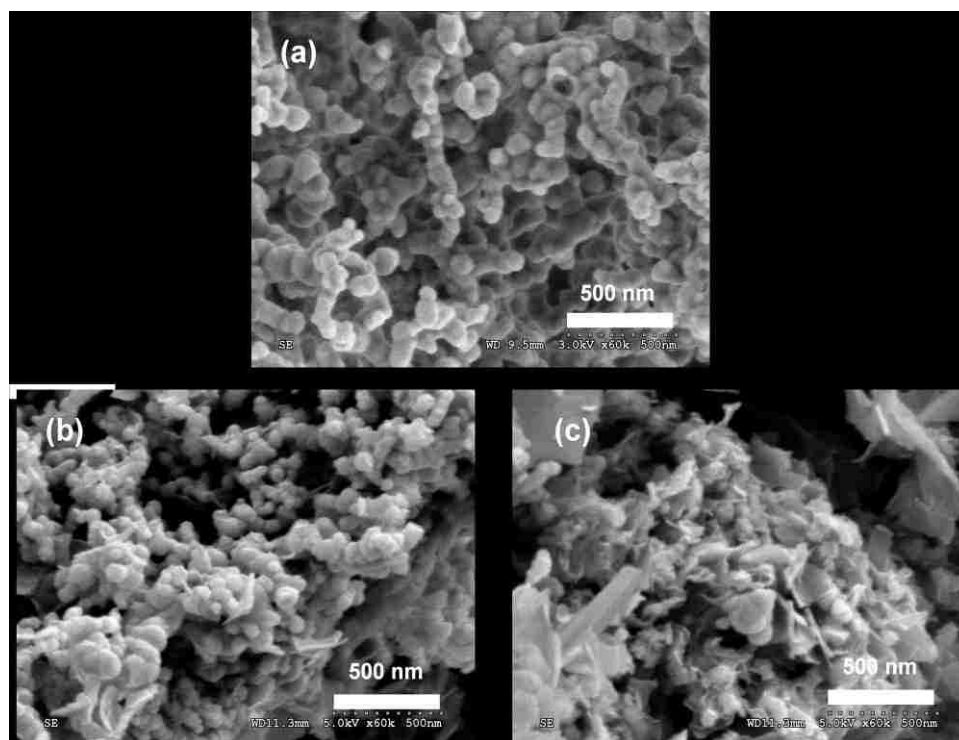


Figure 3.6 SEM images of a) a fresh nZVI sample, b) 5g/L nZVI reacted with 100 mg/L As(III) for 24 hr, and c) 5g/L nZVI reacted with 1000 mg/L As(III) for 24 hr.

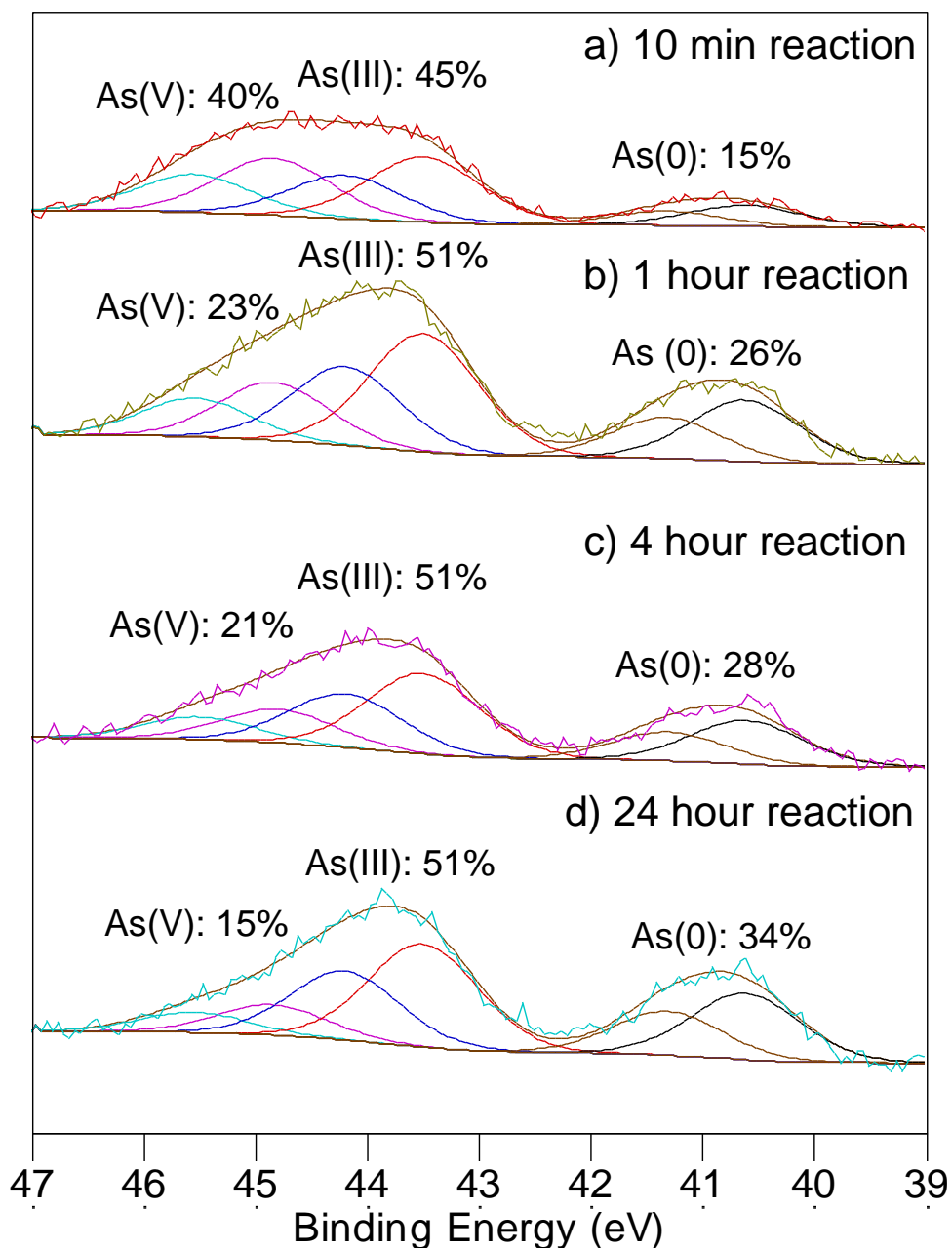


Figure 3.7 As<sub>3d</sub> HR-XPS spectra from nZVI particles reacted with 100 mg/L As(III) for different reaction times. The nZVI loading was 5g/L in all cases. The proportions of the respective species as percentages of the total As detected are annotated on the spectra.

Compared to reduction of As(III) to As(0), oxidation of As(III) to As(V) is less sensitive to the initial As(III) concentration (Figure 3.3). In all cases, As(V) exists as a minor species on the nanoparticle compared to the other two valence states. As(III) oxidation by nZVI has been reported in previous studies, although the exact mechanism remains uncertain. It is purported that there exists more than one oxidant, including peroxide or radical species generated from  $\text{Fe}^0$  corrosion, hydroxide species, and iron oxides [1, 16-18]. Peroxide or oxygen-containing radical generation requires dissolved  $\text{O}_2$  in acidic medium [17,18] and they are not likely to be involved considering our reaction conditions. As(III) oxidation in aqueous phase by hydroxyl ions is plausible [16], but the resultant As(V) species in the solution phase is unlikely to re-attach to the nZVI surface due to surface charge repulsion between As(V) and the oxide layer at neutral to alkaline pH [19]. It is more likely that As(III) was oxidized by iron oxide, which proceeded via formation of iron oxide-As(III) surface complexes [1]. The lack of a distinct trend for As(III) oxidation within the concentration range studied is probably a result of several interacting effects, since the affinity of As(III) for iron oxides, the amount of iron oxides available as adsorptive sites, and the oxidation potential of iron oxides are intricately affected by pH.

The evidence for the simultaneous occurrence of oxidation, reduction and adsorption of As(III) on nZVI surface suggest that the two components of nZVI are able to bring about different reactions in parallel, which is an interesting property that has not been noted before. A time-dependent study of arsenic speciation on nZVI surface (Figure 3.7) provides a clue to the relative kinetics of the respective reactions. As shown in Figure 3.7, As(0) accumulation is relatively slow in comparison to As(III) adsorption and

oxidation. It may also be implied from the figure that the products formed initially, e.g. As(V), may be reduced back to As(III) and then to As(0), hence, there is a dynamic change in arsenic speciation at the nZVI surface on top of continuous arsenic sequestration from the aqueous phase. Additional experiments are needed to elucidate the individual reaction rates and the interrelations among these processes.

### **3.4 Conclusion**

Simultaneous oxidation and reduction of As(III) and the reduction of As(V) to As(III) and As(0) on nZVI surfaces have been observed. The elusive As(0) species suggested in previous studies was clearly detected. The reactions can be reasonably explained based on the core-shell structure of nZVI, in which the oxide outer-layer and metallic core bestow distinctive mechanisms for arsenic removal. The results shown here may help to understand the reaction mechanisms and the stability of arsenic on ZVI surfaces and lead to better design of arsenic sequestration technologies. In particular, in view of the conventional adsorptive methods, which are critically affected by arsenic speciation, concentration and pH, the multi-faceted functionality of nZVI exhibited here may offer a more robust and effective method for arsenic removal.



### REFERENCES FOR CHAPTER III

1. Manning, B. A.; Hunt, M. L.; Amrhein, C.; Yarmoff, J. A., *Environ. Sci. Technol.* **2002**, *36*, 5455.
2. Kanel, S. R.; Greneche, J. M.; Choi, H., *Environ. Sci. Technol.* **2006**, *40*, 2045.
3. Scott, M. J.; Morgan, J. J., *Environ. Sci. Technol.* **1995**, *29*, 1898.
4. Hug, S. J.; Leupin, O., *Environ. Sci. Technol.* **2003**, *37*, 2734.
5. Goldberg, S.; Johnston, C. T. *J. Colloid Interf. Sci.* **2001**, *234*, 204.
6. Mohan, D.; Pitman, C. U., *J. Hazard. Mater.* **2007**, *142*, 1.
7. Su, C. M.; Puls, R. W., *Environ. Sci. Technol.* **2001**, *35*, 1487.
8. Kanel, S. R.; Manning, B.; Charlet, L.; Choi, H., *Environ. Sci. Technol.* **2005**, *39*, 1291.
9. Leupin, O. X.; Hug, S. J., *Water Res.* **2005**, *39*, 1729.
10. Sun, Y. P.; Li, X. Q.; Cao, J. S.; Zhang, W. X.; Wang, H. P., *Adv. Colloid Interfac.* **2006**, *120*, 47.
11. Li, X. Q.; Zhang, W. X., *Langmuir* **2006**, *22*, 4638.
12. Moulder, J. F.; Stickle, W. F.; Sobol, P.E.; Bomben, K. D., *Handbook of X-ray Photoelectron Spectroscopy*; Perkin-Elmer Corporation, Eden Prairie, MN, 1992.
13. Lackovic, J. A.; Nikolaidis, N. P.; Dobbs, G. M., *Environ. Eng. Sci.* **2000**, *17*, 29.
14. Martin, J. E.; Herzing, A. A.; Yan, W. L.; Li, X. Q.; Koel, B. E.; Kiely, C. J.; Zhang, W. X., *Langmuir* **2008**, *24*, 4329.
15. Nurmi, J. T.; Tratnyek, P. G.; Sarathy, V.; Baer, D. R.; Amonette, J. E.; Pecher, K.; Wang, C. M.; Linehan, J. C.; Matson, D. W.; Penn, R. L.; Driessen, M. D. *Environ. Sci. Technol.*, 2005, *39*, 1221.
16. Manning, B. A.; Goldberg, S., *Environ. Sci. Technol.* **1997**, *31*, 2005.

17. Joo, S. H.; Feitz, A. J.; Waite, T. D., *Environ. Sci. Technol.* **2004**, 38, 2242.
18. Katsoyiannis, I. A.; Ruettimann, T.; Hug, S. J., *Environ Sci. Technol.* **2008**, 42, 7424.
19. Manning B. A.; Fendorf, S. E.; Goldberg, S., *Environ Sci. Technol.* **1998**, 32, 2383.

## CHAPTER IV

### ARSENIC ENCAPSULATION IN IRON NANOPARTICLES: EVIDENCE OF INTRAPARTICLE REACTIONS

#### 4.1 Introduction

The occurrence of arsenic in groundwater is a global health concern [1,2] and this has stimulated extensive research to develop technologies for arsenic removal from drinking water sources. Although zero-valent iron (ZVI) has been shown to be effective for both arsenate (As(V)) and arsenite (As(III)) sequestration, and it is currently used in many arsenic treatment installations [3-9], there is no clear consensus on the reactions between ZVI and arsenic, especially on the nature of solid-phase arsenic redox transformations. On the basis of the well-documented surface interactions between arsenic and iron oxides [10-13], it is conceived that arsenic is retained by formation of complexes with an oxide passivation layer present at the surface of ZVI [3-5]. Additionally, precipitation of arsenic with ferrous or ferric ions from Fe(0) corrosion has also been proposed [6,7]. While these processes may account for the immobilization of arsenic from an aqueous phase, reactions within ZVI and the resultant products are not well understood.

Herein we report the investigations of reactions between nanoscale zero-valent iron (nZVI) and arsenite (As(III)) using high-resolution X-ray photoelectron spectroscopy (HR-XPS) multiline analysis and demonstrate for the first time stratified distributions of multiple arsenic valence states within the iron nanoparticles. These results

reveal that As(III) oxidation and reduction can occur in parallel in separate regions of the nanoparticles. This multi-domain intraparticle reaction model draws attention to the importance of iron-arsenic solid-phase redox chemistry in arsenic sequestration processes and sheds new light on the potential of nZVI as an arsenic treatment agent.

High efficacy of nZVI for As(III) removal from an aqueous phase over a wide range of concentrations (ppb to ppm levels) has been reported [3,5-7]. This report focuses on the solid-phase chemistry of nZVI in reactions with As(III) solutions. nZVI material was prepared by using the borohydride reduction method described previously [14,15]. Scanning electron microscopy (SEM) characterization showed nanoparticles varying in size from 50 to 100 nm, and high-resolution transmission electron microscopy (HR-TEM) analysis revealed individual particles comprised of a core of nanocrystalline *bcc* Fe(0) enclosed by a continuous, amorphous oxide layer (Figure 4.1). The stoichiometric composition of the oxide layer was determined to be FeOOH in previous XPS work [14]. In this work, we compare results using nZVI with those from two common iron oxides, Fe<sub>2</sub>O<sub>3</sub> and Fe<sub>3</sub>O<sub>4</sub>, to demonstrate the distinct reactivity possessed by nZVI. X-ray diffraction (XRD) revealed these iron oxides to be predominantly hematite and magnetite, respectively, and their specific surface areas were comparable to that of nZVI (Table 4.1).

## 4.2 Experimental methods

### 4.2.1 Preparation of iron materials

Iron nanoparticles (nZVI) were prepared from reduction of ferric chloride by sodium borohydride as described in previous studies [12,16]. As-synthesized nZVI was

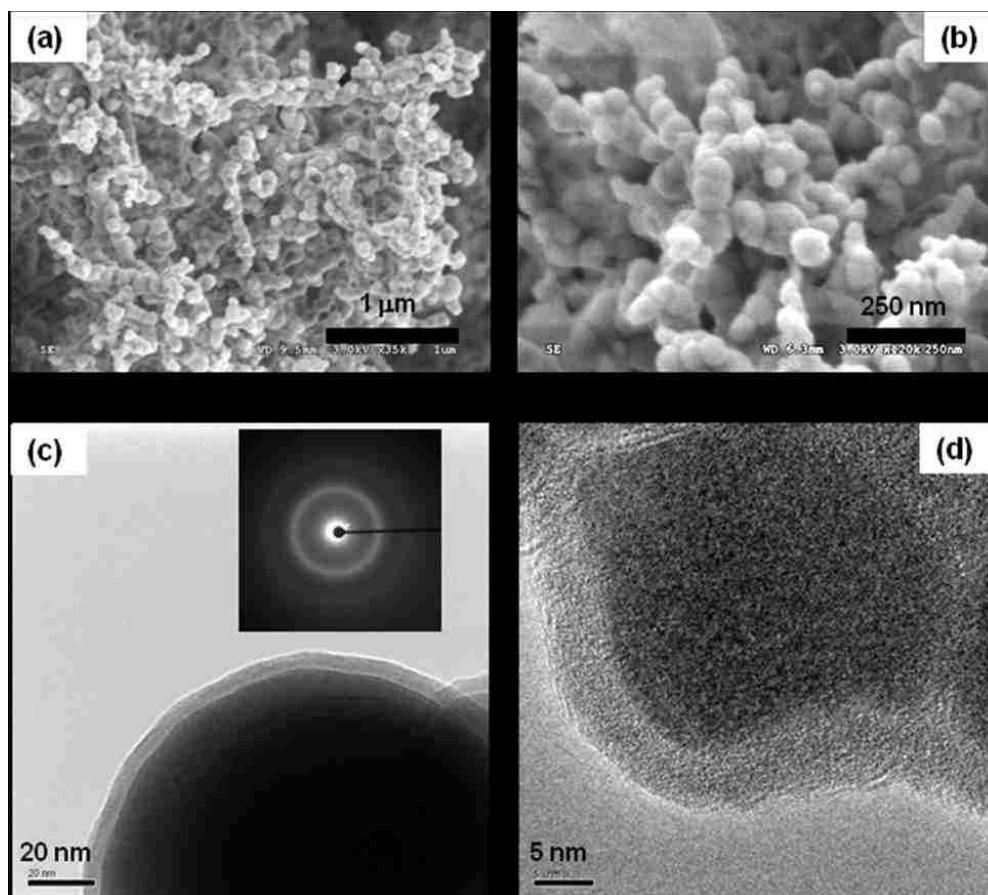


Figure 4.1 (a)-(b) Field-emission SEM micrographs of freshly made nZVI nanoparticles showing the particles are in the size range of 50 to 100 nm. (c) Bright field TEM micrograph of an individual nZVI particle reveals a dense core encapsulated by a thin continuous layer of iron oxide. The inset shows electron diffraction from the interior core region, in which the diffuse ring pattern is characteristic of polycrystalline *bcc* Fe(0). (d) Phase contrast TEM image of a particle. The lack of long-range periodic lattice fringes in the oxide region underlies its amorphous nature.

Table 4.1 Characteristics of various iron-based materials used in the study

<b>Iron material</b>	<b>Source</b>	<b>BET surface area m<sup>2</sup>/g</b>	<b>Crystalline phase</b>
Fe <sub>2</sub> O <sub>3</sub>	Fisher	11	Hematite
Fe <sub>3</sub> O <sub>4</sub>	Fisher	8.0	Magnetite
nZVI	Lab synthesized	30	Core: <i>bcc</i> iron <sup>a</sup> Shell: amorphous FeOOH <sup>b</sup>

<sup>a</sup>See electron diffraction pattern shown in Figure 4.1.

<sup>b</sup>Assignment based on stoichiometry of Fe, O and OH measured in prior XPS characterization [12].

stored in 95% ethanol solution in a sealed PTFE container at 4°C prior to use. Prior characterization work showed that the nanoparticles have a median diameter of 60 nm and a BET surface area of 30 m<sup>2</sup>/g [13]. Two iron oxide powders, Fe<sub>3</sub>O<sub>4</sub> and Fe<sub>2</sub>O<sub>3</sub> (both from Fisher Chemicals), were used as received.

#### 4.2.2 Arsenic batch experiments

As(III) solutions were prepared from NaAsO<sub>2</sub>(Fluka). The solutions were deoxygenated by sparging with nitrogen (high purity, >99.9%) for 30 minutes immediately prior to the addition of iron materials. Experiments were carried out in closed, 120-ml serum bottles in which the solution volume was 100 ml. After an appropriate amount of iron material was added to the solution, the bottle was capped with a Teflon-lined cap and placed on a mechanical shaker at 25°C. After a predetermined time period, a solution sample was withdrawn and the solid residues were harvested by vacuum filtration, dried and stored in a N<sub>2</sub>-filled glove box.

#### 4.2.3 XPS analysis

Dried samples of nZVI after reaction with As(III) were characterized using High Resolution X-ray Photoelectron Spectroscopy (HR-XPS) performed on a Scienta ESCA 300 spectrometer equipped with an 8 kW-rotating anode and seven toroidally bent  $\alpha$ -quartz crystals [17] for providing monochromated AlK $\alpha$  ( $h\nu = 1486.7$  eV) radiation. A 300-mm radius hemispherical analyzer and position-sensitive detector was used for signal detection, which provides high energy resolution at improved signal-to-noise ratios. Samples were mounted on a stainless steel stub and transferred to the analysis chamber ( $5.0 \times 10^{-9}$  Torr). Spectra were obtained using a takeoff angle of 90° with respect to the

surface plane of the sample stub. Survey scans of the samples were obtained at 300-eV pass energy, while scans of smaller energy regions for As3d, As2p<sub>3/2</sub>, Fe2p, C1s, and O1s spectra were obtained at 150-eV pass energy.

Each spectrum was calibrated against the binding energy (BE) for adventitious carbon detected in the C1s region (284.6 eV BE). Curve fitting for As3d and As2p<sub>3/2</sub> spectra was carried out using the CASA XPS MFC Application software, version 2.3.12.8. For the curve-fitting procedure, a Shirley background was used to account for inelastic scattering and all peaks were described using a Gaussian/Lorentzian ratio of 70/30. The full-width-at-half-maximum (FWHM) of each component peak was set to 1.15 eV for As3d spectra and 1.64 eV for As2p<sub>3/2</sub> spectra [18]. The As3d<sub>5/2</sub> and As3d<sub>3/2</sub> components of the As3d spin orbit-split doublet peak were fixed at a constant intensity ratio of 3:2 and at a fixed separation of 0.70 eV.

#### 4.3 Results and Discussion

Samples for HR-XPS analysis were prepared by incubating nZVI or iron oxides (5 g/L) with 1.3 mM As(III) solutions in closed vials for 24 hours. Solution-phase analysis indicated that the aqueous arsenic concentration decreased to below 1 μM after 1 hour of mixing with nZVI, whereas 87-89% of the arsenic remained in solutions after 24 hours of mixing with Fe<sub>2</sub>O<sub>3</sub> and Fe<sub>3</sub>O<sub>4</sub>. HR-XPS spectra for two arsenic core-levels widely separated in binding energy (BE), As2p<sub>3/2</sub> (~1326 eV BE) and As3d (~44 eV BE), were collected using a monochromated Al Kα source (1486.7 eV). Due to the large BE differences in these core levels, the photoelectrons analyzed in these spectra have markedly different kinetic energies and thus “escape depths” (3λ, where λ is the attenuation length or mean free path for inelastic scattering at the respective kinetic



energy), which are estimated to be 1.4 nm and 6.8 nm, respectively, in FeOOH based on the semi-empirical CS2 equation [19]. The different surface sensitivity of each of these As $2p_{3/2}$  and As $3d$  spectra enables us to resolve the distribution of arsenic species within a ~7nm thick surface region (Figure 4.2). This approach has advantages over other methods, e.g., depth-profiling by angle-resolved XPS measurements, which is especially complicated by the spherical geometry and size distribution of the nanoparticles. This depth-dependent information cannot be obtained by bulk analysis or less surface sensitive techniques such as EXAFS, while solid phase extraction, a technique frequently employed in arsenic geochemistry studies [1,5] is inherently destructive.

#### 4.3.1 Analysis of depth-dependent distribution of multiple As valence states within nZVI and iron oxides ( $Fe_3O_4$ and $Fe_2O_3$ )

Figure 4.3a and 4.3b show As $2p_{3/2}$  and As $3d$  spectra of different iron materials that have been reacted with As(III) solutions for 24 hours. Curve-fitting was used to elucidate the contributions of arsenic species with different oxidation states to the observed spectral peaks. In Figure 4.3, each arsenic oxidation state gives rise to two peaks in the As $3d$  spectra, due to the spin orbit-split As $3d_{5/2}$  and As $3d_{3/2}$  components present at a constant intensity ratio and fixed separation, and a single peak in the As $2p_{3/2}$  spectra. For  $Fe_2O_3$  and  $Fe_3O_4$  particles, approximately 40 at.% of the original As(III) was found to be oxidized to As(V). All solutions were sparged with pure  $N_2$  for 30 minutes immediately before the introduction of iron materials, so direct oxidation of As(III) by dissolved oxygen was avoided. It has been reported that iron oxide surfaces, such as hematite and maghemite, may cause As(III) oxidation under alkaline conditions [20,16], which is consistent with the conditions we observed here, where the solution pH was

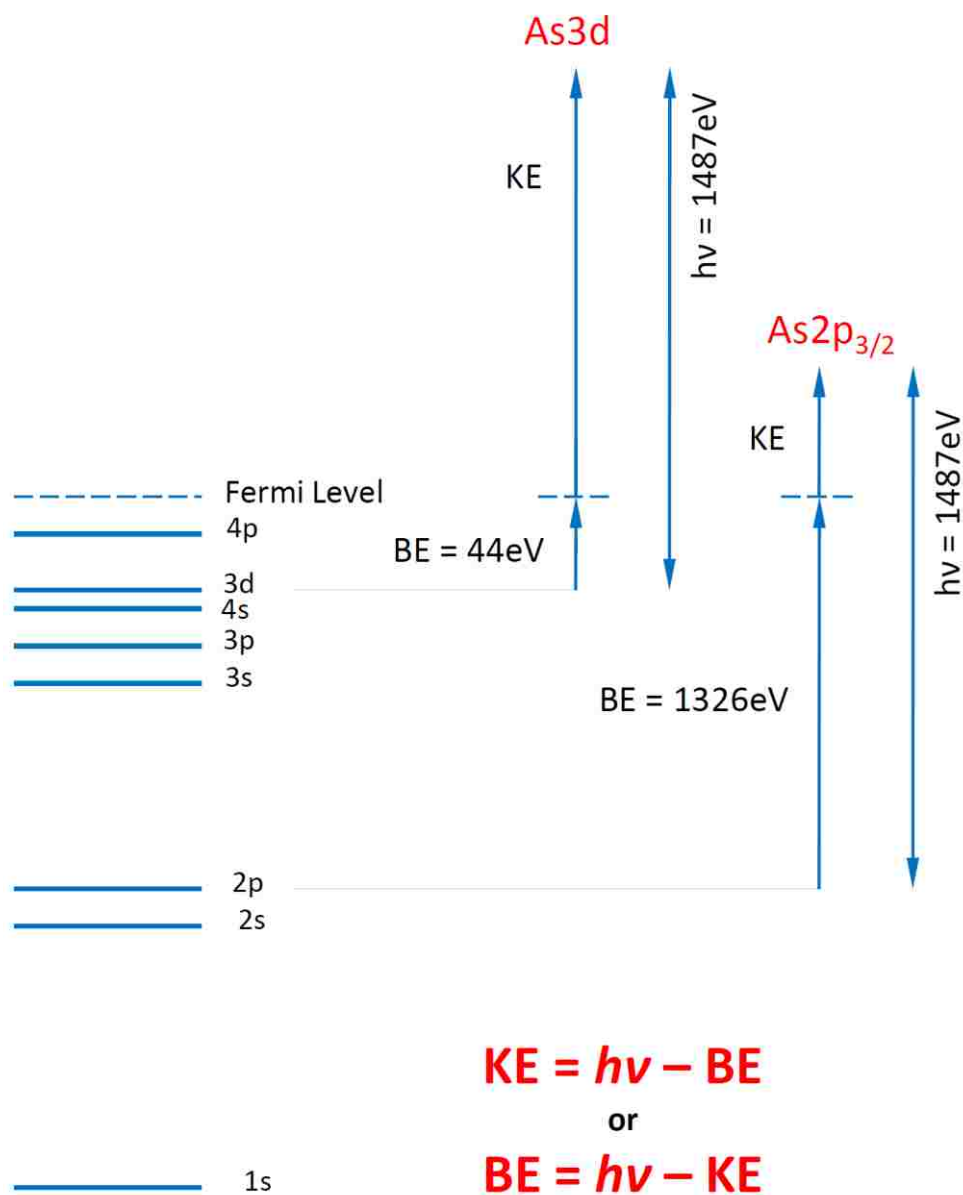


Figure 4.2 Elements whose spectra exhibit photoelectron lines widely spaced in Kinetic Energy (KE) (e.g. As lines 2p and 3d) can be located using the intensity ratio of the lines. In general, electrons with lower KE are attenuated more when moving through a solid phase, whereas those of higher KE have a greater escape path. Thus for a surface species the lower KE component will be stronger than the higher KE component.

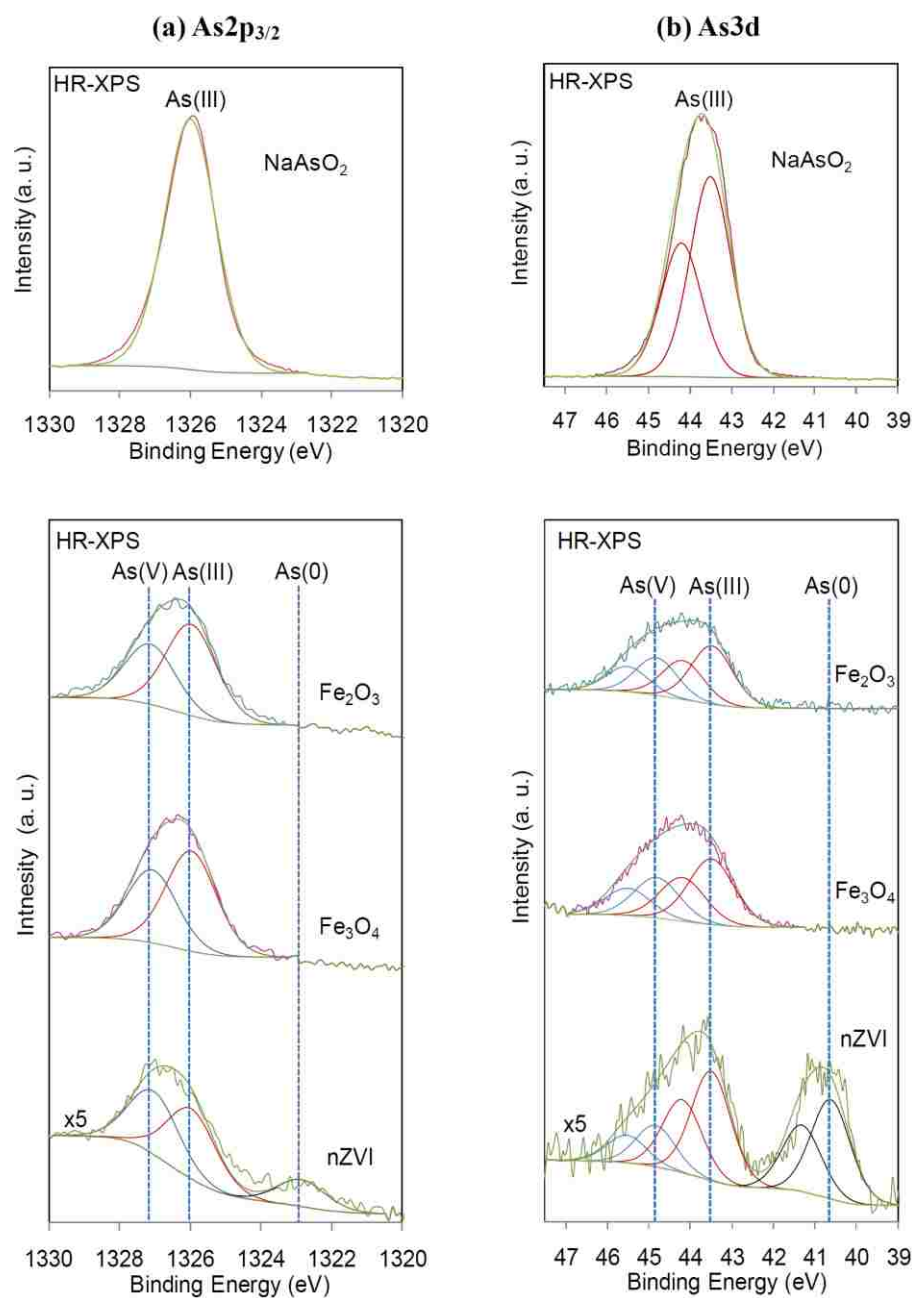


Figure 4.3 HR-XPS spectra of (a)  $As2p_{3/2}$  and (b)  $As3d$  regions of various Fe materials reacted with  $As(III)$  solutions. These two core-levels were chosen because of the widely spaced kinetic energies of the respective photoelectrons and hence difference in surface sensitivity.  $As2p_{3/2}$  spectra arise from photoemission from a shallower depth than does  $As3d$  spectra. The top spectrum of each column is that of pure sodium arsenite ( $NaAsO_2$ ), which was used to prepare the  $As(III)$  solutions used in these experiments. The vertical scale of the two spectra from the nZVI sample is enlarged five-fold. Samples were prepared by reacting 5g/L of the iron oxides or nZVI with deoxygenated 1.3 mM  $As(III)$  solutions for 24 hours.

measured to be 9.2 – 10.1 (Table 4.2.). In addition, a recent study suggests that Fe(II)-Fe(III) surfaces are capable of inducing As(III) oxidation in anoxic conditions [17].

HR-XPS spectra of the nZVI sample in Figure 4.3 reveal the presence of As(V) and As(0) species in addition to the initially loaded As(III) species. The observation of multiple arsenic valence states confirms our prior observation that nZVI exhibits a combination of reactivity that includes adsorptive, reductive and oxidative abilities towards As(III) [21]. However, deconvolution of the spectra shows that the apparent proportions of arsenic species at different oxidation states differs significantly in the As2p<sub>3/2</sub> and As3d spectra. In particular, arsenic present as As(0) constitutes 40 at.% of the total in the As3d spectrum, while it contributes only 16 at.% in the As2p<sub>3/2</sub> spectrum (Table 4.3,4.4,4.5). The opposite trend is observed for As(V) species. These observations indicate that arsenic species with different valence states are distributed differently within the surface region of the solid phase.

Depth-dependent distributions from Figure 4.3 can be calculated by utilizing the ratio of the As2p<sub>3/2</sub> to As3d peak areas, after correcting each by a relative sensitivity factor (RSF) to account for the difference in ionization cross-sections and instrument-dependent response functions [22,23]. A homogeneous solid sample, NaAsO<sub>2</sub>, which is the precursor of As(III) solutions used in the experiments, was analyzed to confirm the validity of this approach and its spectra are shown in the figures for reference. On the basis of the different surface sensitivity of As2p<sub>3/2</sub> and As3d lines, arsenic species that are homogeneously distributed in the surface region, i.e., with depth-independent concentration, should have an As2p<sub>3/2</sub>/As3d intensity ratio around unity, which is clearly the case for NaAsO<sub>2</sub> shown in Figure 4.4. Arsenic species that are more concentrated at

Table 4.2 As(III) batch experiment conditions

<b>Iron material</b>	<b>Initial conditions</b>	<b>Reaction Time</b>	<b>Initial pH</b>	<b>Final pH</b>	<b>Final <math>E_h</math>, mV</b>
Fe <sub>2</sub> O <sub>3</sub>	As(III) 100 mg/L, Fe <sub>2</sub> O <sub>3</sub> 5 g/L	24 h	10.0	10.0	306
Fe <sub>3</sub> O <sub>4</sub>	As(III) 100 mg/L, Fe <sub>3</sub> O <sub>4</sub> 5 g/L	24 h	10.1	9.9	279
nZVI	As(III) 100 mg/L, nZVI 5 g/L	24 h	10.0	9.2	-90

Table 4.3 Curve-fitting parameters for As2p<sub>3/2</sub> and As3d HR-XPS spectra and the relative areas of the peak components arising from different arsenic oxidation states.

<b><u>BE (eV)</u></b>	<b>As 2p<sub>3/2</sub></b>			<b>As 3d</b>		
	<u>As(V)</u>	<u>As(III)</u>	<u>As(0)</u>	<u>As(V)</u>	<u>As(III)</u>	<u>As(0)</u>
	1327.1	1326.0	1323.1	44.8 <sup>a</sup>	43.5 <sup>a</sup>	40.6 <sup>a</sup>
<b><u>FWHM (eV)</u></b>	1.64	1.64	1.64	1.15	1.15	1.15
<b><u>Relative Area</u></b>						
NaAsO <sub>2</sub>	0	100	0	0	100	0
Fe <sub>2</sub> O <sub>3</sub>	40	60	0	40	60	0
F <sub>3</sub> O <sub>4</sub>	42	58	0	38	62	0
nZVI	41	43	16	16	44	40

<sup>a</sup> Binding energy of the As3d<sub>5/2</sub> peak. The spin-orbit splitting of the As3d peaks was fixed at 0.7 eV.

Table 4.4 Integrated peak areas of the XPS spectra taken for each sample

<b>Sample</b>	<b>C1s</b>	<b>O1s</b>	<b>Fe2p<sub>3/2</sub></b>	<b>As3d</b>	<b>As2p<sub>3/2</sub></b>
<b>NaAsO<sub>2</sub></b>	309.4	2887.1	0	779.6	13476
<b>Fe<sub>2</sub>O<sub>3</sub></b>	258.3	1397.1	3421.3	35.5	1192.6
<b>Fe<sub>3</sub>O<sub>4</sub></b>	206.9	1478.6	3331.7	40	1151.8
<b>nZVI</b>	115.4	1188.3	2529.3	16.4	183.4

Table 4.5 Apparent elemental concentrations (at. %) for major elemental components <sup>a</sup>

Sample	C	O	Fe	As <sup>b</sup>
<b>NaAsO<sub>2</sub></b> <sup>c</sup>	13.3%	42.4%	0%	18.3%
<b>Fe<sub>2</sub>O<sub>3</sub></b>	26.8%	49.5%	21.7%	2.03%
<b>Fe<sub>3</sub>O<sub>4</sub></b>	22.1%	53.9%	21.7%	2.34%
<b>nZVI</b>	16.2%	62.8%	19.6% <sup>d</sup>	1.41%

<sup>a</sup> Composition as atomic percent for each element *i* was calculated according to Eq. (1)

$$C_i = \frac{A_i/S_i}{\sum_i A_i/S_i} \quad (1)$$

where  $A_i$  is the measured peak area (as shown in Table 4.4) and  $S_i$  is the relative sensitivity factor. These latter values were taken from literature [24] as:  $S(\text{C1s})=1.0$ ,  $S(\text{O1s})=2.93$ ,  $S(\text{Fe2p})=16.4$ , and  $S(\text{As3d})=1.82$ . The value of  $S(\text{As2p})$  was determined empirically from a pure  $\text{As}_2\text{O}_3$  sample to be 31.5. The values shown in the table are apparent concentrations because of the inherent assumption in the calculation that each element is distributed homogeneously throughout the probe depth.

<sup>b</sup> Calculated from As3d signals. If using As2p<sub>3/2</sub> spectra, the apparent elemental concentrations obtained will be different due to As2p<sub>3/2</sub> line having smaller escape depth.

<sup>c</sup> The balance percentage is sodium.

<sup>d</sup> Among the iron detected by XPS, approximately 2.7% appears to be Fe(0).



the surface will have a  $\text{As}2p_{3/2}/\text{As}3d$  ratio greater than one, and conversely, arsenic species enriched in subsurface layers will have a ratio less than one.

As shown in Figure 4.4 for  $\text{Fe}_2\text{O}_3$  particles, the  $\text{As}2p_{3/2}/\text{As}3d$  ratios of As(III) and As(V) are well above one (2.2), indicating that both types of species are located in a thin surface layer. Quantitative analysis drawing on the correlation between photoelectron intensity and emission depth [23,25] yields a thickness of  $\sim 0.7$  nm for this arsenic-laden layer [26]. Considering that the monolayer thickness of an arsenic-iron oxide inner-sphere complex is  $\sim 0.6$  nm, on the basis of the Fe-As distance measured by X-ray absorption studies and the radius of OH ligands [11,12,20], our results indicate strongly that As(III) and As(V) are bound as a surface complex layer on the  $\text{Fe}_2\text{O}_3$  particles. For  $\text{Fe}_3\text{O}_4$ , a similar spatial distribution profile is obtained, with As(III) occurring in a slightly thicker layer ( $\sim 1.3$  nm) than As(V) ( $\sim 0.8$  nm), suggesting short-range diffusion of As(III) into the particles, possibly via micropores or defect sites in  $\text{Fe}_3\text{O}_4$  [27]. Arsenic species detected in the nZVI sample display a marked disparity in the  $\text{As}2p_{3/2}/\text{As}3d$  intensity ratios, as shown in Figure 4.4. As(V), with  $\text{As}2p_{3/2}/\text{As}3d = 2.1$ , is clearly enriched at the surface. As(III), with a ratio of 0.82, is present fairly uniformly across the sampling depth. In contrast, As(0), with  $\text{As}2p_{3/2}/\text{As}3d = 0.34$ , is localized in the subsurface region.

In addition, the Fe2p HR-XPS spectra of this sample showed a small peak at 707.0 eV corresponding to Fe(0) (Figure 4.5). The presence of this peak indicates that the metallic core is enclosed by only a thin oxide shell. Following our previous approach to quantifying the oxide layer thickness from the relative intensity of the metallic and oxidized iron peaks [14,25], we estimate that the average oxide thickness of this nZVI

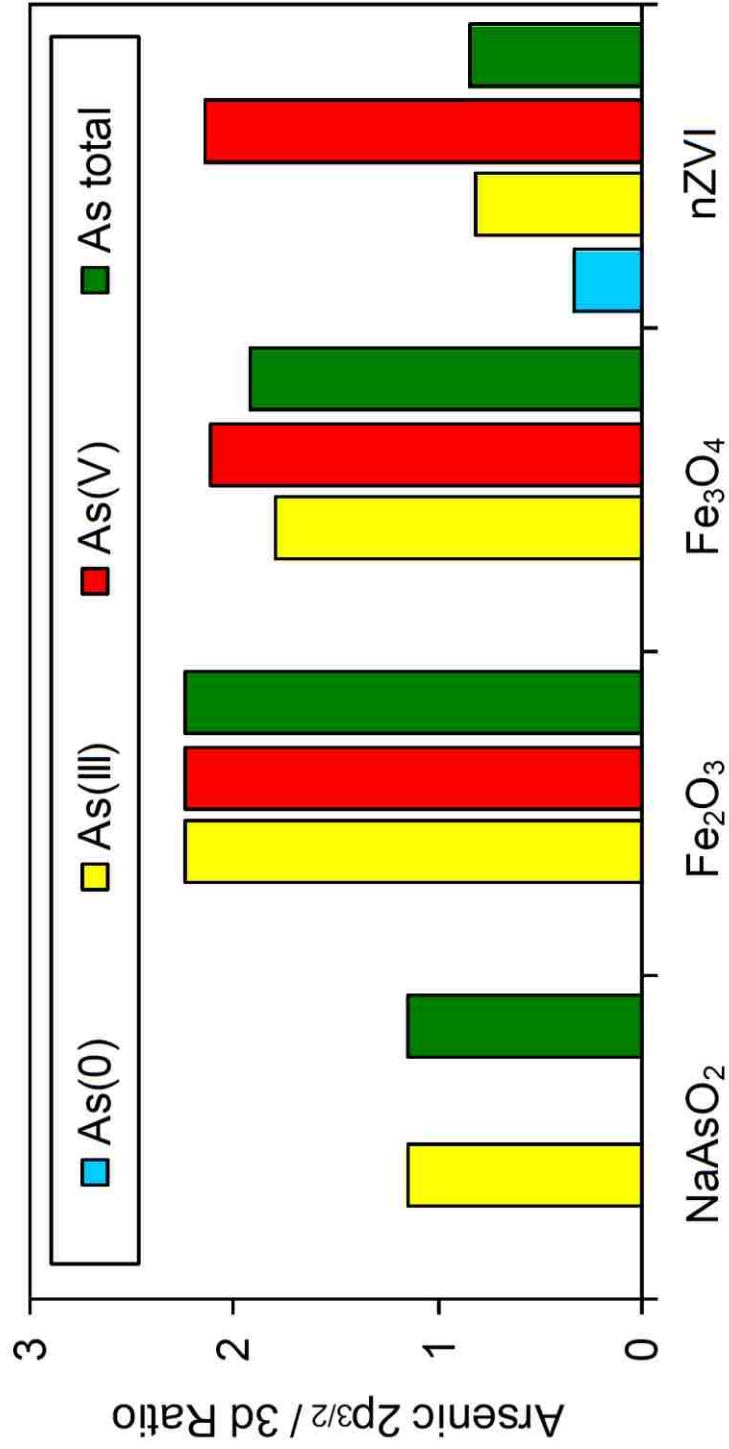


Figure 4.4 Normalized intensity ratios of the As<sub>2</sub>p<sub>3/2</sub> to As<sub>3</sub>d peaks in HR-XPS spectra.

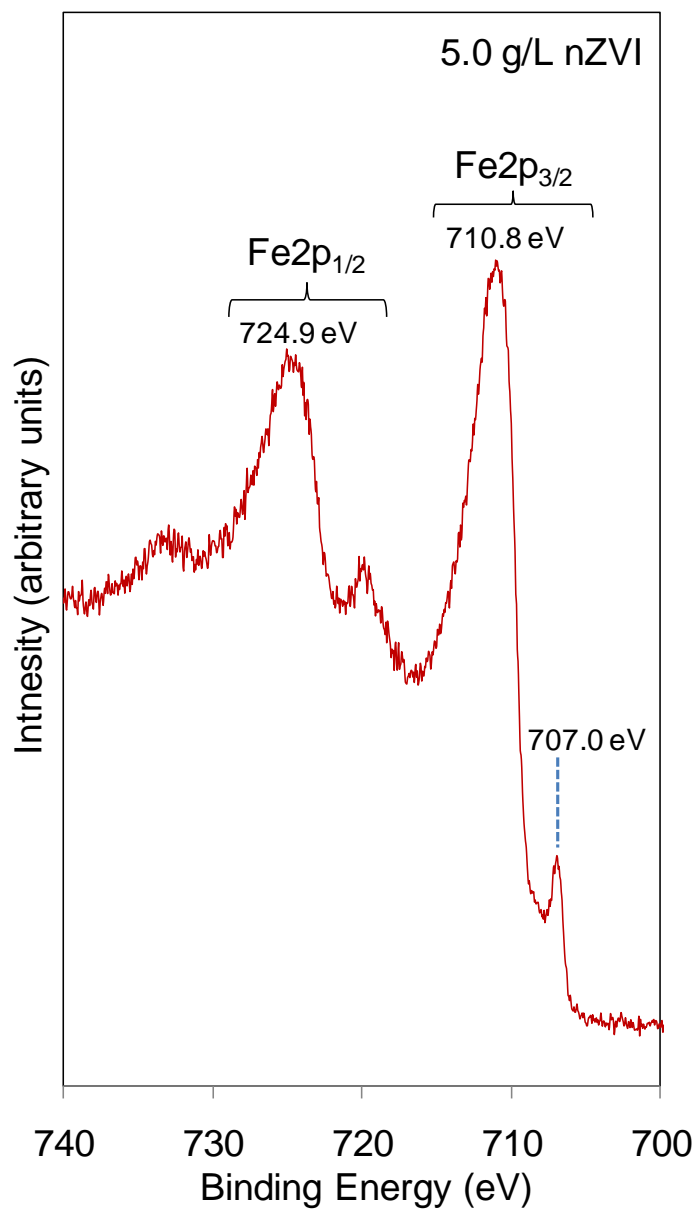


Figure 4.5 Fe2p HR-XPS spectra of nZVI reacted with an 100 mg/L As(III)solution for 24 hours. The small peak at 707.0 eV BE corresponds to the Fe2p<sub>3/2</sub> signal from Fe(0) and the larger peak at 710.8 eV BE corresponds to the Fe2p<sub>3/2</sub> signal from oxidized Fe. Using the Fe2p<sub>3/2</sub> intensities observed for metallic and oxidized iron, the average thickness of the oxide layer can be calculated to be 4.2 nm using the XPS Multi-Quant software [22].

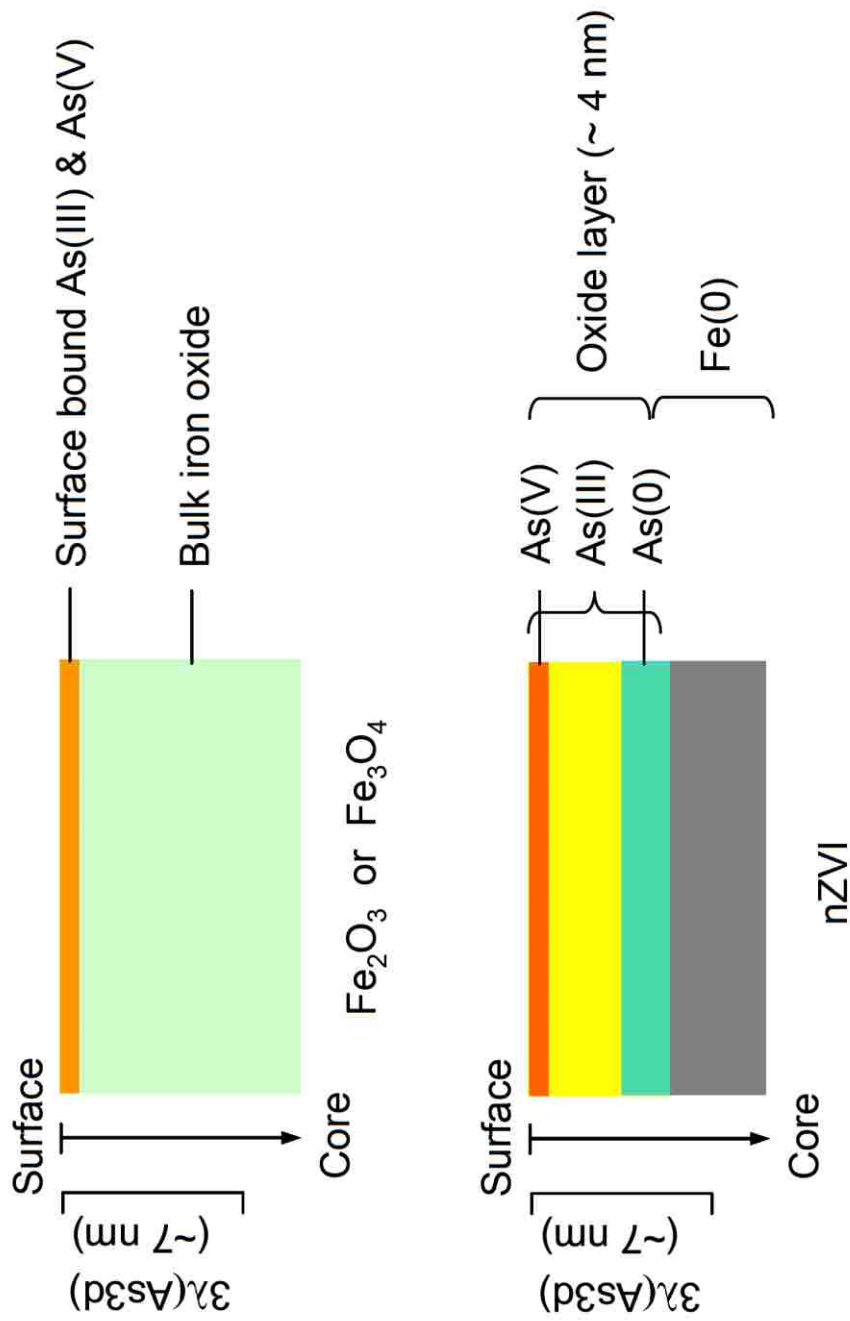


Figure 4.6 Schematic illustrations of the depth distribution of arsenic species in iron oxides and nZVI. The left-hand scale bars indicate the escape depth ( $3\lambda$ ) of As3d photoelectrons in iron (oxy)hydroxide (FeOOH). The thickness of the surface oxide layer for nZVI is calculated from the relative intensities of metallic and oxidized iron contributions in the Fe2p spectra

sample is 4.2 nm, which is an increase of ~2 nm over that of the freshly made nZVI sample [14].

The As $2p_{3/2}$  photoelectrons are strongly attenuated by traversing through this oxide shell, while the As $3d$  photoelectrons are not so much. Thus it is reasonable to infer that the As(0) signals emanate mainly from a region close to the core-shell interface. This is shown in Figure 4.6, which provides a schematic illustration of the depth distribution of arsenic based on the present analysis. Due to the probing depth limitations of our data, we are unable to ascertain whether As(0) is further dispersed into the metallic Fe within the core of the particles. Additional studies are currently underway using depth-profiling by ion sputtering to probe the composition of the interior core region.

#### 4.4 Conclusion

The stratified concentration profiles of arsenic species in nZVI expose several novel aspects of the reactions between As(III) and nZVI. The results offer clear evidence of As(III) redox reactions within the nanoparticles. The distinct layers where As(V) and As(0) reside imply As(III) oxidation and reduction occur at different physical fronts. Surface enrichment of As(V) is consistent with an adsorption/oxidation model in which As(III) attaches to the surface coordination sites and subsequent oxidation is facilitated by electron transfer across the complex structure coupled with rearrangement of H $_2$ O or OH $^-$  ligands [17,28]. On the other hand, As(0) residing predominantly in subsurface layers implies that the reduction takes place near the metallic core. Since this would entail inward diffusion of As(III) species and migration of reductants from the core region, we expect As(III) reduction to be more kinetically limited than As(III) oxidation. This agrees with our time-dependent studies of nZVI samples that show gradual

formation of As(0) over a 24-hour period, in contrast to the much more rapid formation of As(V). A detailed discussion of this subject will be covered in a separate paper. The dynamic transformations of arsenic species in the solid phase represent a new aspect of arsenic-iron chemistry previously unexamined and these processes are expected to have a deep impact on the stability and mobility of the solid-bound arsenic.

Figure 4.4 shows that the  $As_{2p_{3/2}}/As_{3d}$  ratio for the total arsenic detected in nZVI, obtained by summing together all of the different arsenic species present, has a value of 0.8. This implies that the majority of arsenic is buried underneath the surface. The ability to impregnate arsenic into the solid phase renders nZVI a potentially more voluminous sink for arsenic compared to the widely used iron oxides, whose capacities are limited by the available surface coordinative sites and are subject to competition from co-existing anions in the water [13]. This feature of nZVI is supported by a much higher efficacy of nZVI for As(III) removal relative to that of the iron oxides as observed in our solution experiments. Furthermore, infiltration of arsenic induced by reactions with Fe(0) may offer an engineering methodology to encapsulate arsenic for remediation and waste disposal applications. In this context, continuing studies to evaluate the performance of nZVI for As(III) treatment in a broad spectrum of environmental conditions is warranted.

## REFERENCES FOR CHAPTER IV

1. Smedley, P. L.; Kinniburgh, D. G., *Appl. Geochem.* **2002**, *17*, 517.
2. Nordstrom, D. K., *Science* **2002**, *296*, 2143-2145. Kanel, S. R.; Manning, B.; Charlet, L.; Choi, H., *Environ. Sci. Technol.* **2005**, *39*, 1291.
3. Kanel, S. R.; Greneche, J. M.; Choi, H., *Environ. Sci. Technol.* **2006**, *40*, 2045.
4. Su, C. M.; Puls, R. W., *Environ. Sci. Technol.* **2001**, *35*, 1487.
5. Lackovic, J. A.; Nikolaidis, N. P.; Dobbs, G. M., *Environ. Engin. Sci.* **2000**, *17*, 29.
6. Lien, H. L.; Wilkin, R. T., *Chemosphere* **2005**, *59*, 377.
7. Hussam, A.; Munir, A. K. M., *J. Environ. Sci. Health Part A* **2007**, *42*, 1869.  
Bang, S.; Johnson, M. D.; Korfiatis, G. P.; Meng, X. G., *Water Research* **2005**, *39*, 763.
8. Goldberg, S.; Johnston, C. T., *J. Colloid Interface Sci.* **2001**, *234*, 204.
9. Manning, B. A.; Fendorf, S. E.; Goldberg, S., *Environ. Sci. Technol.* **1998**, *32*, 2383.
10. Manceau, A., *Geochim. Cosmochim. Acta* **1995**, *59*, 3647.
11. Dixit, S.; Hering, J. G., *Environ. Sci. Technol.* **2003**, *37*, 4182.
12. Martin, J. E.; Herzing, A. A.; Yan, W. L.; Li, X. Q.; Koel, B. E.; Kiely, C. J.; Zhang, W. X., *Langmuir* **2008**, *24*, 4329.
13. Sun, Y. P.; Li, X. Q.; Cao, J. S.; Zhang, W. X.; Wang, H. P., *Adv. Colloid Interface Sci.* **2006**, *120*, 47.
14. Cumpson, P. J.; Seah, M. P., *Surf. Interface Anal.* **1997**, *25*, 430.

15. Manning, B. A.; Hunt, M. L.; Amrhein, C.; Yarmoff, J. A., *Environ. Sci. Technol.* **2002**, *36*, 5455.
16. Ramos, M. A. V.; Yan, W.; Li, X. Q.; Koel, B. E.; Zhang, W. X., *J. Phys. Chem. C* **2009**, *113*, 14591.
17. Moulder, J. F.; Stickle, W. F.; Sobol, P.E.; Bomben, K. D., *Handbook of X-ray Photoelectron Spectroscopy*; Perkin-Elmer Corporation, Eden Prairie, MN, 1992.
18. Contour, J. P.; Massies, J.; Fronius, H.; Ploug, K., *Jpn. J. Appl. Phys.* **1988**, *27*, L167.
19. Manning, B. A.; Goldberg, S., *Environ. Sci. Technol.* **1997**, *31*, 2005.
20. Amstaetter, K.; Borch, T.; Larese-Casanova, P.; Kappler, A., *Environ. Sci. Technol.* **2010**, *44*, 102.
21. Briggs, D.; Seah, M. P. (Eds.), *Practical Surface Analysis*, Vol. 1: *Auger and X-ray Photoelectron Spectroscopy*, John Wiley & Sons, New York, 1990.
22. Mohai, M., *XPS Multiquant Users Manual*; **2005**.
23. For the Fe<sub>2</sub>O<sub>3</sub> sample, the normalized ratio of As2p<sub>3/2</sub> and As3d peaks suggests that the sequestered arsenic is present in a surface overlayer. Applying the relationship between the intensity of an XPS line *i* (*I<sub>i</sub>*) and the thickness of the overlayer (*d*) from which the photoelectron signals are generated,  $I_i = X_{As} I_i^\infty (1 - \exp(-d/\lambda_i \cos\theta))$  (where  $X_{As}$  is the average concentration of arsenic in the overlayer,  $I_i^\infty$  is the intensity of line *i* for a pure homogeneous arsenic sample,  $\lambda_i$  is the electron inelastic mean free path for line *i*, and  $\theta$  is the take-off angle) to As2p<sub>3/2</sub> and As3d peaks, respectively, and replace the bulk intensities by the relative sensitivity factors (RSF), we obtain the relationship between the intensity ratio of As2p<sub>3/2</sub> and As3d peaks, after correcting each by the respective RSF, and *d* at a normal take-off angle as:
 
$$(I_{As2p_{3/2}}/RSF_{As2p_{3/2}})/(I_{As3d}/RSF_{As3d}) = (1 - \exp(-d/\lambda_{As2p_{3/2}}))/(1 - \exp(-d/\lambda_{As3d}))$$
 Solving the above equation with the normalized intensity ratio (2.2) and the inelastic mean free paths of As2p<sub>3/2</sub> (0.47 nm) and As3d (2.1 nm) in Fe<sub>2</sub>O<sub>3</sub>, we obtain the value of *d* to be 0.7 nm. Note that in the above calculation, the effect due to a spherical topology of the sample can be neglected as *d* is much smaller than the mean diameter of the nanoparticle (60 nm). Similar calculation applies to the Fe<sub>3</sub>O<sub>4</sub> sample.
24. Fairley, N.; Carrick, A., *The Casa Cookbook – Part 1: Recipes for XPS data Processing*, Acolyte Science, Cheshire, WA 16 16LZ U.K., 2005.
25. Axe, L.; Trivedi, P., *J. Colloid Interface Sci.* **2002**, *247*, 259.



26. Scott, M. J.; Morgan, J. J., *Environ. Sci. Technol.***1995**, 29, 1898.
27. Mohan, D.; Pittman, C. U., *J. Hazardous Mat.***2007**, 142, 1.
28. Korte, N. E.; Fernando, Q., *Crit. Rev. Environ. Control* **1991**, 21, 1.

## CHAPTER V

### REMOVAL OF AS(III) BY IRON NANOPARTICLES (NZVI): INVESTIGATION OF SOLID-PHASE ARSENIC-IRON REACTIONS

#### 5.1 Introduction

High levels of arsenic in groundwater pose a serious health threat to millions of people around the world [1,2]. The situation is of particular concern in rural areas of developing countries such as Bangladesh, India, Vietnam, and Cambodia, where there is no centralized water treatment facility and the contaminated groundwater is heavily utilized for drinking and irrigation of food crops [3,4]. Severe health implications including cancers have been traced to long-term arsenic intake [5], and the WHO guideline imposes a stringent limit of 10  $\mu\text{g/L}$  for arsenic in drinking water [6].

Many options have been explored for arsenic removal and these include coagulation, adsorption, ion exchange, and membrane processes [7-10]. Coagulation with alum or ferric chloride is commonly used in large-scale water treatment plants and can be further optimized for arsenic removal [7], whereas sorbents such as metal oxides or ion-exchange-based filtration units can be tailored for household or small community use and are currently a more practical solution in rural regions of the affected countries [8-10]. The principal forms of arsenic in the aqueous environment are arsenite (predominantly as  $\text{H}_3\text{AsO}_3$ ) and arsenate (as  $\text{H}_2\text{AsO}_4^-$  or  $\text{HAsO}_4^{2-}$ ) [11,12]. Amorphous or crystalline iron

oxides possess strong affinity for both As(V) and As(III) species. Under neutral or alkaline pH, As(III) adsorbs to a greater extent than As(V) onto iron oxide surfaces via inner-sphere complex formation [11,13-14] and the molecular structures of arsenic-iron oxide complexes have been characterized by advanced spectroscopic techniques [14-17].

Recent studies have shown that zero-valent iron is an effective remediation agent for treating arsenic-laden groundwater or drinking water [18-22]. It is generally conceived that As(III) or As(V) is removed by adsorbing to the iron oxide layer on the ZVI particles [18,20] or forming co-precipitates with iron hydroxide produced during *in situ* iron corrosion [19,22]. However, spectroscopic investigations of arsenic speciation in ZVI materials reveal that the immobilized arsenic is converted to different oxidation states from their aqueous forms, suggesting arsenic redox transformations have played an active part in the remediation process. X-ray photoelectron spectroscopy (XPS) analysis by Su *et al.* detected no reduction of As(III) by ZVI filings but partial oxidation of As(III) to As(V) [18]. Manning *et al.* reported similar findings with X-ray absorption spectroscopy (XANES and EXAFS) for ZVI powders reacted under aerobic conditions, where they proposed the oxidation of As(III) might be mediated by iron corrosion products such as magnetite/maghemite or lepidocrocite [20]. On the other hand, Bang *et al.* found a fraction of As(III) being reduced to As(0) on an acid-pretreated iron coupon under anoxic conditions [21]. The variations in the experimental parameters and the limited spectroscopic data sets available make it difficult to interpret these results on a consistent basis.

In recent years, attention has been focused on nanoscale zero-valent iron (nZVI) for its effectiveness in treating halogenated hydrocarbons, hexavalent chromium and

other heavy metal species in water [23-25]. The particles' small size gives rise to an increased surface area, greater remediation capacity, and favorable field injection and transport properties for *in situ* remediation. While the nanoparticles have shown a remarkable efficacy to immobilize aqueous arsenic species [26-27], the reactions involved appear to be more complex than those of iron oxide based sorbents and the bulk-sized ZVI materials. It was observed that aqueous As(III) was sequestered in multiple oxidation states (i.e., As(V), As(III), and As(0)) on nZVI, implying the nanoparticles possess both arsenite oxidation and reduction capabilities [28]. Previous characterization shows nZVI consists of a reactive Fe(0) phase enclosed by a thin layer of amorphous iron oxide averaging ~ 3 nm in thickness [29]. The fine scale and the defective nature of the oxide film may increase the rates of charge transfer or mass diffusion processes, thus the nanoparticles exhibit interesting redox behaviors on a relatively small time scale, which may not manifest to an appreciable extent in the bulk iron counterparts. In this context, studying nZVI-arsenic interactions will not only help to reveal the mechanisms underlying nZVI's efficient arsenic sequestration performance, but also provide an additional means to study arsenic-iron chemistry and the fate and stability of sequestered arsenic species. In this work, high-resolution X-ray photoelectron-spectrometry (HR-XPS) is employed to investigate solid-phase arsenic speciation upon reactions between nZVI and aqueous As(III). High surface sensitivity and the availability of quantitative information on arsenic in different valence states make XPS a powerful tool for the purpose of this study. Specifically, we compared arsenic speciation in reacted nZVI with that in model iron oxide compounds under similar conditions to understand the difference in reactivity of nZVI relative to that of the well-

characterized iron oxides. We also evaluated the effects of reaction time and nZVI dose on the reaction products, which in conjunction with solution phase analysis, allows us to propose a more detailed reaction model between As(III) and nZVI.

## **5.2 Materials and Methods**

### **5.2.1 Preparation of iron materials**

Iron nanoparticles (nZVI) were synthesized by reacting sodium borohydride with ferric chloride as reported previously [29,31]. Two iron oxides,  $\text{Fe}_3\text{O}_4$  and  $\text{Fe}_2\text{O}_3$  (>99%, Fisher Chemical), were used in this study as references since As(III) reactions with iron oxides have been extensively studied [11-14,16-17]. XRD characterization shows that the predominant mineral phases for  $\text{Fe}_3\text{O}_4$  and  $\text{Fe}_2\text{O}_3$  are magnetite and hematite, respectively. The BET surface areas of all iron materials are summarized in Table 5.1.

### **5.2.2 Batch experiments**

As(III) and As(V) solutions were prepared from  $\text{NaAsO}_2$  and  $\text{Na}_2\text{HAsO}_4 \cdot 7\text{H}_2\text{O}$  (>98.5%, Fluka), respectively. Batch experiments of As(III) removal were performed in 120-ml serum bottles containing 100 ml of As(III) solution at 100 mg/L. The solution was deoxygenated by sparging with nitrogen (high purity, >99.9%) for 30 minutes immediately before the experiments. Upon adding an appropriate amount of iron material, the bottle was sealed with a screw cap lined with a Teflon-coated septum and placed on a mechanical shaker (250 rpm) at 25°C. After a predetermined reaction time, a batch reactor was sacrificed and the solids were separated from the solutions by vacuum filtration, dried and stored in a  $\text{N}_2$ -glovebox before XPS analysis. The solution samples

Table 5.1 Characteristics of iron-based materials used

<b>Iron material</b>	<b>Source</b>	<b>Mean diameter, nm</b>	<b>BET specific surface area, m<sup>2</sup>/g</b>	<b>Crystalline phase</b>
nZVI	This work (refer to ref [32] for preparation procedure)	60 <sup>a</sup>	29	Polycrystalline <i>bcc</i> Fe(0) <sup>b</sup>
Fe <sub>3</sub> O <sub>4</sub>	Fisher <sup>®</sup> , laboratory grade		30	Magnetite <sup>c</sup>
Fe <sub>2</sub> O <sub>3</sub>	Fisher <sup>®</sup> , certified >99% purity		42	Hematite <sup>c</sup>

<sup>a</sup> determined by acoustic spectrometry [32]

<sup>b</sup> determined by selected area electron diffraction (SAED) pattern, as shown in Figure 5.1

<sup>c</sup> determined by XRD analysis

were stored in 40-ml glass vials at 4° C prior to analysis. Samples were analyzed within 48 hours of preparation.

### 5.2.3 Aqueous phase analysis

Arsenic and iron concentrations in the solution phase were determined by inductively-coupled plasma-optical emission spectroscopy (ICP-OES; Perkin Elmer Optima 2100 DV), which has a detection limit of 50 µg/L and 10 µg/L for arsenic and iron, respectively. The pH and  $E_h$  values of the solutions after reactions were measured, respectively, with a pH probe (Orion) and an ORP probe with a Ag/AgCl reference electrode (Cole-Parmer). The reported  $E_h$  values are referenced to the standard hydrogen electrode (SHE).

### 5.2.4 Solid phase analysis using XPS/SEM/TEM/XRD

Dried samples of nZVI after reaction with As(III) were characterized using High Resolution X-ray Photoelectron Spectroscopy (HR-XPS) performed on a Scienta ESCA 300 spectrometer equipped with an 8 kW-rotating anode yielding monochromatic  $AlK\alpha$  ( $h\nu = 1486.7$  eV) radiation. A 300-mm radius hemispherical analyzer in conjunction with a position-sensitive detector provides high energy resolution at improved signal-to-noise ratios. Samples were mounted on a stainless steel stub coated with conductive carbon tape and transferred to the analysis chamber ( $5.0 \times 10^{-9}$  Torr). Spectra were obtained using a takeoff angle of 90° with respect to the surface plane of the samples. Samples were analyzed at C1s, O1s, As3d, and Fe2p regions, which account for the major elements present at the surface. In addition, As $2p_{3/2}$  photoelectrons, which have a smaller probing depth (~ 1.4 nm) than As3d photoelectrons (~7 nm) [30] were analyzed when needed to

investigate arsenic distributions in the near surface region. Each spectrum was calibrated against the binding energy (BE) of adventitious carbon detected in the C1s region (284.6 eV). Curve fitting was carried out using the CASA XPS MFC application software (version 2.3.12.8). A Shirley background was used to account for inelastic scattering and all peaks were described using a Gaussian/Lorentzian ratio of 70/30. The full-width-at-half-maximum (FWHM) of each component peak was set to 1.15 eV for As3d spectra, and 1.64 eV for As2p<sub>3/2</sub> spectra [33]. The As3d<sub>5/2</sub> and As3d<sub>3/2</sub> components of the As3d spin orbit-split doublet peaks were fixed at a constant intensity ratio of 3:2 and a constant separation of 0.70 eV.

The morphology of fresh nZVI particles was analyzed with a field-emission scanning electron microscope (SEM, Hitachi S-4300) at 3.0 kV. Transmission electron microscope (TEM) imaging was carried out in a JEOL 2000FX TEM equipped with a LaB<sub>6</sub> filament operating at 200 kV. High-resolution lattice imaging was performed using a JEOL 2200FS TEM with a field-emission gun operating at 200 kV. X-Ray diffractograms were obtained using a Rigaku diffractometer (Rigaku, Japan) with Cu K $\alpha$  radiation generated at 40 kV. Iron samples were scanned from a 2 $\theta$  range of 10 to 80° with a step size of 0.1° and scan rate of 60 s per step.

## **5.3 Results and Discussion**

### **5.3.1 Characterization of nZVI**

In the past few years, a number of studies have been published to establish the core-shell structure of nZVI particles [25,29-31]. Scanning electron microscope (SEM) images show that the synthesized nanoparticles clustered into loose aggregates as a result



of magnetic and/or electrostatic interactions (Figure 5.1a & b). The diameters of nanoparticles range mostly from 50 to 100 nm. The transmission electron microscope (TEM) image in Figure 5.1c shows that an individual particle consists of an electron-dense core in the center, which has an electron diffraction pattern characteristic of nanocrystalline *bcc* Fe(0), surrounded by a continuous, smooth layer of iron oxide. The high-resolution TEM micrograph in Figure 5.1d reveals no periodic lattice fringes in the oxide phase, indicating the bulk of the oxide is amorphous in character. Examination of a few dozens of particles using TEM shows the thickness of the oxide layer varies between 2-5 nm. These observations agree with an estimated average oxide thickness of ~ 3 nm in our prior study [29]. Iron and oxygen contents in fresh nZVI particles were measured using temperature programmed reduction (TPR). The average oxygen content of fresh nZVI was 8.2%; total iron content of nZVI was 90%, among which zero-valent iron (Fe(0)) was estimated at 76% [34].

### 5.3.2 As(III) removal from the aqueous phase

High efficacy of arsenic removal by nZVI has been reported in previous studies at a concentration range typical of arsenic-laden groundwater (10-1000  $\mu\text{g/L}$ ), where solution-based experiments were conducted to study the removal kinetics and the effects of iron loading and solution pH on arsenic uptake [26-27]. To directly examine arsenic reactions in the solid phase, higher concentrations are needed to ensure adequate arsenic presence in the solids for accurate speciation analysis. Even for XPS analysis using the high-intensity Scienta ESCA 300, a minimal aqueous concentration of 10 mg/L is needed to generate a convenient amount of arsenic (>0.1 at.%) in nZVI. For most experiments

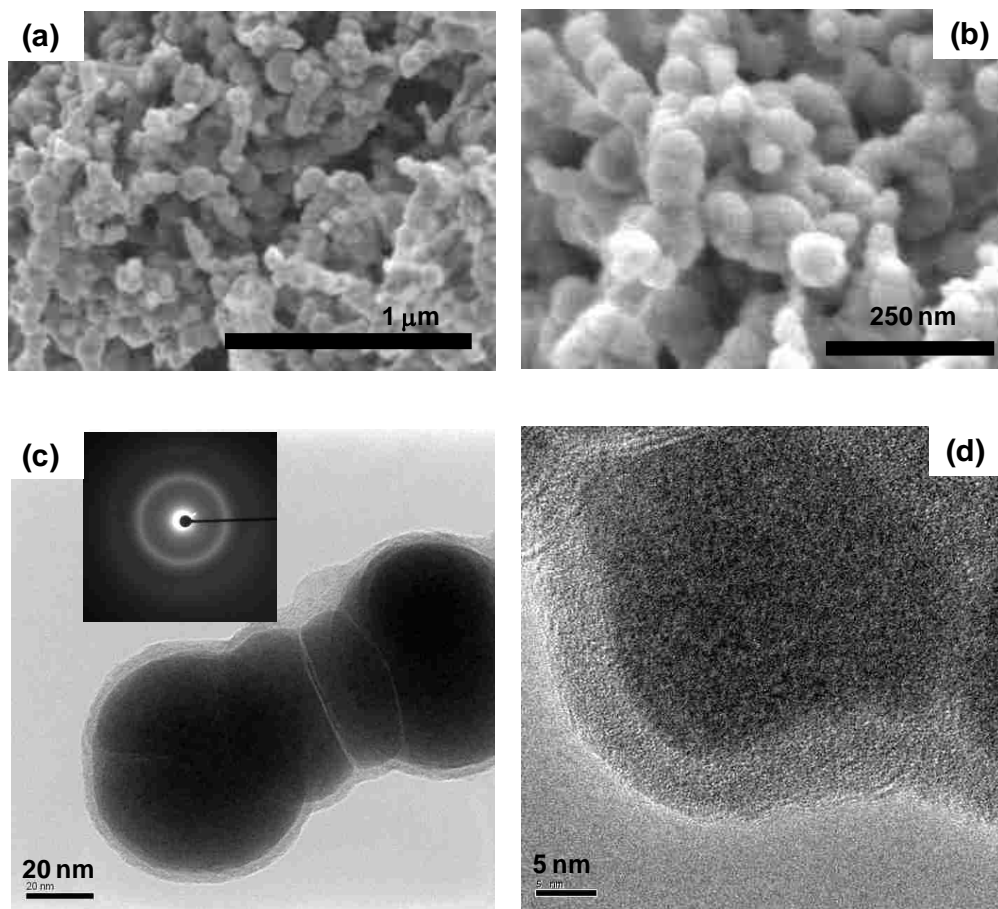


Figure 5.1 (a)-(b) Field-emission SEM micrographs of freshly made nZVI nanoparticles showing the particles are in the size range of 50 to 100 nm. (c) Bright field TEM micrograph of an individual nZVI particle reveals a dense core encapsulated by a thin continuous layer of iron oxide. The inset shows electron diffraction from the interior core region, in which the diffuse ring pattern is characteristic of polycrystalline *bcc* Fe(0). (d) Phase contrast TEM image of a particle. The lack of long-range periodic lattice fringes in the oxide region suggests it is amorphous in nature.

presented in this work, an initial As(III) concentration of 100 mg/L was used for the HR-XPS analysis. This concentration also affords the measurement of arsenic removal capacity and kinetics by different iron materials. Figure 5.2 compares the rate of As(III) removal by nZVI and Fe<sub>3</sub>O<sub>4</sub> at a mass dose of 5 g/L. Rapid loss of aqueous As(III) from the solution phase was observed upon addition of nZVI. The total aqueous arsenic concentration decreased to 106 µg/L (corresponding to ~ 99.9% removal) at 10 min and it was below the detection limit after 1 h of mixing. Since the nZVI samples for XPS analysis were collected after at least 10 min of reaction, rapid loss of arsenic in the solution phase suggests that changes in arsenic speciation observed by XPS resulted from solid-phase reactions instead of sorption of homogenous reaction products. Under similar conditions, Fe<sub>3</sub>O<sub>4</sub> resulted in sequestration of only 13% of the aqueous As(III). A large difference in As(III) retention capacity between nZVI and the iron oxides can be clearly seen in the inset of Figure 5.2, which compares final As(III) removal after 24 h by various doses (0.4 – 5 g/L) of nZVI, Fe<sub>3</sub>O<sub>4</sub>, and Fe<sub>2</sub>O<sub>3</sub>. Despite a relatively high initial concentration (100 mg/L), nearly complete removal of As(III) was obtained with a nZVI dose as low as 1 g/L, whereas the removal efficiency remained below 20% even at the highest dose (5 g/L) of Fe<sub>3</sub>O<sub>4</sub> and Fe<sub>2</sub>O<sub>3</sub>. Since the BET specific surface areas of nZVI and the two oxides are comparable (Table 5.1), direct comparison of mass-normalized As(III) removal capacity can be made. For nZVI, the maximum As(III) loading capacity is 2.2 mM As/g, while the value of the oxides is no more than 0.17 mM As/g. Applying a surface complexation model in which the average adsorption site density of an iron oxide surface is ~3 sites/nm<sup>2</sup> [11], we can estimate a maximum As(III) adsorption of ~ 0.2 mM

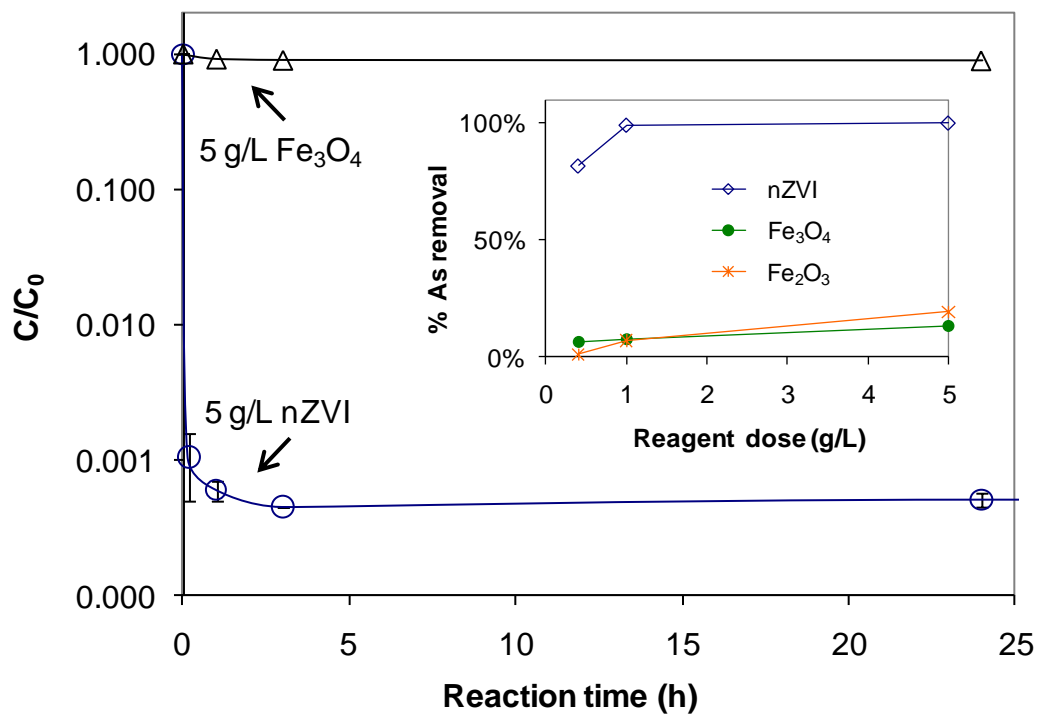


Figure 5.2. Change in aqueous arsenic concentration with time. Initial As(III) concentration ( $C_0$ ) was 100 mg/L; nZVI or iron oxide dose was 5 g/L. Inset: percentage As(III) removal at various dose of iron materials after 24 hours.

As/g, which is consistent with the observed capacities of the iron oxides. On the other hand, the arsenite loading capacity of nZVI is well in excess of the total surface adsorption sites available, which suggests arsenite is present in more than a mere surface layer. Previous studies have attributed similar results to As(III) forming co-precipitates with ferric ions [19,22] and the continuous production of iron corrosion products supplying additional surface sites for As(III) uptake [20-21]. Although arsenite oxidation [18, 20, 35] and reduction [21] have been observed in the presence of ZVI, the role of redox reactions has not been explicitly examined.

### 5.3.3 Arsenic speciation on the solid phase

Figure 5.3 shows As3d XPS spectra of different iron materials reacted with As(III) or As(V) solutions for 24 hours. The spectra were fitted by three arsenic chemical states, viz., As(V), As(III), and As(0), where each state gives rise to a doublet from spin-orbit splitting of the As3d<sub>3/2</sub> and As3d<sub>5/2</sub> components [28]. The binding energies (BE) of the different chemical states of the As3d<sub>5/2</sub> component are assigned as follows: As(V) 44.8 eV, As(III) 43.5 eV, and As(0) 40.5 eV. More details of the curve-fitting procedures are described elsewhere [28,30]. The effect of X-ray and electron-induced chemical changes was checked by comparing scans obtained immediately upon X-ray irradiation (exposure of 10 min) with those obtained after the sample was exposed to X-ray irradiation for over 1 h, which showed little change in peak shapes and positions. Two samples from replicate solution experiments were analyzed in separate XPS sessions, and the apparent compositions of major species measured in the two samples agree with each

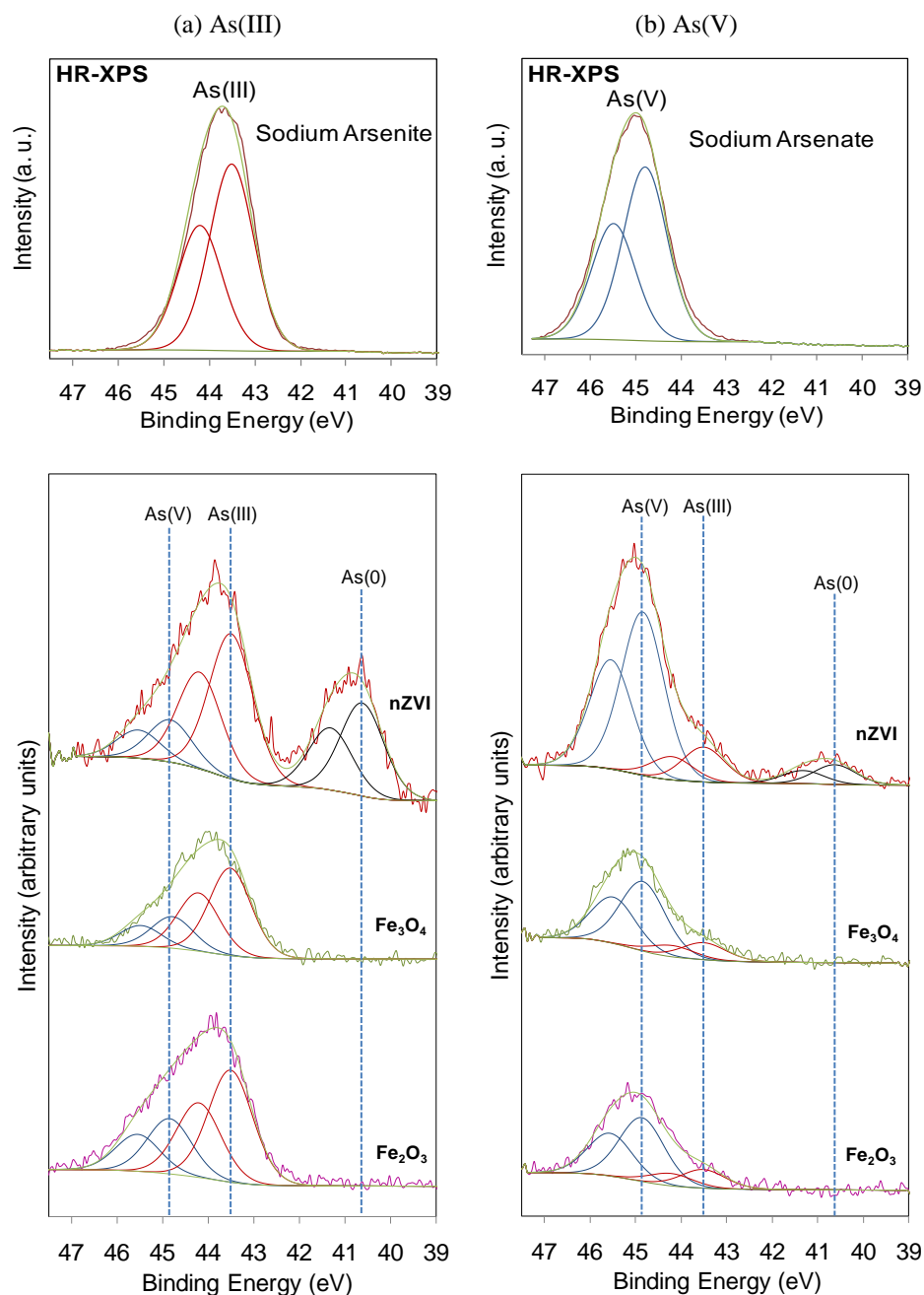
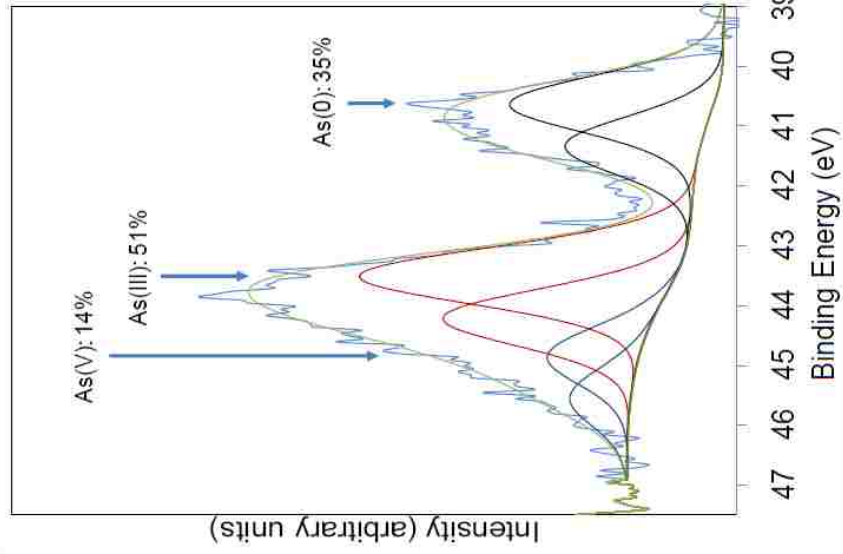


Figure 5.3 As3d HR-XPS spectra of (a) As(III) and (b) As(V) reacted with nZVI and iron oxide particles. The top spectra are those of pure sodium arsenite ( $\text{NaAsO}_2$ ) and sodium arsenate ( $\text{Na}_2\text{HAsO}_4 \cdot 7\text{H}_2\text{O}$ ), respectively, which were precursors used to prepare As(III) and As(V) solutions. Initial As(III) or As(V) concentration was 100 mg/L; mass loading of iron materials was 5 g/L; reaction time was 24 hours.

Table 5.2 Comparison of XPS spectra of two replicate experiments in Figure 5.4

<b>Sample</b>	<b>As(V) (rel. %)</b>	<b>As(III) (rel. %)</b>	<b>As(0) (rel. %)</b>	<b>As total (at.%)</b>	<b>Fe 2p (at.%)</b>	<b>O 1s (at.%)</b>	<b>C 1s (at.%)</b>
Replicate 1	14	51	35	1.36	16.81	67.23	14.59
Replicate 2	16	44	40	1.40	19.58	62.80	16.22
Difference	2	7	5	0.04	2.77	4.43	1.63

Replicate 1 As3d



Replicate 2 As3d

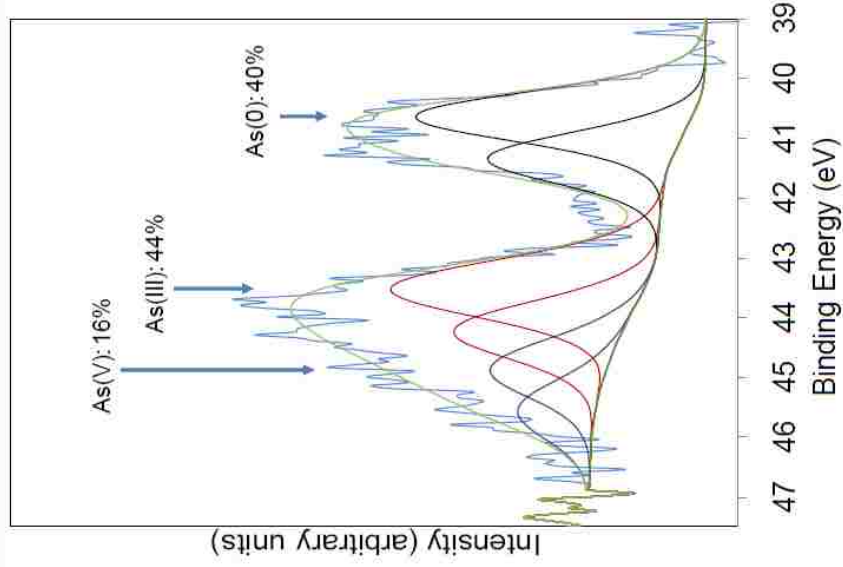


Figure 5.4 Comparison of As3d XPS spectra of two replicate experiments. Experimental conditions: As(III) initial concentration 100 mg/L, nZVI dose 5 g/L, reaction time 24 hour.



other with deviations < 8% (Table 5.2), which include the overall uncertainty in carrying out the solution experiments in addition to the XPS analysis (Figure 5.4).

As shown in Figure 5.3a, the solid residue of nZVI after reaction with As(III) solution for 24 h contains As(V), As(III) and As(0) species at an apparent relative abundance of 14%, 51%, and 35%, respectively [36]. The emergence of As(V) arsenic species and elemental arsenic offers clear evidence of divergent As(III) oxidation and reduction in the nZVI system. We have previously postulated that As(III) oxidation is mediated by the oxide layer at the nZVI surface [28], which is supported by our recent study showing As(V) preferentially concentrates at the top surface of the nanoparticles [30]. In addition, experiments with Fe<sub>3</sub>O<sub>4</sub> and Fe<sub>2</sub>O<sub>3</sub> under identical conditions had approximately 27% and 33% of the solid-phase arsenite oxidized to As(V), confirming the role of iron oxides in mediating arsenite oxidation. Previous studies have reported that iron oxides, including magnetite, goethite ( $\alpha$ -FeOOH), hematite ( $\alpha$ -Fe<sub>2</sub>O<sub>3</sub>) and ferrihydrite, are able to induce As(III) oxidation in the presence of surface Fe(II) species [37-38]. While several studies suggest dissolved oxygen is required in the process to produce reactive oxygen species with Fe(II) [35,38], As(III) oxidation under anoxic conditions has also been reported via possibly a Fe(III) oxide-Fe(II)-As(III) surface ternary complex [37]. In our study reported here, the solutions were purged with pure nitrogen for 30 minutes to remove dissolved oxygen and anoxic conditions were maintained during solution experiments and sample preparation, we thus consider arsenite oxidation reported in this study does not involve dissolved oxygen to a significant extent but is largely enabled by the oxide surfaces containing Fe(II) species that catalyzes surface redox exchange with the adsorbed contaminants [39].

While both nZVI and the two iron oxides can induce As(III) oxidation, the ability to form As(0) is an attribute of nZVI only. As(0) contributes ~ 33% of the total As signal for the sequestered arsenic (Figure 5.3a). As(0) formation has not been observed in conventional ZVI powders [18-20], except in a study performed on a polished and acid-treated Fe(0) surface that presumably had a fresh surface of metallic iron [21]. The ability of nZVI to maintain a reducing capability despite having an oxide film suggests the oxide layer of nZVI is amenable to electron transport or diffusion of arsenic into the region adjacent to the metallic iron. Prior studies reported that the composition within the several-nanometer thick oxide film is not homogeneous, but varying from a Fe(II)-rich layer in the vicinity of the Fe(0) interface to predominantly ferric oxide at the periphery [40-41]. The structural heterogeneity and the curvature of the oxide layer caused by the small radii of the nanoparticles are likely to produce a significant level of strains and defects (e.g. vacancies) in the oxide phase, which may lead to high ionic mobility even at room temperature [42]. Electron or charge transfer in oxide, especially mixed valent Fe(II) and Fe(III) oxide, are well studied [43], and the property may be further enhanced by the presence of impurities, such as boron [44] from the synthesis procedure. Indeed, using a XPS multiline approach that enables us to resolve arsenic speciation along the depth of the oxide layer, we observed that As(0) is located primarily underneath the surface in proximity to the Fe(0) core, which implies that arsenite reduction occurs at a sub-surface region and likely involves inward penetration of As(III) species [30].

The reductive capability of nZVI is also manifested in As(V) experiments. Figure 5.3b presents XPS spectra of samples reacted with As(V) solutions for 24 h. Approximately 16 and 9% of the immobilized arsenic signal was reduced to As(III) and

As(0), respectively. Different from the swift removal of As(III) species, sequestration of As(V) by nZVI took place more gradually over a time scale of hours (Figure 5.5). Thus, the solid phase As(III) may partly come from homogeneous reduction of As(V) followed by adsorption, recognizing that reduction of aqueous As(V) is thermodynamically permissible at the given pH and  $E_h$  conditions (Table 5.3) [2]. No As(0) was detected on the two iron oxides, although a small fraction of As(III) was formed in both samples, which has not been reported in previous X-ray absorption studies. Taken together, our results demonstrate arsenic removal by nZVI involves more than simple adsorption or coprecipitation. Multiple redox transformations shape to a large extent arsenic speciation and distribution in the solid phase. The redox duality exhibited by nZVI in As(III) solutions, resulting in As(V) and As(0) formation at different regions of the nanoparticles, relates to the structure of the nanoparticles containing a highly reducing metallic core and an adsorptive, and relatively permeable, oxide shell.

#### 5.3.4 Arsenic speciation over time

The progressive transformation of arsenic species in nZVI was investigated by analyzing the reaction products at various times between 10 min to 24 h (Figure 5.6). Solution phase analysis confirms that 99.9% of the aqueous As(III) was captured by nZVI within 10 min (Figure 5.2), and therefore the total amount of arsenic present in the solid phase was effectively constant during the monitoring period. As shown in Figure 5.6, the maximum formation of As(V) (~ 40% of the total arsenic intensity) was observed at 10 min, and then this gradually declined with time over 24 h. The opposite trend can be noted for As(0), which contributes 15% of the total As intensity at 10 min, and rises

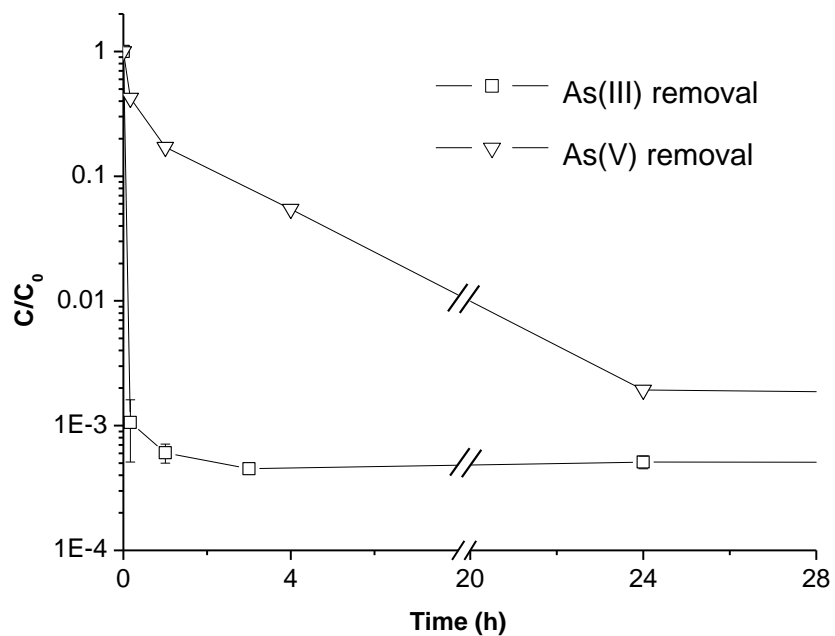


Figure 5.5 Comparison of As(III) and As(V) removal rate with nZVI. The initial concentration of As(III) or As(V) was 100 g/L; the mass loading of nZVI was 5 g/L.

Table 5.3 Solution pH and  $E_h$  values, speciation of solid-phase arsenic, and aqueous phase arsenic and iron concentrations.

Initial As species	Iron material	Reaction time	Final pH	Final $E_h$ (mV)	Solid phase				XPS spectrum	Solution	
					As(V) <sup>a</sup> (rel. %)	As(III) <sup>a</sup> (rel. %)	As(0) <sup>a</sup> (rel. %)	As Total <sup>b</sup> (at. %)		Fe (mg/L)	As <sup>c</sup> ( $C_{final}/C_0$ )
As(III)	5 g/L nZVI	24 h	8.9	-49	14	51	35	1.36	Fig. 2a/3/4	0.15	UD <sup>d</sup>
As(III)	5 g/L Fe <sub>3</sub> O <sub>4</sub>	24 h	9.9	279	38	62	0	2.57	Fig. 2a	0.57	0.87
As(III)	5 g/L Fe <sub>2</sub> O <sub>3</sub>	24 h	10.0	306	40	60	0	2.09	Fig. 2a	0.52	0.81
As(V)	5 g/L nZVI	24 h	9.2	-398	75	16	9	2.54	Fig. 2b	0.37	0.002
As(V)	5 g/L Fe <sub>3</sub> O <sub>4</sub>	24 h	8.5	274	80	20	0	0.82	Fig. 2b	-	-
As(V)	5 g/L Fe <sub>2</sub> O <sub>3</sub>	24 h	8.4	285	78	22	0	0.69	Fig. 2b	0.15	0.94
As(III)	5 g/L nZVI	10 min	-	-	40	45	15	2.24	Fig. 3	0.18	0.001
As(III)	5 g/L nZVI	1 h	9.1	-44	23	51	26	1.50	Fig. 3	0.23	UD <sup>d</sup>
As(III)	5 g/L nZVI	4 h	9.0	-48	21	51	28	1.20	Fig. 3	0.76	UD <sup>d</sup>
As(III)	5 g/L nZVI	15 d	8.7	-44	21	49	30	1.84	Fig. 3	0.73	UD <sup>d</sup>
As(III)	0.4 g/L nZVI	24 h	9.5	199	45	55	0	3.60	Fig. 4	1.84	0.82
As(III)	1 g/L nZVI	24 h	9.9	157	27	73	0	5.32	Fig. 4	0.17	0.04

<sup>a</sup> Determined by the relative intensities of individual arsenic valence state relative to that of total arsenic detected. <sup>b</sup> Determined by the intensity of As relative to those of other major species present, including C, Fe, and O, each normalized by the respective sensitivity factors. <sup>c</sup> Initial aqueous arsenic concentration 100 mg/L. <sup>d</sup> Final concentration below the detection limit (50µg/L)

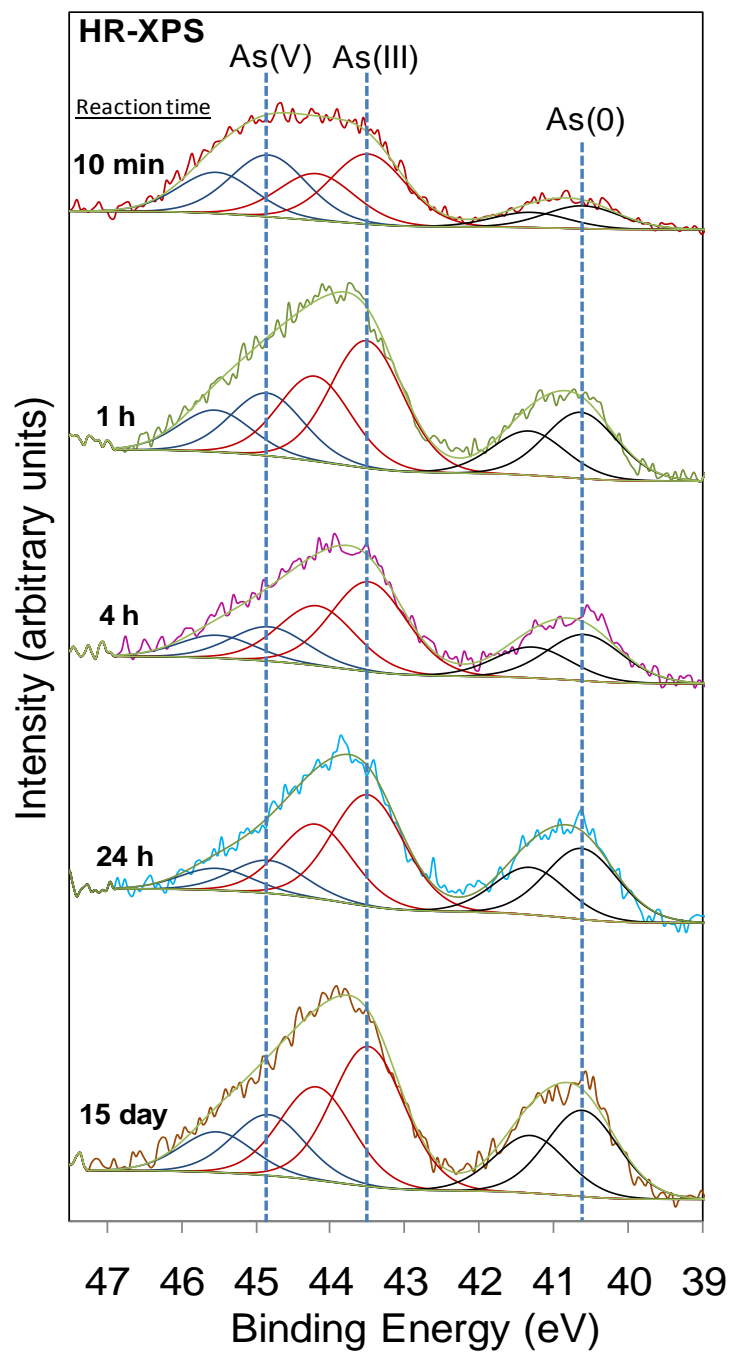


Figure 5.6. As<sub>3d</sub> HR-XPS spectra of nZVI reacted with As(III) for different times. Initial As(III) concentration was 100 mg/L; nZVI loading was 5 g/L.

Table 5.4 Surface elemental composition determined by XPS analysis <sup>a</sup>

<b>Sample description <sup>b</sup></b>	<b>As 3d (at.%)</b>	<b>C 1s (at.%)</b>	<b>Fe 2p (at.%)</b>	<b>O 1s (at.%)</b>
As(III), 5 g/L nZVI, 24 h	1.36	14.6	16.8	67.2
As(III), 5 g/L Fe <sub>3</sub> O <sub>4</sub> , 24 h	2.57	18.6	16.8	62.0
As(III), 5 g/L Fe <sub>2</sub> O <sub>3</sub> , 24 h	2.09	10.9	27.1	60.0
As(V), 5 g/L nZVI, 24 h	2.54	21.6	19.5	56.8
As(V), 5 g/L Fe <sub>3</sub> O <sub>4</sub> , 24 h	0.82	16.9	25.2	57.0
As(V), 5 g/L Fe <sub>2</sub> O <sub>3</sub> , 24 h	0.69	16.3	25.0	58.0
As(V), 5 g/L nZVI, 10 min	2.24	12.2	15.8	69.8
As(V), 5 g/L nZVI, 1 h	1.50	15.0	16.0	67.5
As(V), 5 g/L nZVI, 4 h	1.20	14.6	17.6	66.6
As(V), 5 g/L nZVI, 15 d	1.84	22.2	14.9	61.1
As(III), 0.4 g/L nZVI, 24 h	3.82	29.7	10.4	56.1
As(III), 1 g/L nZVI, 24 h	6.63	41.3	8.03	44.1

<sup>a</sup> Composition as atomic percent for each element *i* was calculated according to Eq. (1)

$$C_i = \frac{A_i / S_i}{\sum_i A_i / S_i} \quad (1)$$

where  $A_i$  is the measured peak area and  $S_i$  is the relative sensitivity factor. These latter values were taken from literature [45] as:  $S(\text{C}1s)=1.0$ ,  $S(\text{O}1s)=2.93$ ,  $S(\text{Fe}2p)=16.4$ , and  $S(\text{As}3d)=1.82$ . The values shown in the table are apparent concentrations because of the inherent assumption in the calculation that each element is distributed homogeneously throughout the probe depth.

<sup>b</sup> Initial arsenic concentration was 100 mg/L.

steadily to 35% after 24 h (Table 5.4). The data indicate arsenite oxidation is a rapid reaction that is completed on a time scale of minutes upon loading nZVI into the solution. Facile As(III) oxidation has been reported in the presence of Fe(II)-adsorbed goethite and other mineral surfaces [37], where these surfaces catalyze oxidation reactions of adsorbed As(III). This surface-mediated oxidation model is also consistent with our prior finding that As(V) exists at the outer surface of the nanoparticles exposed to the aqueous phase [30]. The gradual loss of As(V) after the first 10 min in Figure 5.6 indicates As(III) conversion to As(V) is reversible. A similar finding, i.e., rapid initial As(III) oxidation followed by a slower transformation in the opposite direction, has been noted in the As(III)-Fe(II)-goethite system [37], which highlights the dynamic nature of arsenic-iron redox interactions. On the other hand, the relatively slow emergence of As(0) is consistent with the observation of As(0) at the Fe(0) interface. Because this would entail arsenite to undergo a diffusion step, which would likely be rate limiting, slower formation of As(0) is thus expected. The sample reacted for 15 days shows that there were no significant changes compared to the 24 hrs data, suggesting that the reduced arsenic encapsulated by the oxide layer will persist for a substantial amount of time in anoxic conditions.

### 5.3.5 Effect of nZVI dose

Figure 5.7 shows As3d XPS spectra of samples reacted with As(III) solutions at different nZVI doses. The formation of As(0) was observed at the highest dose of nZVI (5 g/L), but not in lower dose samples. The accompanying Fe2p XPS spectra reveals a



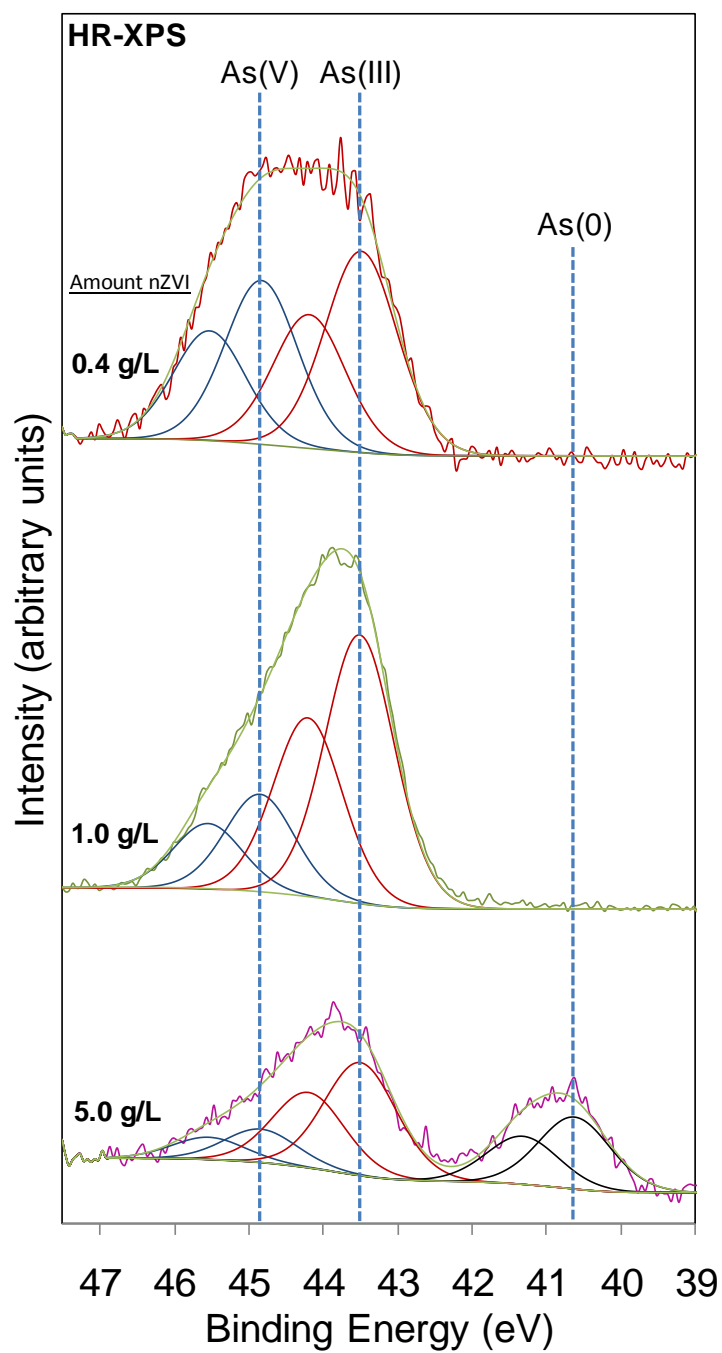


Figure 5.7 As3d HR-XPS spectra of varying dose of nZVI reacted with 100 mg/L As(III) for 24 hours.

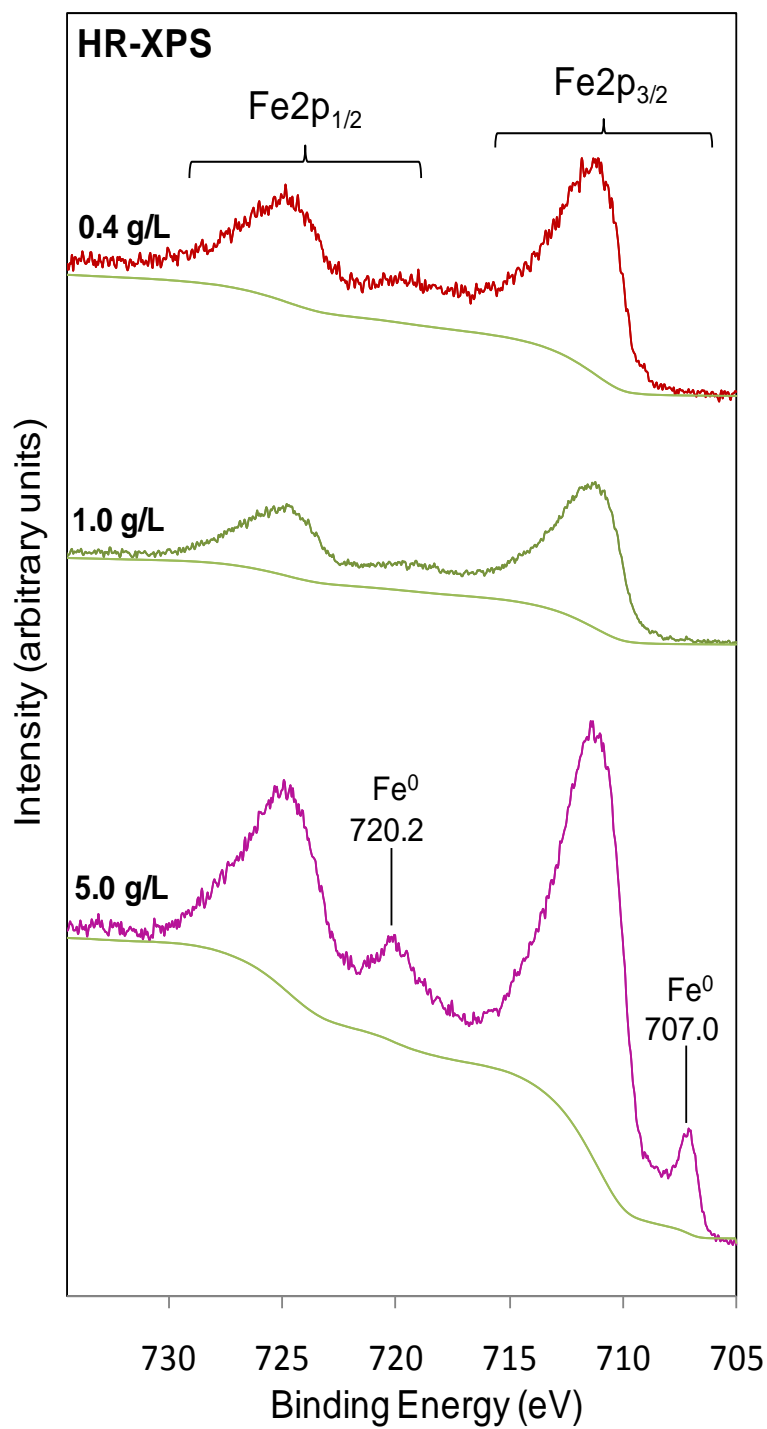


Figure 5.8 Fe2p XPS spectra of varying dose of nZVI reacted with As(III) solutions. Initial As(III) concentration was 100 mg/L; reaction time was 24 hours.

correlation of the presence of As(0) and Fe(0). Specifically, a Fe(0) 2p<sub>3/2</sub> component at 707.0 eV BE is present in the 5 g/L sample (Figure 5.8), whereas the solids contain only oxidized iron species in the 0.4 and 1 g/L samples. The concomitant appearance of As(0) and Fe(0) in XPS is consistent with As(0) residing at the Fe(0)-oxide interface as previously noted. Considering the XPS probe depth for Fe2p photoelectrons is ~ 6 nm, absence of a metallic iron signal in the low dose samples indicates the nanoparticles underwent pronounced corrosion, resulting in deposition of oxidation products on the surface. Extensive surface passivation may also be inferred from the solution phase E<sub>h</sub> values shown in Table 5.3, where the final E<sub>h</sub> values in 0.4 and 1 g/L nZVI systems are substantially higher than that of a freely corroding iron surface [46]. It was observed that the proportion of As(V) increased with decreasing nZVI dose. Based on the previous analysis of nZVI reacted for different amounts of time, the amount of As(V) present was controlled by the relatively fast As(V) formation and a slower reaction in the reverse direction. Severe corrosion or depletion of Fe(0) when only a small amount of nZVI was added may effectively quench the reverse reaction and result in more As(V) in the solid phase.

The distribution of arsenic species with different valence states within nZVI nanoparticles can be deduced by comparing intensities of each component within the As3d and As2p<sub>3/2</sub> XPS spectra, as discussed in our previous study [30]. As2p<sub>3/2</sub> spectra arise from photoelectrons emanating from a shallow surface region of ~ 1.4 nm, while As3d spectra are produced by photoelectrons from a greater depth of ~ 7 nm. The ratios of As2p<sub>3/2</sub> and As3d intensities therefore provide information about the depth where the species reside. Figure 5.9 plots the intensity ratios of individual arsenic valence states and

the total arsenic detected in each sample shown in Figure 5.7. As denoted in Figure 5.9, analyses of a pure homogenous arsenic material (sodium arsenite) gives a ratio close to one, thus larger and smaller values for the ratio indicate surface and deep-lying species, respectively. For the 5g/L nZVI sample, the ratios of different valence states are widely separated, implying the species predominate at different depths in the order of As(V)>As(III)>As(0) from surface toward the interior [30]. In 0.4 g/L or 1 g/L nZVI, only As(III) and As(V) were detected, and their intensity ratios are closer to one suggesting they are more diffusively distributed across the depth compared to the 5 g/L sample. In all cases, the ratios of the total arsenic are less than one, and this implies the bulk of the sequestered arsenic was embedded below the surface. Notably, increasing the iron dose causes the total arsenic ratio to be smaller, due to formation of As(0) as deep deposits and the increasing build-up of iron corrosion products.

### 5.3.6 Reaction model and practical implications

Evidence from solid and aqueous phase analyses can be used to establish that sequestered arsenite undergoes a series of redox transformations enabled by the oxide shell and metallic core of the nanoparticles, which results in arsenic being captured in multiple chemical states. Time-dependent and multiline analyses of the reacted solids using HR-XPS reveals the relative time scales of individual reactions and the distribution of arsenic valence states in the products, as shown schematically in Figure 5.10. The relative importance of each reaction shifts with time and the changing composition of nZVI during on-going corrosion. This stresses the importance of viewing the arsenic-nZVI system as dynamic instead of as a static, equilibrium-controlled system. Previous studies of reaction kinetics between iron materials and water contaminants rely largely on

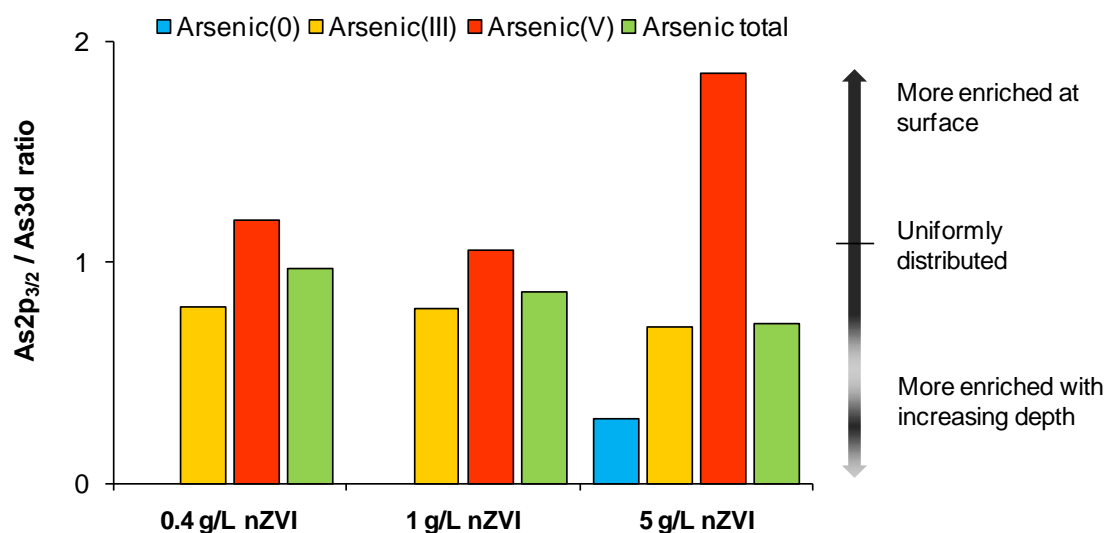


Figure 5.9 Intensity ratios of the As<sub>2p<sub>3/2</sub></sub> and As<sub>3d</sub> XPS spectra for the three samples in Figure 5.7. The raw intensities have been corrected by the relative sensitivity factors (S):  $S_{As_{2p}} = 31.5$  and  $S_{As_{3d}} = 1.82$ . The value of  $S_{As_{2p}}$  was determined empirically in a previous study [30] and  $S_{As_{3d}}$  was from ref [45]. Using sodium arsenite ( $NaAsO_2$ ) as a standard, we determined the intensity ratio of uniformly distributed arsenic species is 1.1 as indicated on the figure.

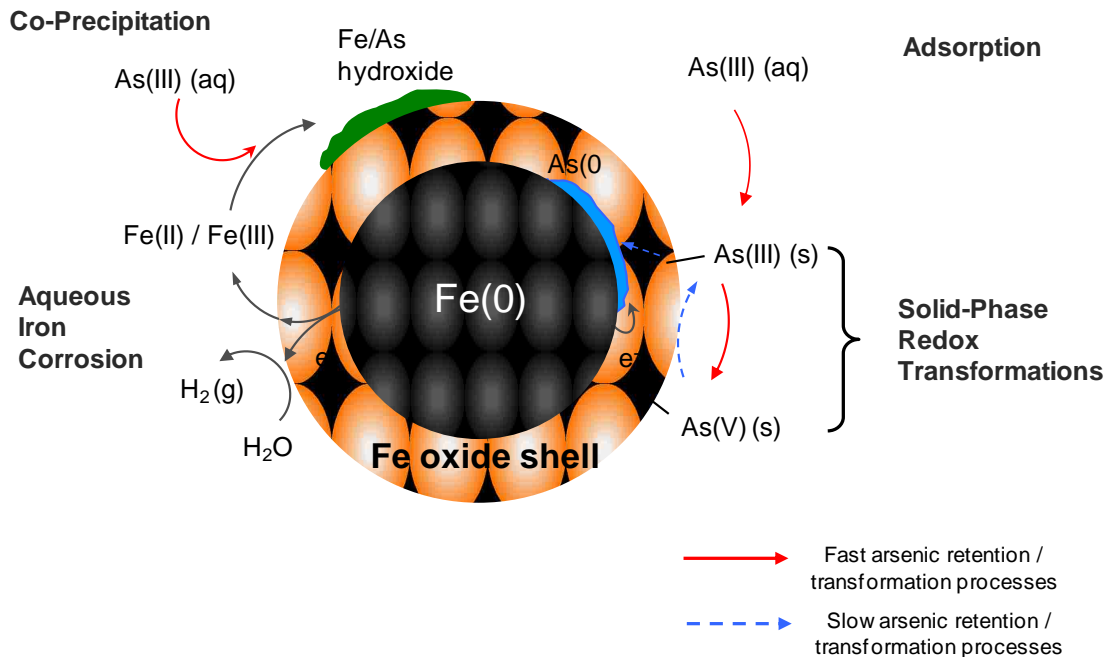


Figure 5.10 Schematic diagram summarizing processes responsible for arsenic removal in As(III)-nZVI system in anoxic conditions. The relative scale of the core and shell components of nZVI are for illustration only and do not reflect actual dimensions. As(III) may be taken up from the aqueous phase by adsorption or co-precipitation. The solid-bound As(III) is oxidized rapidly at the oxide surface, and the As(V) formed may be reverted to As(III) at a slower rate. Some As(III) diffuses towards Fe(0) core and is reduced to elemental arsenic (As(0)) near the oxide/Fe(0) interface.

measurements of contaminant concentrations in bulk solutions. The temporal and spatial variations of arsenic speciation in nZVI observed in this study suggest more attention may be given to the kinetics of solid-phase redox reactions so as to obtain a more complete understanding of the reaction mechanisms.

The redox interactions reported here have significant implications on nZVI remediation performance as well as arsenic speciation and distribution in the final products. A distinct feature of nZVI relative to conventional adsorbents is that a large proportion of arsenic is embedded within the oxide structure instead of being retained as surface adsorbed species. Continuous iron corrosion in this case, not only serves to encapsulate the sequestered arsenic, but also supplies a continuous source of reactive sites for arsenic abatement. As such, nZVI exhibits much larger arsenic removal capacities than iron oxides on a mass or surface area basis, and the retained arsenic is potentially less susceptible to leaching caused by pH changes [11,13] and competing anions (e.g., phosphate) [12,47]. Compared to bulk ZVI materials, nZVI is capable of both arsenite oxidation and reduction, which results in heterogeneous spatial distributions of arsenic valence states in the solids representing a new form of arsenic sequestration product previously not discussed.

#### **5.4 Conclusion**

From an application point of view, the removal kinetics and arsenic loading per unit mass of nZVI are expected to be significantly higher than those of bulk ZVI materials owing to its larger reactive surface and a greater "volume" participated in the solid-phase redox exchanges. These virtues render nZVI a good candidate for *in situ*

applications in underground source zones and for use in centralized water treatment facilities. Since nZVI is a reactive and consumable material, the evolution of these nanoparticles and the stability of sequestered arsenic over long time periods (on the order of months or longer) in environmentally relevant conditions need to be systematically evaluated for these applications.



## REFERENCES FOR CHAPTER V

1. Nordstrom, D. K., *Science* **2002**, 296, 2143.
2. Smedley, P. L.; Kinniburgh, D. G., *Appl. Geochem.* **2002**, 17, 517.
3. Meharg, A. A.; Rahman, M., *Environ. Sci. Technol.* **2003**, 37, 229.
4. Dittmar, J.; Voegelin, A.; Roberts, L. C.; Hug, S. J.; Saha, G. C.; Ali, M. A.; Badruzzaman, A. B. M.; Kretzschmar, R., *Environ. Sci. Technol.* **2010**, 44, 2925.
5. Mandal, B. K.; Suzuki, K. T., *Talanta* **2002**, 58, 201.
6. WHO guidelines for drinking-water quality, 3rd edition, 2008.  
[http://www.who.int/water\\_sanitation\\_health/dwq/gdwq3rev/en/index.html](http://www.who.int/water_sanitation_health/dwq/gdwq3rev/en/index.html)
7. Edwards, M., *J. Am. Water Works Assn.* **1994**, 86, 64.
8. Sarkar, S.; Gupta, A.; Biswas, R. K.; Deb, A. K.; Greenleaf, J. E.; SenGupta, A. K., *Water Res.* **2005**, 39, 2196.
9. Mohan, D.; Pittman, C. U., *J. Hazard. Mater.* **2007**, 142, 1.
10. Hussam, A.; Munir, A. K. M., *J. Environ. Sci. Health. Part A Toxic/Hazard. Subst. Environ. Eng.* **2007**, 42, 1869.
11. Dixit, S.; Hering, J. G., *Environ. Sci. Technol.* **2003**, 37, 4182.
12. Korte, N. E.; Fernando, Q., *Crit. Rev. Env. Control* **1991**, 21, 1.
13. Raven, K. P.; Jain, A.; Loeppert, R. H., *Environ. Sci. Technol.* **1998**, 32, 344.
14. Manning, B. A.; Fendorf, S. E.; Goldberg, S., *Environ. Sci. Technol.* **1998**, 32, 2383.
15. Manceau, A., *Geochim. Cosmochim. Acta* **1995**, 59, 3647.

16. Goldberg, S.; Johnston, C. T., *J. Colloid Interface Sci.* **2001**, *234*, 204.
17. Ona-Nguema, G.; Morin, G.; Juillot, F.; Calas, G.; Brown, G. E., *Environ. Sci. Technol.* **2005**, *39*, 9147.
18. Su, C. M.; Puls, R. W., *Environ. Sci. Technol.* **2001**, *35*, 1487.
19. Lackovic, J. A.; Nikolaidis, N. P.; Dobbs, G. M., *Environ. Eng. Sci.* **2000**, *17*, 29.
20. Manning, B. A.; Hunt, M. L.; Amrhein, C.; Yarmoff, J. A., *Environ. Sci. Technol.* **2002**, *36*, 5455.
21. Bang, S.; Johnson, M. D.; Korfiatis, G. P.; Meng, X. G., *Water Res.* **2005**, *39*, 763.
22. Lien, H. L.; Wilkin, R. T., *Chemosphere* **2005**, *59*, 377.
23. Ponder, S. M.; Darab, J. G.; Mallouk, T. E., *Environ. Sci. Technol.* **2000**, *34*, 2564.
24. Liu, Y. Q.; Choi, H.; Dionysiou, D.; Lowry, G. V., *Chem. Mater.* **2005**, *17*, 5315.
25. Li, X. Q.; Zhang, W. X., *J. Phys. Chem. C* **2007**, *111*, 6939.
26. Kanel, S. R.; Manning, B.; Charlet, L.; Choi, H., *Environ. Sci. Technol.* **2005**, *39*, 1291.
27. Kanel, S. R.; Greneche, J. M.; Choi, H., *Environ. Sci. Technol.* **2006**, *40*, 2045.
28. Ramos, M. A. V.; Yan, W.; Li, X. Q.; Koel, B. E.; Zhang, W. X., *J. Phys. Chem. C* **2009**, *113*, 14591.
29. Martin, J. E.; Herzing, A. A.; Yan, W. L.; Li, X. Q.; Koel, B. E.; Kiely, C. J.; Zhang, W. X., *Langmuir* **2008**, *24*, 4329.
30. Yan, W. L.; Ramos, M. A. V.; Koel, B. E.; Zhang, W. X., *Chem. Comm.*, **2010**, *46*, 6995.
31. Li, X. Q.; Zhang, W. X., Iron nanoparticles: *Langmuir*, **2006**, *22*, 4638.
32. Sun, Y. P.; Li, X. Q.; Cao, J. S.; Zhang, W. X.; Wang, H. P., *Adv. Colloid Interface Sci.* **2006**, *120*, 47.
33. Contour, J. P.; Massies, J.; Fronius, H.; Ploug, K. *Jpn. J. Appl. Phys.* **1988**, *27*, L167.

34. Cao, J. S.; Li, X. Q.; Tavacoli, J.; Zhang, W. X., *Environ. Sci. Technol.* **2008**, *42*, 3780.
35. Katsoyiannis, I. A.; Ruettimann, T.; Hug, S. J., *Environ. Sci. Technol.* **2008**, *42*, 7424.
36. The values shown in the figure are apparent concentrations because of the inherent assumption in the calculation that each element is distributed homogeneously throughout the probe depth.
37. Amstaetter, K.; Borch, T.; Larese-Casanova, P.; Kappler, A., *Environ. Sci. Technol.* **2010**, *44*, 102.
38. Ona-Nguema, G.; Morin, G.; Wang, Y. H.; Foster, A. L.; Juillot, F.; Galas, G.; Brown, G. E., *Environ. Sci. Technol.* **2010**, *44*, 5416.
39. Borch, T.; Kretzschmar, R.; Kappler, A.; Van Cappellen, P.; Ginder-Vogel, M.; Voegelín, A.; Campbell, K., *Environ. Sci. Technol.* **2010**, *44*, 15.
40. Wang, C. M.; Baer, D. R.; Amonette, J. E.; Engelhard, M. H.; Antony, J.; Qiang, Y., *J. Am. Chem. Soc.* **2009**, *131*, 8824.
41. Signorini, L.; Pasquini, L.; Savini, L.; Carboni, R.; Boscherini, F.; Bonetti, E.; Giglia, A.; Pedio, M.; Mahne, N.; Nannarone, S., *Phys. Rev. B* **2003**, *68*, 195423.
42. Garcia-Barriocanal, J.; Rivera-Calzada, A.; Varela, M.; Sefrioui, Z.; Iborra, E.; Leon, C.; Pennycook, S. J.; Santamaria, J., *Science* **2008**, *321*, 676.
43. Kerisit, S.; Rosso, K. M., *J. of Chem. Phys.* **2005**, *123*, 224712.
44. Carpenter, E. E.; Calvin, S.; Stroud, R. M.; Harris, V. G., *Chem. Mater.* **2003**, *15*, 3245.
45. Fairley, N.; Carrick, A. *The Casa Cookbook – Part 1: Recipes for XPS data Processing*; Acolyte Science: Cheshire, U.K., 2005.
46. Melitas, N.; Conklin, M.; Farrell, J., *Environ. Sci. Technol.* **2002**, *36*, 3188.
47. Hug, S. J.; Leupin, O. X.; Berg, M., *Environ. Sci. Technol.* **2008**, *42*, 6318.

## CHAPTER VI

### CONCLUDING REMARKS

#### 6.1 Summary

Detailed characterization of the oxide/hydroxide shell thickness nZVI nanoparticles has been discussed. High-resolution TEM images provided direct evidence of the core-shell structure and indicated that nZVI nanoparticles had a shell thickness of 2 - 4 nm. Also by using HR-XPS analysis and the relative integrated intensities of metallic and oxidized iron with a geometric correction an average shell thickness of 2.3 - 2.8 nm was obtained.

In addition, by analyzing the solid and aqueous phases during arsenite sequestration processes, we have confirmed that the removal of As(III) from the aqueous phase by nZVI proceeds rapidly and the multiple states of arsenic observed on the reacted nZVI are a result of several parallel or sequential solid phase reactions. Unlike the models conceived in prior studies, which mainly ascribe As-nZVI reactions to surface adsorption or co-precipitation processes, the results here demonstrate explicitly the active redox transformations effected by the oxide shell and the metallic core of the particles.

Furthermore, while earlier studies have demonstrated effective As(III) sequestration by iron oxide minerals or bulk-scale Fe(0) materials, nZVI has been shown

to react much more rapidly with As(III) and has a substantially greater sequestration capacity than these conventional iron materials.

The distinct layers where As(V) and As(0) reside imply As(III) oxidation and reduction occur at different physical fronts. The ability to impregnate arsenic into the solid phase renders nZVI a potentially more voluminous sink for arsenic compared to the widely used iron oxides, whose capacities are limited by the available surface coordinative sites and are subject to competition from co-existing anions in the water.

## MAURICIO ALFRED VALENCIA RAMOS

Lehigh University  
Department of Chemistry  
6 E. Packer Ave.  
Bethlehem, PA 18015  
[mar205@lehigh.edu](mailto:mar205@lehigh.edu)

### EDUCATION

---

**Ph.D.** Chemistry, *Lehigh University, Bethlehem, PA 18015* **May 2011**

- Thesis Title: "Sequestration of Arsenic by Nanoscale Zero-Valent Iron (nZVI): Surface Reactions Characterized by High Resolution X-ray Photoelectron Spectroscopy (HR-XPS)"
- Advisor: Prof. Bruce E. Koel

**Graduate coursework**, *University of Southern California, Los Angeles, CA 90089*

**Jan. 2004 – Aug. 2005**

- Completed required 24 semester hours of graduate coursework toward Ph.D. degree in Phys. Chemistry

**B.S.** Chemistry, *California State University, Los Angeles, CA 90032*

**Dec. 2003**

- Research: "Measurements of urban pollutant gradients (ozone) on a fine scale"
- Advisor: Dr. Scott Nickolaisen

**A.S.** Chemistry, *Los Angeles City College, Los Angeles, CA 90029*

**Dec. 2000**

### RESEARCH/WORK EXPERIENCE

---

**Graduate Research Assistant** • *Lehigh University, Bethlehem, PA*

**2005 – Present**

- Investigated the properties of *zero-valent iron nanoparticles* (nZVI) as a means to efficiently remove arsenic (>99%) from water.
  - Operated a high-resolution XPS instrument (Scienta ESCA 300) equipped with a monochromated AlK $\alpha$  X-ray source for the characterization and depth-profiling analysis of arsenic-treated nZVI, which resulted in observing for the first time the formation of metallic arsenic encapsulated by nZVI.
- Collaborated with colleagues in the Department of Civil and Environmental Engineering to analyze the reactions mechanisms for As sorption on nZVI under different chemical environments. Identified the physical location of the species arising from the three arsenic oxidation states (V, III, and 0) within the core and iron-oxide shell of nZVI nanoparticles.
  - Analyzed XPS data from the As-treated nZVI samples using CASA XPS MFC application software.
- Designed, developed, and tested an e-beam heater used to anneal metal surfaces up to 1100 °C in vacuum for use in catalysis studies.
- Mentored and provided scientific guidance to undergraduate students working in the Koel laboratory.
  - Developed and optimized a prototype high resolution IR instrument for applications of the IRAS technique to characterize and analyze reaction mechanisms of thiol self-assembled monolayers (SAMs) on Au(111) films as a means to study the properties of organic aerosol particles.

**Graduate Teaching Assistant • Lehigh University, Bethlehem, PA**

**2005 – 2006**

- Instructed and oversaw undergraduate students' safety and performance in both Organic Chemistry and Physical Chemistry laboratories.
- Graded laboratory reports and assignments.

**Graduate Teaching Assistant • University of Southern California, Los Angeles, CA**

**2004 – 2005**

- Set up experimental equipment and explained experimental procedures to undergraduate students in general chemistry laboratories.
- Graded laboratory reports, and exams.

**Undergraduate Research Assistant • California State University, Los Angeles, Los Angeles, CA**

**2001 – 2003**

- Developed an experiment for measuring and analyzing urban pollutant gradients on a fine scale with emphasis on ozone concentration detection in the Los Angeles metropolitan area.

**SKILLS**

---

- Able to understand, follow and translate scientific/technical/medical information in verbal or written form (English/Spanish)
- Proficient use of surface analytical techniques and instrumentation: High-Resolution X-ray Photoelectron Spectroscopy (**HR-XPS**) using the **Scienta ESCA 300**, Attenuated Total Reflectance Infrared Spectroscopy (**ATR-IR**), Low Energy Electron Diffraction (**LEED**), Auger Electron Spectroscopy (**AES**), and TECTRA *Gen II Oxygen Plasma Source*.
- Trained in **NMR and GC** analytical techniques.
- Proficient with Microsoft Office Applications, SigmaPlot Graphing Software, and *CASA XPS MFC Application Software*

**PUBLICATIONS**

---

- Mauricio A. V. Ramos, Weile Yan, Bruce E. Koel, and Wei-xian Zhang, "Arsenic sensitivity experiments for environmental studies using high-resolution X-ray photoelectron spectroscopy (HR-XPS)," *In Progress*.
- Weile Yan, Mauricio A. V. Ramos, Bruce E. Koel, and Wei-xian Zhang, "Removal of As(III) by iron nanoparticles (nZVI): mechanisms of solid-phase arsenic-iron reactions" Submitted to *Environ. Sci. Technol.* (10/10)
- Weile Yan, Mauricio A. V. Ramos, Bruce E. Koel, and Wei-xian Zhang, "Multi-tiered distributions of arsenic in iron nanoparticles: Observation of dual redox functionality enabled by a core-shell structure," *Chem. Commun.*, 2010, **46**, 6995-6997.
- Mauricio A. V. Ramos, Weile Yan, Xiao-qin Li, Bruce E. Koel and Wei-xian Zhang, "Simultaneous Oxidation and Reduction of Arsenic by Zero-Valent Iron Nanoparticles: Understanding the Significance of the Core-Shell Structure," *J. Phys. Chem. C*, **2009**, *113* (33), 14591–14594.

## **RECENT PRESENTATIONS/MEETINGS ATTENDED**

---

- **Mar. 23, 2011** — “Arsenic Encapsulation in Iron Nanoparticles: Evidence of Intraparticle Reactions” *A Unique Surface Analysis Symposium*: Poster Session; Lehigh University, Bethlehem, PA
- **Aug. 22-26, 2010** — “Multi-tiered distributions of arsenic in iron nanoparticles: Observation of dual redox functionality enabled by a core–shell structure” *ACS National Meeting and Expo*: Poster Session; Boston, MA
- **Apr. 13, 2010** — “Sequestration of Arsenic by nanoscale zero-valent iron (nZVI): Surface Reactions Characterized by High Resolution X-ray photoelectron spectroscopy (HR-XPS)” *Lehigh University Graduate Student Seminar*: Oral Presentation; Lehigh University, Bethlehem, PA
- **Jun. 17-19, 2009** — “Determination of Oxide Layer Thickness in Core-Shell Zero-Valent Iron Nanoparticles” *69<sup>th</sup> Annual Physical Electronic Conference*: Poster Session; Rutgers, The State University of New Jersey, Piscataway, NJ
- **Feb. 8-13, 2009** — “Determination of Oxide Layer Thickness in Core-Shell Zero-Valent Iron Nanoparticles” *Gordon Research Conference-Chemical Reactions at Surfaces*: Poster Session; Ventura, CA
- **Nov. 17, 2008** — “Probing the Chemistry of the Engel-Brewer Intermetallic Compound  $\text{HfIr}_3$  with  $\text{H}_2$ ,  $\text{CO}$ , Toluene, and Methylcyclohexane” *47<sup>th</sup> Eastern Analytical Symposium & Expo*: Poster Session; Somerset, NJ
- **Oct. 31 - Nov. 1, 2007** — *Balancing Energy and the Environment: An Exploration of Future Research Needs*: Attended; Lehigh University, Bethlehem, PA